PROBING QUANTUM PHASE SLIPS IN SUPERCONDUCTING NANOWIRES MODIFIED USING HIGH BIAS VOLTAGE PULSES

BY

THOMAS AREF

DISSERTATION

Submitted in partial fulfillment of the requirements
for the degree of Doctor of Philosophy in Physics
in the Graduate College of the
University of Illinois at Urbana-Champaign, 2010

Urbana, Illinois

Doctoral Committee:

Professor James Eckstein, Chair
Professor Alexey Bezryadin, Director of Research
Professor Yoshitsugo Oono
Professor Taek-Jip Ha

Abstract

Quantum phase slips (QPS) or the macroscopic quantum tunneling (MQT) of a nanowire's order parameter through an activation energy barrier have remained the subject of intense debate for many years. They are expected to occur at low enough temperature where thermally activated phase slips (TAPS) have been frozen out in analogy with Josephson junctions where the macroscopic tunneling of phase at low temperatures has been conclusively experimentally demonstrated. We address this question by following a similar experimental strategy to that employed for establishing MQT in JJs. By measuring switching current distributions, we can probe the phase slip rate and determine if it corresponds to thermal activation or quantum tunneling. Having established that the behavior we see is consistent with being in the quantum regime, we can alter properties of the nanowires and see if the response is consistent with the expectations of the quantum model. To do this we employ an in-situ modification technique using high bias voltage pulses. Using these pulses, we can change resistance, critical temperature, critical current and morphology of the nanowire. We can also change the shunting capacitance of the nanowire by altering the photolithography step used to create the nanowires electrodes. The resulting response of the nanowires agrees well with being in the quantum tunneling dominated regime. An interesting side benefit of the pulsing technique is that we can exactly set the nanowires switching current to a desired value. This may be instrumental in the development of superconducting nanowire qubits.

To my family.

Acknowledgments

First, I would like to thank my advisor, Alexey Bezryadin, who has had a large impact on my experience as a graduate student. I would not have the breadth of abilities I now possess if it were not for him and I will always admire his ability to come up with new, interesting ideas, many of which we unfortunately did not have time to fully pursue. I would like to acknowledge the help of the many members of the Bezryadin group I have known in my time here. In particular, I want to thank Tony Bollinger, Ulas Coskun, Andrey Rogachev and Dave Hopkins for showing me the ropes when I was starting and Matt Brenner, Jaseung Ku, Rob Dinsmore and Mitrabhanu Sahu for helping me transition into superconducting nanowires later in my graduate studies. I would also like to express my gratitude to my various friends and collaborators including Cesar Chialvo, Myung-ho Bae, Mikas Remeika, Bob Colby, C. J. Lo, Anil Nandyala, Hisashi Kajiura, Nick Salovich, Eric Olson and Michelle Nahas. I would like to say to everyone I have worked with that I have learned something from each and everyone of you and have always enjoyed working with you. I would also like to acknowledge the patient staff of MRL's microfab and CMM for the many hours of training and advice I received. In particular, I would like to thank Jian-Guo Wen, Changhui Lei, Mike Marshall, Bharat Sankaran, Tony Banks, Kevin Colravy and Vania Petrova. I would also like to thank Russ Giannetta for the use of his milling machine and Ivan Petrov for the loan of his MEMS TEM holder. Finally, I would like to acknowledge my parents, Hassan and Susanne, my brother, Michael, and my sister-in-law, Lan, for their continual support and advice through this long process. This work was supported by the U.S. Department of Energy under Grant No. DE-FG0207ER46453. This work was carried out in part in

the Frederick Seitz Materials Research Laboratory Central Facilities, University of Illinois, which are partially supported by the U.S. Department of Energy under Grant Nos. DE-FG0207ER46453 and DE-FG0207ER46471.

Table of Contents

Chapter 1

Introduction

1.1 Motivation

In 1911, Heike Kamerlingh Onnes observed the abrupt disappearance of resistance while performing transport measurements on solid mercury at cryogenic temperatures [1]. This phenomenon of electrical transport with zero resistance turned out to happen in a variety of metals and came to be known as superconductivity. Since that time superconductivity has been studied extensively but it is only with the advent of modern micro- and nano-fabrication techniques that certain questions can be addressed experimentally. One of these questions is superconductivity in a one dimensional system. It has been theoretically predicted that a one dimensional nanowire is never truly superconducting but that the occurrence of phase slips induces a non-zero resistance at all temperatures above absolute zero [2]. This resistance may however be vanishingly small. The fits to thermally activated phase slips (TAPS) models have been experimentally verified in numerous samples with fits ranging over many orders of magnitude [3–6]. A more interesting phenomena would be quantum tunneling of phase slips (QPS). This would be a continuation of the program proposed by Leggett [7] to search for examples of macroscopic objects behaving quantum mechanically. Efforts to observe QPS in nanowires have been underway for many years but doubts about the conclusivity of the experiments remain. The most popular method to look for QPS has been to analyze resistance versus temperature curves. Deviations from the expected Arrhenius law of TAPS have been taken as evidence for QPS. As shown in figure 1.1, these deviations take the form of resistance tails. Unfortunately, there can be many sources of this type of deviation

including inhomogeneities in the nanowire and noise in the measurement system. It was demonstrated by Bollinger et al. [8] that inhomogeneity can have a large effect on nanowire behavior and lead to surprising deviations. To further complicate the matter, homogeneous short nanowires generally indicate no signs of QPS tails [6, 9–12] while QPS tails have been primarily seen in longer nanowires [13–18]. The cause of this difference between short and long nanowires is not well understood. The experimental evidence for QPS in long nanowires using this method, though certainly indicative, cannot be considered conclusive.

No such doubts about macroscopic quantum tunneling (MQT) of the phase exists for Josephson junctions (JJs). JJ's have a current phase relationship (CPR) similar to the CPR for extremely short nanowires so they can be considered somewhat analogous to them. It should be noted that in a traditional oxide JJ, there is an actual physical barrier to tunnel through unlike a very short nanowire where the energy barrier is associated with driving a section of the wire normal during the phase slip process. This normal core associated with the phase slip could possibly suppress MQT in the nanowire. The most conclusive demonstration of MQT in JJs was first performed by Martinis, Devoret and Clarke [22]. By analyzing switching current distributions, they demonstrated both excellent agreement between the theoretical model for MQT in JJs and the splitting of the distribution expected for quantized energy levels. Only recently has this distribution technique been applied to studying QPS in nanowires by Sahu et al. [23] (see figure 1.2). At high temperatures, the switching distributions were well fit by a theory involving multiple TAPS. At low temperatures, they observed a deviation from the TAPS model. This deviation could be accounted for by including QPS effects. However, many questions remain. For technical reasons, it is difficult to repeat the splitting of the distribution experiment in the style of Martinis, Devoret and Clarke on nanowires as the plasma frequency of nanowires is approximately 100 GHz, a frequency where microwave engineering becomes difficult. Another question is that the QPS model used for nanowires shares many of the same features as the model for JJs yet there are two entirely different forms of behavior. For JJs, in the thermal region standard deviation

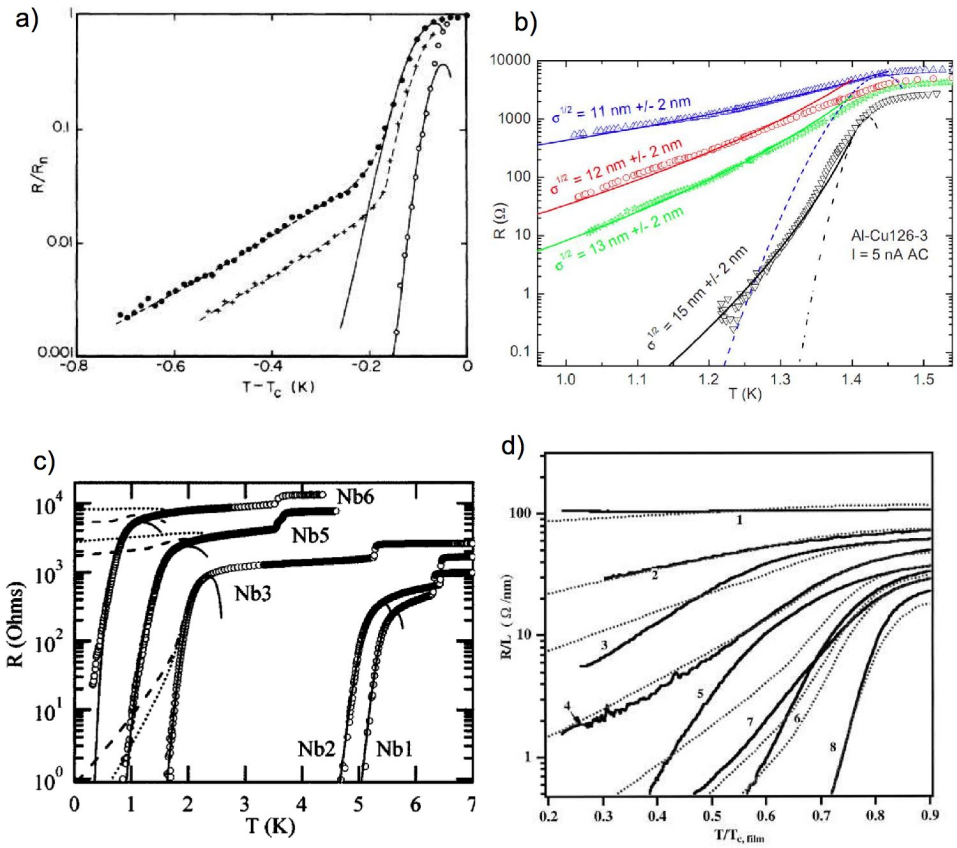

Figure 1.1: Resistance vs Temperature Measurements of Quantum Phase Slips a) From Giordano [14]. The resistive tails observed could not be fit with a TAPS model (solid lines). The dashed lines correspond to a heuristic model of QPS. These wires were observed to be inhomogeneous. b) From Zgirski et al [17]. Using a sputtering method, a single wire can be gradually reduced to a thinner and thinner wire. For the thinnest wire, a TAPS model (dashed lines) fails to fit the data yet a QPS model (solid lines) based on the theory of Golubev and Zaikin does [19]. SEM and AFM measurements indicate these wires were homogeneous but as noted in the paper, hidden structural defects could lead to a similar resistive tail. c) From Rogachev et al. [9]. Measurements on short niobium wires are well fit by a TAPS model (solid lines) with no sign of resistive tails associated with QPS (predictions shown by the dotted lines). The wire were fabricated using the molecular templating method developed by Bezryadin [20]. The same TAPS dominated behavior is observed on a wide range of short MoGe nanowires [12]. d) From Lau et al [13]. Longer nanowires fabricated with the same molecular templating technique showed behavior that could not be fit by TAPS but somewhat by QPS. This is an interesting result as it uses the same fabrication technique as c) which reliably produces shorter nanowires without resistive tails. It should be noted that preliminary evidence indicates that longer nanowires made by molecular templating are typically not as homogeneous as shorter ones [11, 21].

(the width of the switching distribution) increases with increasing temperature and there is a clear saturation effect when switching over to the quantum dominated region (see figure 1.2b). For nanowires, standard deviation is seen to decrease with increasing temperature and there is no clear transition from the thermal to quantum dominated region (see figure 1.2d). The question of TAPS versus QPS will occur repeatedly throughout this thesis and I will discuss experiments dealing both with resistance vs temperature measurements and switching current distribution measurements.

Macroscopic objects behaving quantum mechanically are also important for developing solid state quantum bits. Quantum bits are bits that can be prepared in a superposition of states unlike a conventional bit which is always either 0 or 1. There is great interest in the development of quantum bits, and hopefully quantum computers, since certain algorithms can run more quickly on a quantum computer than a regular computer. If QPS can be verified in superconducting nanowires, it has been suggested by Mooij and Harmans [25, 26] that superconducting nanowire qubits could be constructed. Nanowires are also attractive to researchers working with more traditional JJ qubits since nanowires do not have an oxide layer like JJs (it is believed impurities in the oxide layer has an effect on decoherence in qubits). In certain implementations of nanowire qubits, it is advantageous to have precise control over the critical (or switching current) of the nanowire. However, this is very difficult to achieve by fabrication alone as even wires with very similar parameters can have significant variation in their switching current. By using high voltage pulses, I have demonstrated that the switching current of a nanowire can be set precisely thus removing this obstacle in the development of nanowire qubits. Figure 1.3a shows how, in some applications, an oxide layer JJ can be replaced by a nanowire whose switching current can be tuned. Figure 1.3b shows a proposed implementation of a nanowire qubit [27]. In this scheme, the nanowire selects certain energy levels of the resonator (which would otherwise be equally spaced) as the levels of the qubit. Exact control of the switching current is necessary for this scheme to be effective.

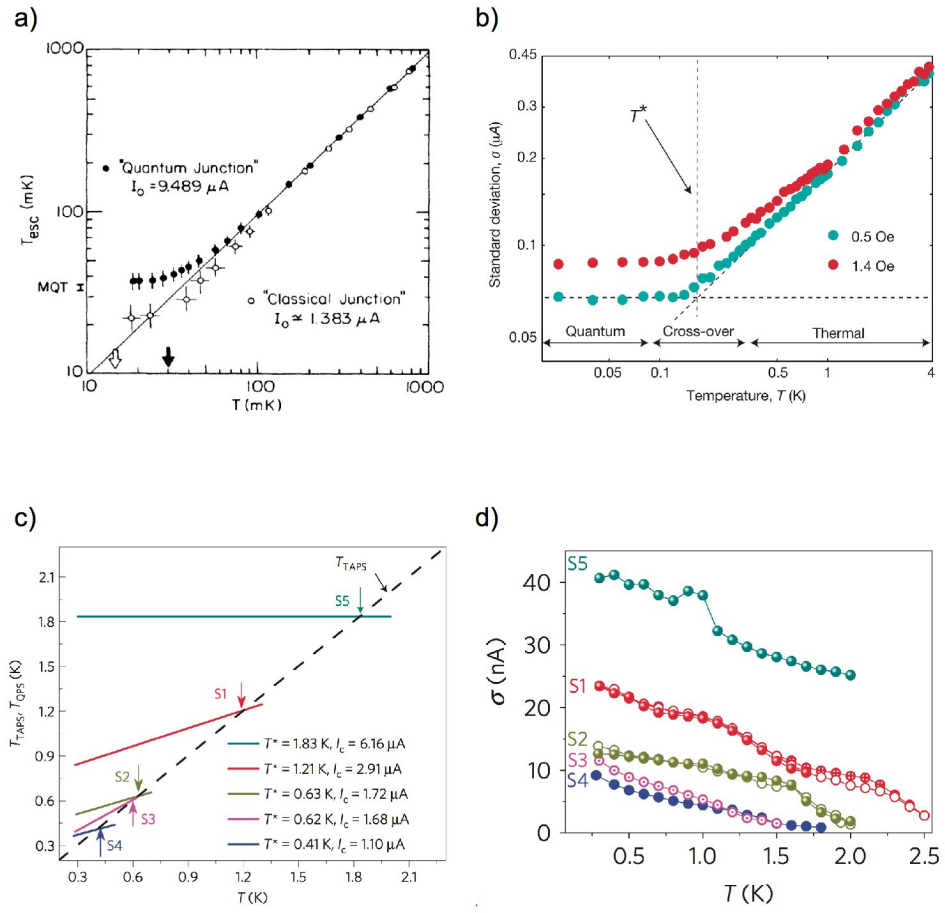

Figure 1.2: Switching Distribution Measurements of Quantum Phase Slips a) From Martinis, Devoret and Clarke [22]. The escape temperature fitting parameter follows true temperature in the thermal region and deviates in the quantum dominated region b) This same effect as shown in a is visible as the saturation of standard deviation at low temperatures and the increase of standard deviation with increasing temperatures in the thermal region. This example is for a vortex in a single Josephson junction is from Wallraff et al. [24] c) The escape temperature fitting function used for nanowires from Sahu et al. [23]. In the quantum region it is more flat than in the thermal region. Note the similarity between a and c. d) Standard deviation vs temperature for nanowires. Opposite to b, standard deviation decreases as temperature increases. There is no clear boundary between the quantum and thermally dominated regimes [23].

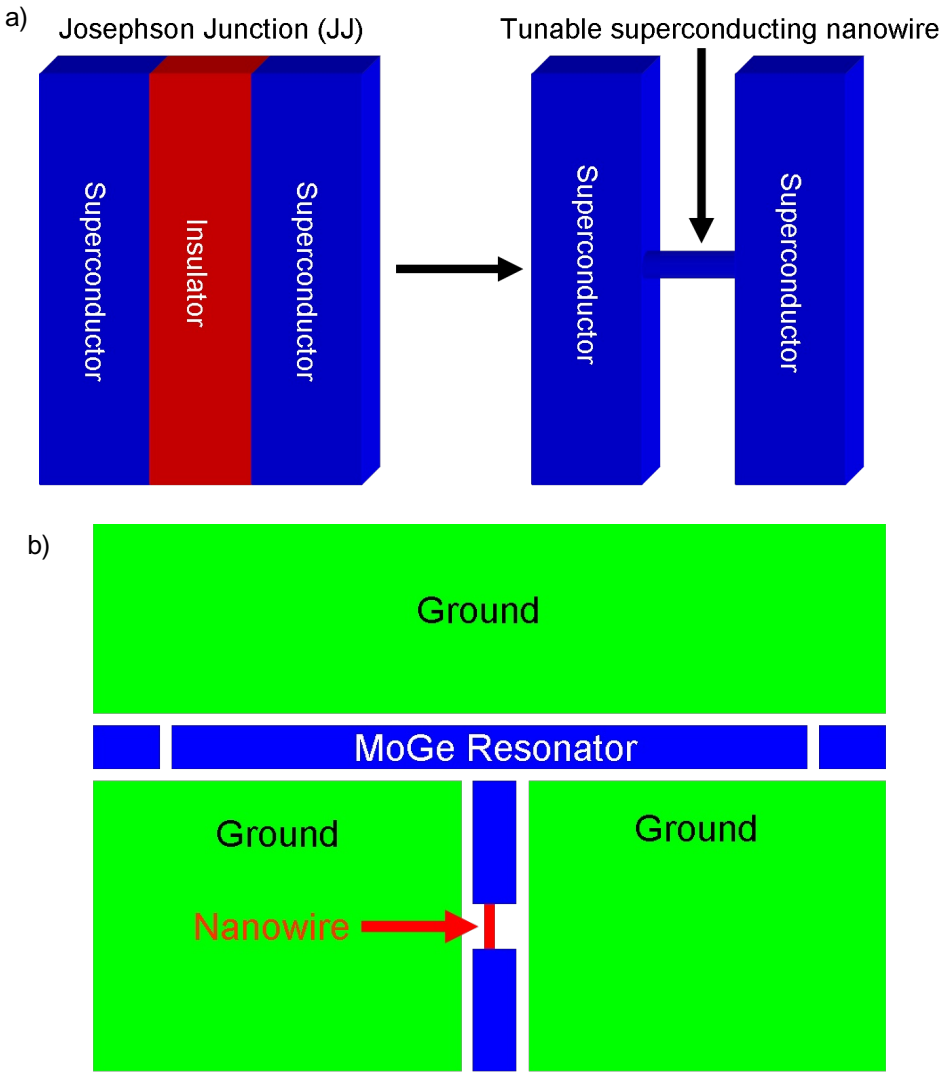

Figure 1.3: Motivation for pulsing a) It might be possible for some applications to use a superconducting nanowire which can be tuned by pulsing, instead of using a Josephson junction. b) In this implementation of a superconducting nanowire qubit, the nanowire is the weak link which picks out the energy levels of the resonator to make a qubit [27]. Exact control of the switching current of the nanowire is necessary for this qubit to work and high bias pulsing provides this control.

Chapter 2 of this thesis will deal with the fabrication steps involved in fabricating the nanowire samples. It contains a description both of the more traditional form of molecular templating to make superconducting nanowires [20] and the fabrication of TEM compatible nanowire samples which were necessary to understand the effects of pulsing on the nanowires. Chapter 3 contains a detailed description of the theory of superconducting nanowires with derivations where appropriate and more extended discussion of the formulas used in later chapters. Chapter 4 describes my experiments on applying high bias voltage pulses to nanowires. This chapter describes the effect of the pulses on the nanowires, an explanation of the counterintuitive return of the switching current with increasing voltage pulses, the demonstration of the setting of the switching current described above and resistance vs temperature analysis. The resistance vs temperature analysis seeks to explore if pulsing sheds new light on the occurrence of QPS in nanowires and compares thermal and quantum models of phase slips. Chapter 5 describes my experiments using switching current distributions on both unpulsed and pulsed nanowires. I demonstrate that by pushing into a new regime of nanowires unexplored previously we find behavior consistent with the similarities between the QPS model for nanowires and the MQT model for JJs. These results confirm and extend Sahu et al. results regarding QPS in nanowires. Chapter 6 is a more detailed description of the nanoslits I developed and their various uses (besides as TEM samples as described in chapters 3 and 4). Chap 7 deals with an alternative form of nanomodification of nanotubes and nanowires using highly focused electron beams rather than high bias voltage pulses.

Chapter 2

Fabrication

2.1 Molecular Templating

2.1.1 Preparing the substrate

The nanowires described in this thesis were fabricated using the method of molecular templating [20]. The overall process is illustrated in figure 2.1. The 500 μm thick, single side polished (SSP), $< 100 >$ silicon wafers used for this process have 500 nm thermal silicon oxide and 60 nm, low-stress, low pressure chemical vapor deposition (LPCVD) silicon nitride on top of them. Electron beam lithography in PMMA resist defines a trench pattern and optical lithography alignment marks (numbers visible by an optical microscope). The electron beam lithography pattern is transferred into the silicon nitride using a SF6 reactive ion etch (RIE). This etch is isotropic for silicon nitride which creates a sloping edge profile in the silicon nitride. This sloping profile is important for later characterizing nanowires that are well suspended across the slit (and thus have the most homogeneous cross-section). It is useful to do a test chip from the wafer to ensure the etching step was successful and the trench is well formed. After the silicon nitride is etched, the wafer is protected with Shipley 1813 photoresist and diced into 4.8 mm by 4.8 mm chips.

For making samples, individual chips are separated out and a cleaning and undercut process is performed. All chemicals (except for the hydrofluoric acid) are placed in new, clean 20 mL scintillation vials to minimize contamination. This process is performed in a fume hood for safety reasons. All chemicals are poured directly from the original bottles

to minimize contamination. The cleaning process consists of a 30 second initial sonication in acetone (to remove the worst of the dirt from the dicing process and the protective photoresist layer). This is followed by a five minute sonication in clean acetone to fully remove the photoresist and e-beam resist layers. A 30 second water agitation in 18.2 MΩ−cm deionized water followed by a 5 minute sonication in 69% nitric acid (to remove potentially contaminating organics) is performed.[1] After the nitric acid, there is another 30 s rinse in deionized water. At this point, I perform a 10 second etch in 49% hydrofluoric acid. Hydrofluoric acid rapidly etches silicon oxide but attacks silicon nitride very slowly. Thus the silicon oxide underneath the slit in the silicon nitride is rapidly removed forming an undercut. This undercut is essential for preventing short circuits from metal deposited in the trench.[2] After the HF undercut, the chip is rinsed in deionized water for 30 seconds, nitric acid for 30 seconds (for further cleaning), deionized water for 30 seconds and then isopropanol (isopropyl alcohol). Finally, it is carefully blown dry with a dry nitrogen gas flow. After the HF undercut is done, no sonication is performed as this would damage the unsupported area of the silicon nitride. The undercut generally extends a few hundred nanometers under the silicon nitride and is often visible in the SEM pictures of the nanowires.

2.1.2 Depositing nanotubes and metal

After the chip is prepared, fluorinated single wall carbon nanotubes (SWNTs) which are always insulating unlike regular carbon nanotubes are deposited on the chip. This is done by sonicating the nanotubes in isopropanol. Unlike regular nanotubes which require polar solvents such as dichloroethylene to be dispersed, fluorinated nanotubes can be dispersed

[1] Nitric acid is caustic and a very aggressive oxidizing acid so it should be handled with care.

[2] Hydrofluoric acid is extremely dangerous and should be handled with the utmost caution. Unlike other acids, it does not necessarily burn if it contacts the skin but will soak into the skin and attack the calcium in the bone. The vapors from HF may interact with the ions used in the neurological system and can result in nervous system damage. We keep calcium carbonate gel for accidental exposures (though any significant exposure should be treated immediately at a hospital) and a special HF neutralizing solution to deal with any spills. HF attacks glass so the HF itself and its waste are kept in a high density polyethylene (HDPE) bottle.

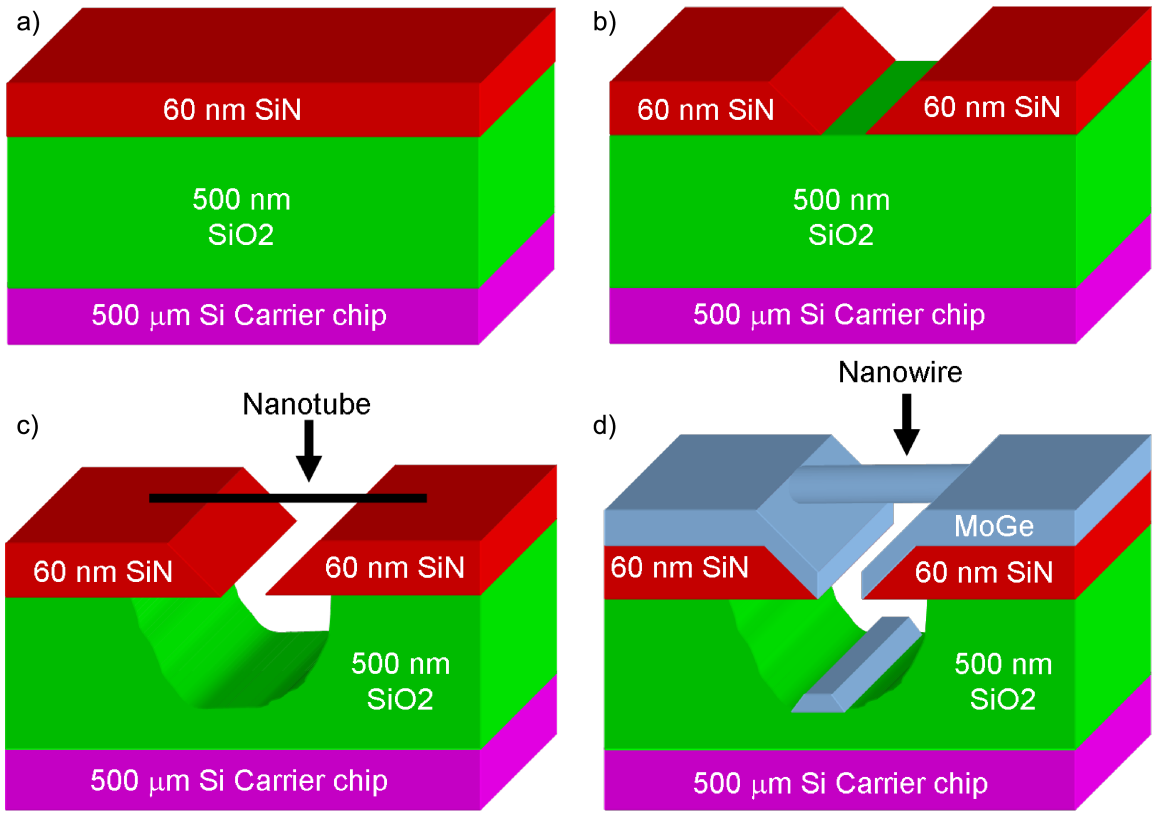

Figure 2.1: a) The starting Si wafer with 500 nm of $SiO_2$and 60 nm of SiN. The drawing is not to scale. b) The wafer after patterning and RIE etching has defined the trench in the silicon nitride. It is at this point that the wafer is diced c) The sample chip after wet etching to form the undercut and deposition of nanotubes d) After metal deposition, the nanotube forms a nanoscaffold forming the nanowire. Note how the undercut prevents unwanted connections along the bottom of the trench

in isopropanol. The chip with nanotubes is sputtered in an AJA sputtering system using a $Mo_{76}Ge_{24}$ target. The $Mo_{76}Ge_{24}$ target is an indium bonded target made from 99.99% pure Mo and 99.999% pure Ge. We avoid using an epoxy bonded targets as we have found the critical temperatures of the resulting films unreliable. A 3-5 minute presputter is performed. This presputter removes contamination particles from the target and coats the inside of the chamber with a thin layer of MoGe to reduce contamination. The presputter is also useful for determining the target is working properly before the samples are inserted. The samples are carbon taped to a sample chuck and inserted into the loadlock (carbon tape is vacuum compatible). The loadlock is pumped within one decade of the main chamber before transfer is performed. The transfer is accomplished by screwing the chuck onto a thread within the main chamber. After transferring, the sample chuck is lowered to the maximum extension to maximize deposition rate and minimize distance between the target and the sample. To minimize contamination from the vacuum of the sputtering system, the base pressure before sputtering begins is reduced to below 1×10^{-7} Torr. This is done using a liquid nitrogen cold trap and may take anywhere from 20 minutes to an hour depending on the condition of the vacuum. In general, we sputter as far after the targets were changed but before the targets are changed again to allow the system to achieve a low starting base pressure. For sputtering, the chamber is pressurized with $0.5 - 2$ mTorr of clean argon gas (we use the lowest sputtering pressures possible such as 0.5-1 mTorr to improve the quality of the film but typically have to tune the pressure slightly for each run). The sputtering rate is monitored by both a crystal monitor and timing the deposition process. Typical deposition rates are 1 Å/second but vary as a function of power. We use DC sputtering at 150 W. Powers higher than about 200 W can cause the indium backing to melt resulting in a short circuit between target and the socket where it is housed. This can be fixed by removing the indium short circuit but requires venting and reinstallation of the target at a later time. After deposition the samples are removed from the sputtering system essentially by reversing all the above steps.

After sputtering the samples are inspected in the FEI dual beam FIB/SEM or the Hitachi S4800 SEM. The FEI SEM produces slightly higher resolution images and has less amorphous carbon growth than the Hitachi S4800 SEM though the Hitachi SEM is somewhat quicker to use. Wires which appear to lie well on top of the trench with solid connections to the superconducting electrodes and with minimal inhomogeneities present are preferentially selected (typically there are several wires with these qualities on every chip so choosing a wire which satisfies these requirements is quite easy). Also, if an appropriate wire is found but a short circuit (such as a second wire or piece of contamination) is too close to it to isolate the wire by photolithography, FIB milling can be used to remove the short circuit. Care is taken so the wire of interest is never exposed to the ion beam. The location of the selected wire is recorded using the numbering scheme written down during the electron beam lithography step. The trench to each side is inspected closely for $\approx 15-20\,\mu$m in either direction (this is the typical width of the bridge used in the photolithography step). If any short circuits are present they are removed by the FIB. This allows us to use photolithography when defining the electrodes of the wire.

Photolithography is performed on the wires to define the electrodes and select just a single wire. The photolithography is performed using the MRL microfabrication class 1000 clean room. The chip is prebaked at 110 °C for five minutes to remove any moisture. Shipley 1813 photoresist is spread on the chip by spinning it at 8000 rpm. The photoresist is postbaked for 1 minute at 110 °C. The photoresist will be flat in the center of the chip and forms a bead at the edge of the chip. A mask with five contact pads and a central bridge of $5-20$ microns is used for for the exposure. The mask is aligned with to the desired wire using the optical markers made in the electron beam lithography step. After exposure the sample is developed in 1:5 Microchem 351 Microposit developer for 30-45 seconds. The pattern is inspected to ensure complete development and that proper alignment was achieved.

After photolithography, the chip is etched in 6% H2O2 to remove MoGe everywhere not protected by photoresist. When the etch is complete, the photoresist is removed using

acetone. The wire is mounted in a chip carrier where 4 thin gold wires have been soldered onto the 4 corner pins (the chip carrier has 6 pins total). Grounding and electrostatic discharge minimization are employed at this step to avoid shocking the wire. The wires are kept in a vacuum pumped desiccator to prevent oxidation of the molybdenum germanium. Wires typically remain usable for at least several months though preferably they are measured within one month of fabrication. SEM images of finished nanowires are shown in figure 2.2. The various instruments used to prepare the wires are shown in figure 2.3.

2.1.3 Cryogenic measurement

Once mounted, the samples are inserted in to a He-4 (base temperature 1.5 K) or He-3 cryostat. Appropriate anti-static steps such as grounding the sample and the person doing the mounting and anti-static spray are again taken to minimize the chance of shocking the nanowire. The He-4 system, constructed by Ulas Coskun, consists of a vacuum compatible dipstick with measurement wires going down the center and a copper heater (wound with heating wire) which can be used to control the temperature. Once mounted the dipstick is pumped to remove air (which would freeze when cooled to liquid helium temperatures). A small amount of helium exchange gas is inserted to allow some thermal coupling between the sample and the liquid helium reservoir. The dipstick is lowered into the liquid helium (typically a few liters are used) after first precooling with liquid nitrogen. The sample quickly reaches ≈ 4.2 K and by pumping on the helium (thereby lowering the boiling point) a base temperature of 1.5 K is reached after approximately 1-2 hours. The sample is measured using a standard four probe measurement (to remove contact resistance). Because of the need for thermal isolation from the room temperature environment down to the sample, high resistive wire is used for all measurement leads. The approximate resistance of each lead is 310 Ω. It should be noted this four probe measurement is of the electrodes and not the nanowire (the electrodes are connected to the nanowire in a two-probe configuration). However, because the electrodes are superconducting and seamlessly connected to the nanowire we consider

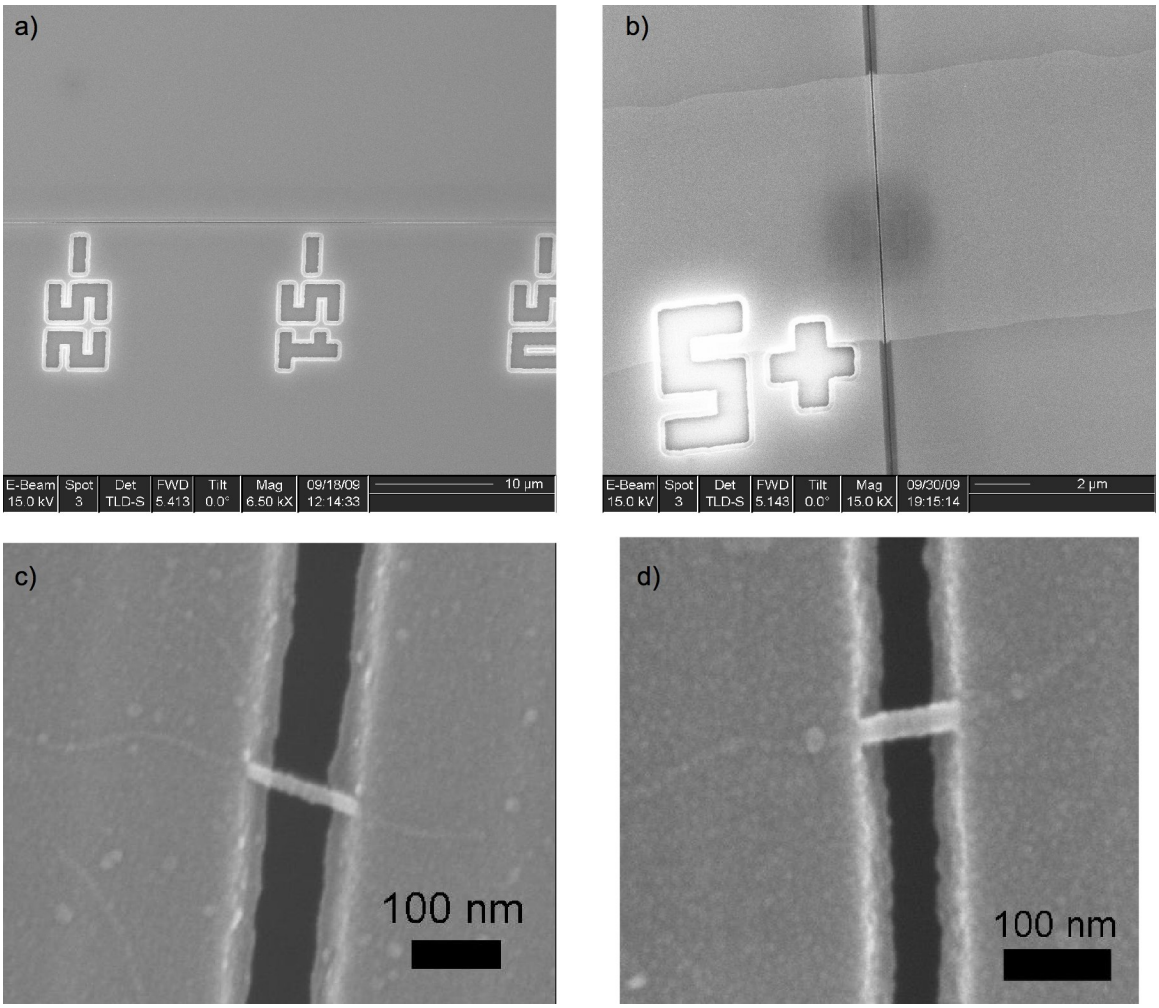

Figure 2.2: Molecular Templating Example a) SEM image of the trench and optical lithography alignment marks b) SEM image of the metal bridge connecting the electrodes to the nanowire after photolithography. The trench and one of the optical lithography alignment marks are visible. The thinnest black line is the trench while the wider dark line is the undercut. The actual nanowire is not visible at this magnification. The width of the metal bridge in this example is about 5μm c) an example nanowire d) another example nanowire

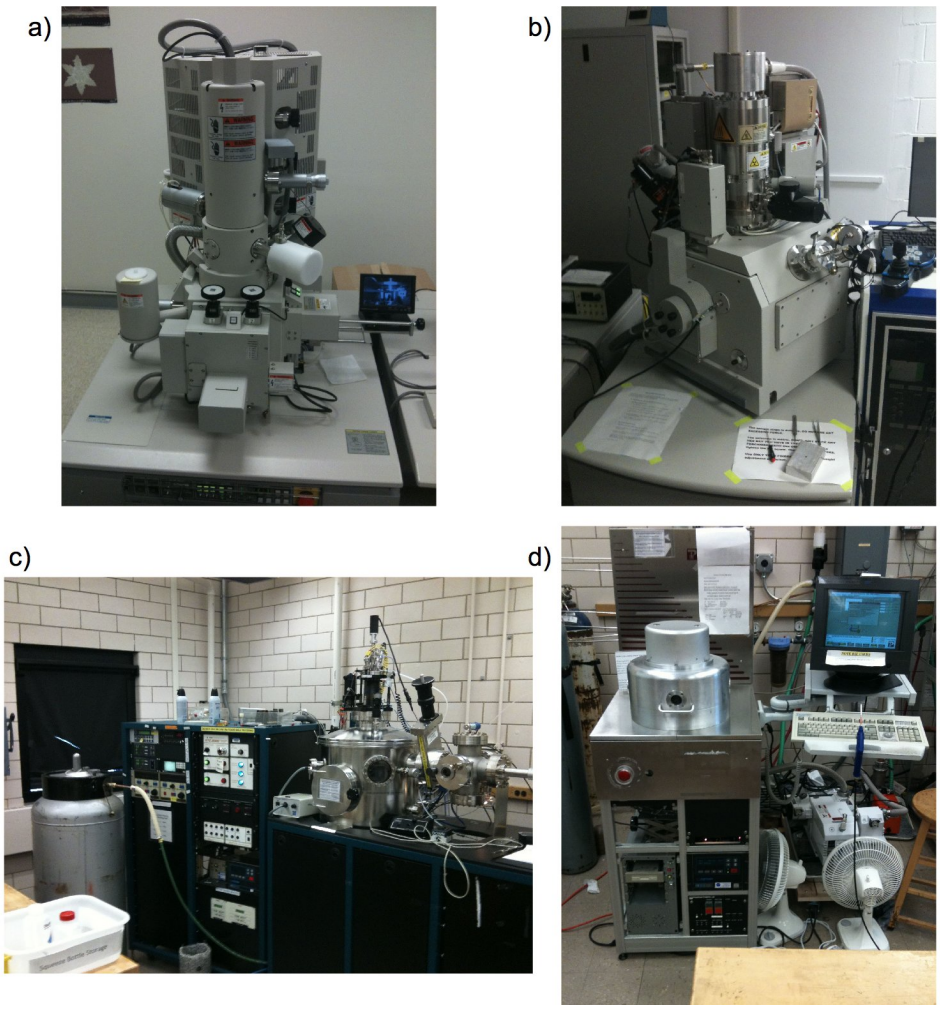

Figure 2.3: Instruments used for wire fabrication a) the Hitachi S4800 scanning electron microscope (SEM) b) the FEI dual beam focused ion beam FIB/SEM c) the AJA sputtering system with cold trap d) the Plasmatherm reactive ion etcher (RIE)

this to be a quasi-four probe measurement. A typical chip carrier, the grounding box and the He−4 system are shown in figure 2.4

The He-3 cryostat is a commercial system from Janis Research Company with the primary wiring for samples done by Andrey Rogachev. It has a similar sample connection to the He-4 system but allows the mounting of two samples rather just one (one sample has electrodes parallel to the magnetic field while one has electrodes perpendicular to the magnetic field). It has in addition to π filters (capacitor-inductor-capacitor low pass filters), a copper powder filter (the small copper powder particles act as inductors to kill high frequencies). Like the He-4 system, air is pumped out of the cryostat and replaced with exchange gas for the initial cooldown. Once the cryostat reaches 4 K, this exchange gas is removed by pumping overnight. The cooling of the He-3 system uses a sorbtion pump. This pump is first heated to 45 K to drive all the He-3 gas out of the charcoal filter inside the pump and down into the He-3 pot. At the same time the 1 K pot is kept at 1.5 K (in the same way the He-4 system is kept at base temperature). Because the condensation temperature of He-3 is 2 K, the 1 K pot is cold enough to allow He-3 to condense in the He-3 pot. Once this liquid He-3 is condensed, the sorbtion pump is allowed to cool thus pumping on the liquid He-3 and reaching a base temperature of 0.3 K. The temperature is measured with a Ruthenium Oxide thermometer using a Lakeshore 370 AC resistance bridge.

A Stanford Research Systems (SRS) ds360 ultra low distortion function generator is connected to a standard resistor R_{std} to form a current source. The voltage across the resistor (typically in the range 0.01-1V) is measured using a SRS 560 low noise voltage preamplifier. A Princeton Applied Research (PAR) 113 voltage preamp is used to measure the two voltage leads. For RT curves, usual settings were: $R_{std} = 1\,\mathrm{M}\Omega$, SRS preamp had 10 gain with a 1 kHz filter, PAR preamp had 1000 gain with a 1 KHz filter. The ds360 source was set to a sine wave with amplitude 10 mV (resulting in a current of 10 nA) with frequency 11.574 Hz. The number of points/second was set to 10,000 while the number of points per cycle was set to 3456 resulting in 4 complete sine wave oscillations for every RT

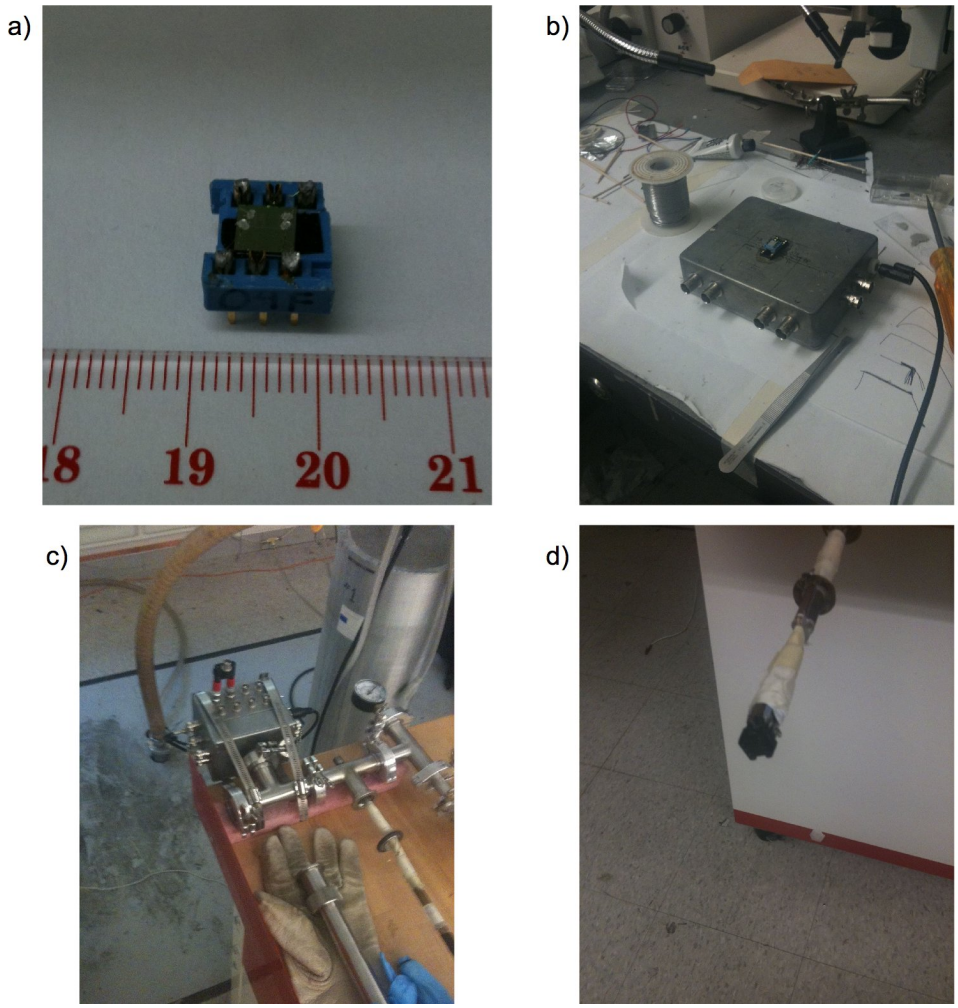

Figure 2.4: Sample measurement and He-4 cryogenics a) a chip mounted in sample holder with 4 gold wires attached with indium dots to the metal electrodes. b) A grounding box used to protect the chip during mounting. The solder is used to connect the gold wires to the chip carrier in a and the tweezers are used to manipulate the chip and wires. c). The top of the He-4 system showing the BNC connections used to connect measurement electronics. d) Bottom of the He-4 system showing the point where the sample carrier in a is plugged in

point collect ($11.574 \times 3456 \approx 40000$). These unusual parameters are used to avoid 60 Hz noise and maximize the lock-in effect.

For VI curves, usual settings were: $R_{std} = 100\,\mathrm{k}\Omega$, SRS preamp had a gain of 1 with a 100 kHz filter, PAR preamp had a gain of 100 with a 100 kHz filter. The ds360 source was set to a sine wave of frequency 11.574 Hz with a suitable amplitude (e.g. 1 V gives $10\,\mu$A. The number of samples per second was 48,000 (the limit of the DAQ card) and number of sample per curve was 4200 ($48000/11.574 \approx 4147$ but ≈ 50 extra points were added to ensure a complete VI curve i.e. slightly more than one cycle was collected). For higher speed VI curves (to speed up the collection of VI curves), the frequency was set to 28.611 Hz and the number of points to 1728. All preamps were battery powered to avoid additional noise and ground loops. The data was collected and analyzed with several custom written Labview programs.

2.1.4 Pulse Set-Up

In order to protect sensitive measurement equipment from high bias pulses (1 V or more) and to allow application of a voltage bias rather than a current bias pulse, a switching system was employed to switch between measurement mode and pulsing mode (see Figure 2.5a). The wire was pulsed between sensitive measurements in order to change its morphology.

Both manually operated switches and automated relays (voltage powered switches controlled by a computer) were used (see figure 2.6). No difference in behavior of the nanowires was observed between the two. The relays were low bias, latching relays powered by a Keithley electrometer controlled by the measurement computer through GPIB. The latching design of the relays allows the power to the relays to be removed without affecting the switch position of the relays. To test the relays, repeated switches were made with no pulse application. No effect on any nanowire was observed from just switching back and forth without pulse application. Square pulses were applied using a data acquisition (DAQ) card. Pulse duration was kept at 100 μs and pulse voltage amplitude was varied. Pulses of this

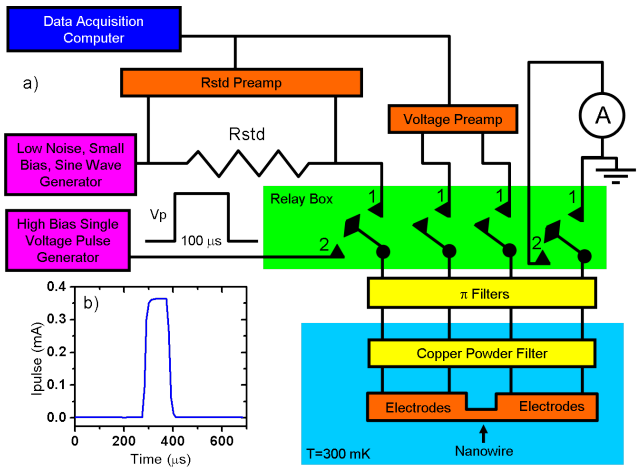

Figure 2.5: Experiment Set-up: a) 4 relays (voltage controlled switches) are used to switch between measurement and pulsing mode. In measurement mode (all relays in position 1), we can measure either voltage vs current curves or resistance vs temperature curves. When measuring the former, a sine wave generator connected through R_{std} = 100 kΩ forms a current source (≈1-10μA) connected to the left lead. When measuring the latter, the sine wave generator is connected through R_{std} = 1 MΩ forming a current source with much smaller amplitude (≈ 10-20 nA). A small voltage (≈1-10mV) is measured on the two center leads. The right current lead is grounded. In pulsing mode (relays in position 2), a single high bias voltage pulse (≈0.1-1V) is sent in on the left current lead, the two center leads are disconnected and the pulse can be detected on the right lead using an ammeter (≈0.1-1 mA). b) Example measured current going through nanowire from a high bias voltage pulse measured with the ammeter. The pulse is 100 μs long and there are minor amounts of rounding of the pulse due to filtering in the cryostat.

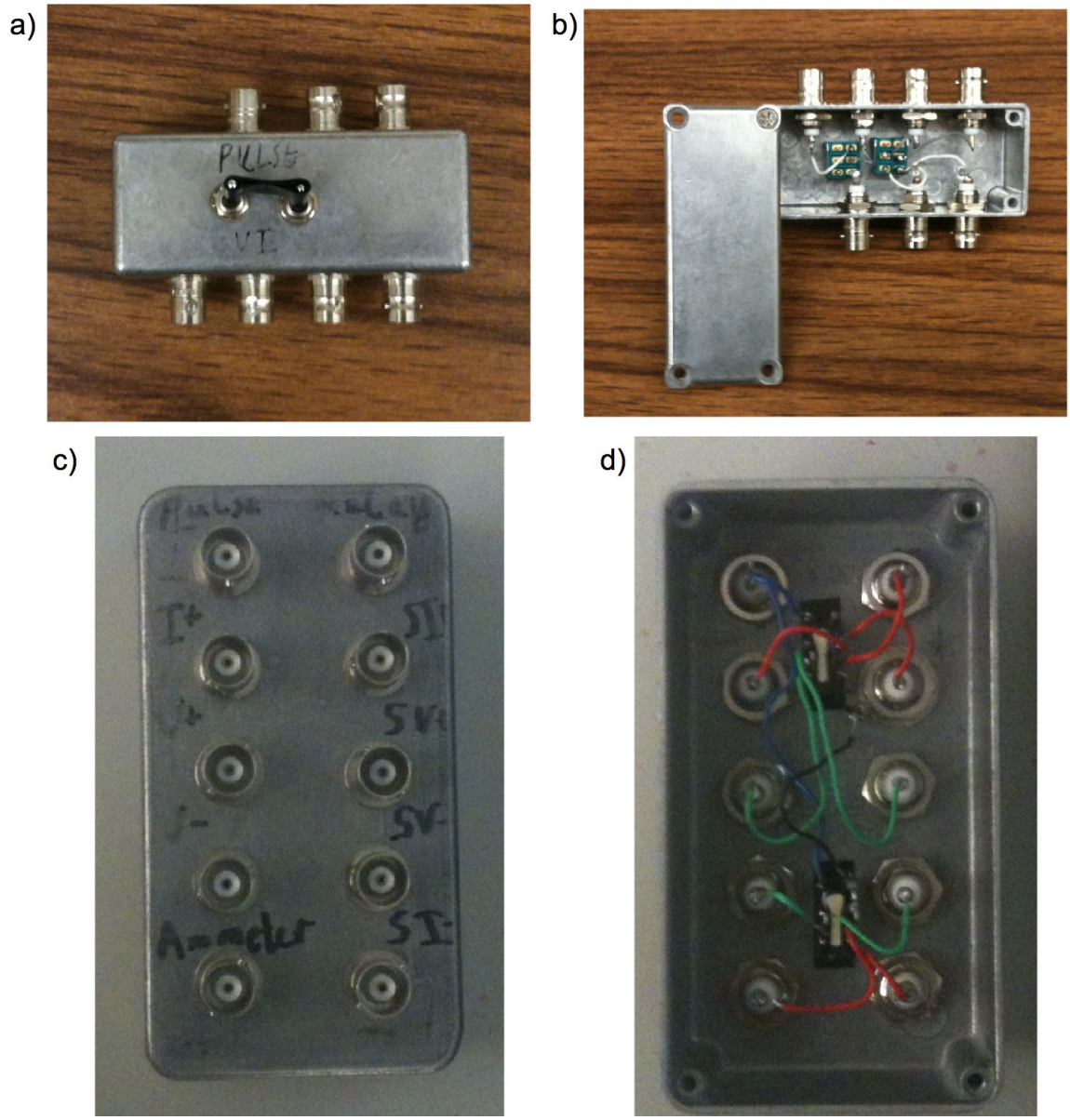

Figure 2.6: The switch box has 4 inputs (pulse, current plus, voltage plus, voltage minus) and 3 outputs (sample current plus, sample voltage plus, and sample voltage minus) The insides of the switch box white wires are inputs and grey wires are outputs. The relay box has a pulse input, a relay control input, $I+$, $V+$ and $V-$ inputs. The sample $I+$, $V+$ $V-$ and $I-$ are hooked up accordingly. The Ithaco current preamp is connected to the ammeter. The insides of the relay box. Each black circuit component contains two relays. The blue wires are the relay control signal to power the relays. The three red wires at the top allow the choice between the pulse and measuring $I+$, the green wires connect $V+$ and $V-$ and the bottom two red wires are for the ammeter connection (the black wires are connected to ground).

length transmit fairly well through the filtering system on the cryogenic measurement systems maintaining their square shape with minimal rounding (see Fig. 2.5b). We have not systematically explored the effect of different length pulses (or different shaped pulses) but we do not expect significant dependence on these two factors for the following reasons. The response time of the nanowire should be on the order of picoseconds (the capacitance of the electrodes is on the order of a few fF [10] while the resistance is approximately 1 kΩ giving a RC time constant of approximately 1-10 picoseconds) so the wire will have reached equilibrium current early in the pulse. The wire is expected to reach its maximum temperature (due to Joule heating) during the pulse and cool back to base temperature after the pulse within 10-100 ns [23] so it should be well thermally equilibrated early in the pulse as well. It should be noted that our relay switching speed (approximately 1 second) is not fast enough to allow us to capture the cooldown back to base temperature after the pulse and the wire is well thermalized before switching currents are measured after a pulse. The current during the pulse was measured with a DL Instruments (Ithaco) 1211 current preamplifier.

2.1.5 TEM Samples

To more thoroughly study the pulses effect on the nanowires, we needed in-situ TEM experiments. TEM compatible samples require a different fabrication process than the SEM compatible samples described previously. Most importantly, the nanowire must be across an open slit for TEM observation. We deposit multi-walled carbon nanotubes (MWNTs) across TEM compatible slits to generate these samples [28]. I will describe how we fabricate these samples in detail below but a brief summary of the process is useful: We use a KOH etch to fabricate a V-shaped cut in a silicon chip coated on both sides with silicon nitride. The V-shaped cut almost pierces the chip except for approximately 5 microns of remaining silicon. This silicon is cracked by very briefly sonicating in deionized water. A short KOH etch removes the cracked silicon leaving an approximately 100 nm wide silicon membrane. This membrane is then etched to form the TEM compatible slit. An alternative to cracking

the silicon is to etch directly with the focused ion beam (FIB). This method provides greater control over the length of the slit but is generally more time consuming and less consistent so it was not used for the majority of the samples presented here. The two processes are illustrated in figure 2.7.

The silicon wafers used are 3" diameter, $< 100 >$ lightly n-doped Czochralski (Cz) double side polished (DSP) silicon wafers with 100 nm of low stress, LPCVD silicon nitride deposited on both sides (Surface Process Group). The wafers are $600 \pm 5\,\mu$m thick. A tight specification on thickness makes choosing the initial mask size easier. The wafers have a total thickness variation (TTV) $< 3\,\mu$m. A small TTV makes the point at which to stop the KOH etch fairly uniform across the wafer. Cleavage lines for the chips are defined by the KOH etch using a corner compensation technique to get rectangular chips [29]. Alternatively, rectangular chips can be defined by dicing after the KOH etch. A transparency mask (5080 dpi transparency printer) was used to define etch pits and cleavage lines using photolithography. We achieved the best accuracy in transparency masks by coding the mask directly in the postscript programming language accepted by the printer rather than using a computer assisted drawing program (CAD) and translating it to postscript. After photolithographic patterning with an appropriately sized mask, the pattern defined in the photoresist was transferred into the silicon nitride by RIE etching using a CHF3/O2 plasma. The photoresist was then stripped in acetone. The wafer was placed in 70 °C KOH (45% by weight, Sigma Aldrich) to etch the silicon anisotropically. A timed etch was performed using a programmable hotplate (Torrey Pines Scientific HS40). Empirically, we found a time of 6 hours to be a satisfactory starting point. At the end of 6 hours, the hot plate automatically switches off. The actual initial etch is longer than 6 hours since etching continues as the KOH etchant cools. Because the $< 111 >$ plane etches much more slowly than the $< 100 >$ or $< 110 >$ plane, a V-shaped etch pit is produced. After the initial etch, etching is continued as before but is now monitored at periodic intervals. Every $15 - 30$ minutes, the wafer is removed from the KOH and placed in a flat polystyrene petri dish (FALCON 351007) filled

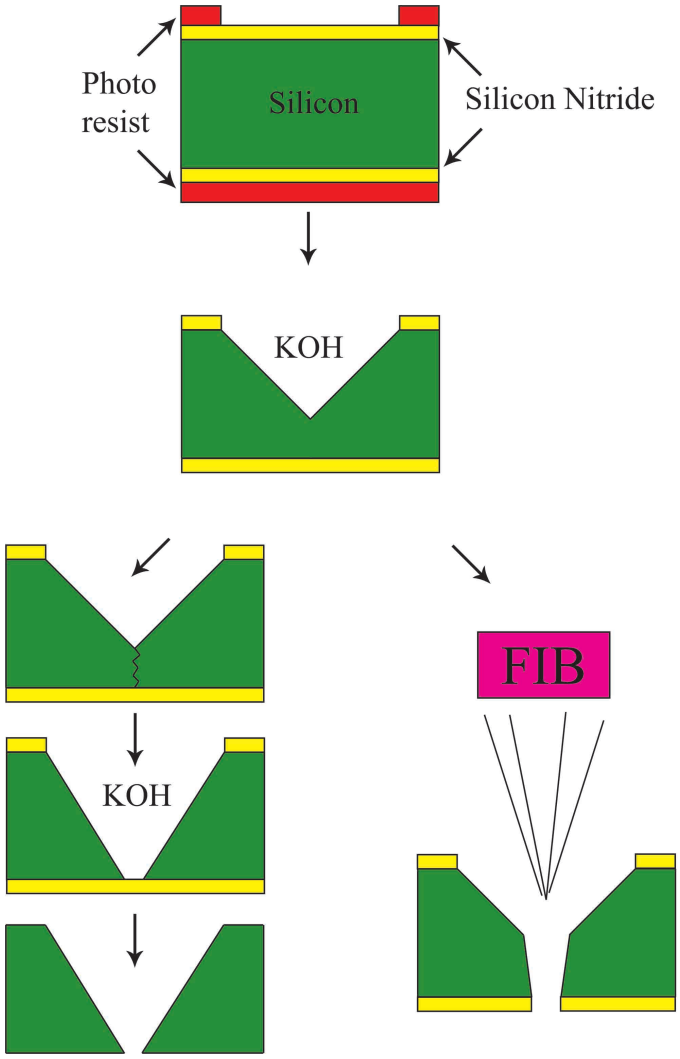

Figure 2.7: Two processes for fabricating nano-slits in macroscopic silicon chips: Starting with a silicon wafer coated with silicon nitride, photolithography followed by reactive ion etching (RIE) is used to define a hard mask in the silicon nitride. KOH etching is used to produce a V-shaped etch pit. The KOH etch is monitored using optical microscopy. When the remaining silicon at the bottom of the etch pit is thin enough, light will penetrate through when the sample is back-lit. From this point, two different fabrication routes can be followed. On the left, $\approx 100\,\text{nm}$ scale slits are produced using only low- resolution technology. The thin silicon is first cracked using brief sonication in deionized water. Further KOH etching of the crack produces a silicon nitride membrane $\approx 100 - 200\,\text{nm}$ wide. Stripping the silicon nitride produces a narrow slit. On the right, focused ion beam (FIB) milling is used to directly make $\approx 100\,\text{nm}$ scale slits through the thin silicon. This method offers more control over the length and width of the slit than the process on the left but relies on high-resolution technology.

with the minimum amount of deionized water needed to cover the sample. The wafers are inspected in an optical microscope with a strong back light (VWR VistaVision T-RTP). When the silicon is sufficiently thin (we estimate $\approx 5\,\mu$m from FIB cross sections), a thin red line will be visible in the optical microscope from the back light penetrating the chip. At this point, KOH etching is stopped by a rinse in deionized water, nitric acid, deionized water, and then isopropanol. The wafer is then blown dry with nitrogen gas. These red-line samples are the starting point for the various processes described. Using a wafer with a tight TTV as described, the majority of the wafer will become red-line chips at around the same time. The chips were cleaved and separated at this point before further processing was performed to minimize stress on the slit. The mask used was designed by calculating the width of the mask required to just etch through the wafer. Using simple trigonometry, it can be derived (from the angle the etch pit makes relative to the surface of the chip, $\tan^{-1}\sqrt{2} \approx 54.7$) that this width follows the formula $w = h\sqrt{2}$ where h is the thickness of the wafer and w is the width of the mask required to just etch through the wafer. For a $600\,\mu$m thick wafer, the width of the mask should be $600 \times \sqrt{2} \approx 849\,\mu$m. The variation in wafer thickness of $\pm 5\,\mu$m implies the mask width should be between $595 \times 2 \approx 841\,\mu$m and $605 \times 2 \approx 855\,\mu$m. Because we manually align to the flat of the wafer, we get some undercut from the etch so an undersized mask was used. If we use only one size mask, the etching time can vary by several hours just from the variation in thickness between separate wafers. Therefore, we performed a test etch with varying size etch pits on a small piece of the wafer. The test mask had etch pits ranging from $790 - 830\,\mu$m in $5\,\mu$m increments. The test mask and corresponding wafer sized masks can all be included on a single transparency. We have also tried this fabrication process on wafers with a much larger uncertainty in thickness ($\pm 25\mu$m). The large variation in thickness made it more difficult to choose an appropriate sized photomask. We had to use a significantly under sized mask and use long etching times. If the photomask used is significantly undersized, the KOH etch cannot be completed in a reasonable amount of time (several hours). In this case, tetramethylammonium hydroxide (TMAH) (Sigma Aldrich)

etch was used since it etches the $< 111 >$ plane of silicon more quickly than KOH. In this case, we did an etch of TMAH for three hours and KOH etch for one hour until we reached a red-line state. However, with more uniform wafers, a properly sized mask and a test mask, this step was unnecessary. Wafers with less tight TTVs tended to reach the red-line state at different etching times across the wafer. This required stopping the etch when some of the samples were ready, separating out samples that were not ready and continuing the etch independently for each samples that did not yet have light penetrating it when back lit. Using a wafer with TTV$< 3\,\mu$m had most of the wafer reach the red line state at roughly the same time and allowed stopping of the etch on the entire wafer simultaneously. Once a red-line chip is formed, we can fabricate ≈ 100 nm scale slits in it using only sonication and wet etching. A red-line chip is briefly (less than 1 second) sonicated in deionized water. This sonication breaks the silicon along the thinnest point, which is the tip of the V-shaped etch pit. The silicon nitride on top of the silicon does not typically break. The chip is then etched in 70 °C KOH for $1 - 5$ min. Every 30 seconds, the chip is removed from the KOH, placed in a petri dish with the minimum amount of DI water needed to cover the chip and examined under an optical microscope. When the slit appears to have etched to an appropriate size, the chip is cleaned in nitric acid, deionized water, isopropanol and then blown dry with nitrogen gas. Once dry, the chip is inspected under the optical microscope again. Although the optical microscope is inherently inaccurate at this small scale, we can consistently produce slits on the order of 100 nm wide. The inaccuracy of the optical microscopy feedback and sizing by eye produces a spread in slit sizes of ≈ 100 nm amongst different chips. The silicon nitride typically survives to form a membrane across the narrow silicon slit. A few isolated sections of the slit are unusable from damage done by the sonication step but the majority of the slit is a usable, uniform $\approx 100 - 200$ nm slit. To form an actual slit, we can either strip the silicon nitride in 115 °C phosphoric acid for 40 minutes (as is described in the paper [28]) or etch the membrane away with the RIE (which is a simpler and quicker method we developed later). The membrane is removed by RIE etching from the etch pit

side. The membrane is supported during the RIE step by a piece of polydimethylsiloxane (PDMS). By etching the silicon nitride from the etch pit side, we are able to use the silicon nitride as the insulating layer thus skipping the oxidizing step that is necessary when using phosphoric acid (since all the silicon nitride is removed). It should be noted that the edges of the slit are generally more ragged with the RIE method than the wet etch method. Once the slit is formed, MWNTs were deposited by crushing MWNT powder between two pieces of PDMS and then applying the PDMS to the slit [30, 31]. The slit was shadow masked with strips of polydimethylsiloxane (PDMS, Sylgard 184) in an H shaped pattern. MoGe was deposited as before. These slits are particularly susceptible to clogging once formed so wet chemical treatments and photolithography are avoided. Unwanted nanowires and debris crossing the slit were instead removed using FIB milling. Care was taken so the nanowire to be measured was not exposed to the ion beam. In order to minimize the amount of FIB work the PDMS mask was designed so only $\approx 100\,\mu$m of the 1 mm slit received metal. The sample was mounted in a specially designed TEM specimen holder that allows electrical contact to the sample in situ [32]. Electrical transport measurements and simultaneous TEM imaging were performed (see figure 2.8). To avoid electron beam induced crystallization in our TEM images, dosage from the electron beam was minimized for all TEM images.

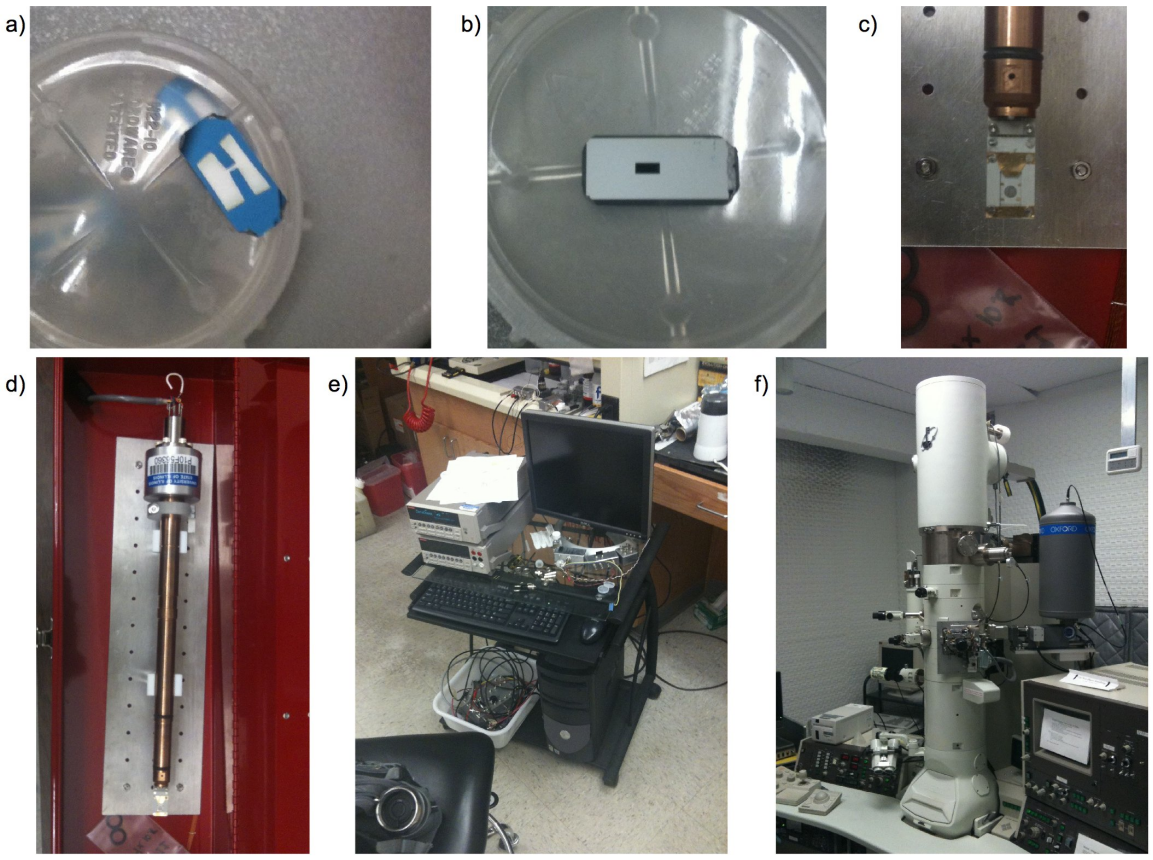

Figure 2.8: Front of a typical TEM chip showing the H shaped electrodes. The silver color is metal while the blue is the insulating silicon nitride. The trench is too small to be seen. Back side of the TEM chip showing the etch pit. The grey color is the exposed silicon (from etching the silicon nitride from the back using the RIE). the JEOL 2010F field emission gun 200 keV TEM used for the TEM experiments. The portable measurement station used to pulse and collect data during the in-situ TEM measurements. The MEMS TEM holder compatible with the TEM chips. close up of the MEMS TEM holder. Between the clips the four probes that contact the electrodes on the chip can be seen

Chapter 3

Theory

3.1 Introduction

Our primary theoretical task is to describe the behavior of one-dimensional superconducting nanowires so we can compare theory to experimental data such as resistance versus temperature curves or switching current distributions. In Ginzburg-Landau (GL) theory, the current in a one-dimensional nanowire is described by a complex order parameter with constant amplitude which can be visualized as a helix as shown in figure 3.1a. Application of a voltage would result in the increase in phase, i.e., the tightening of this helix. Little [2] developed the notion of a phase slip whereby a local fluctuation drives the order parameter to zero. Essentially, a small section of the wire goes normal destroying the phase coherence and allowing one coil of the wound up helix to slip by 2π (see figure 3.1b). This phase slip process allows the progression of phase according to the expected Josephson rate but at currents less than the critical current. These phase slips occur along the nanowire stochastically and are important because the rate of phase slips defines the voltage drop as can be seen from the Josephson relation:

$$V = \frac{\hbar}{2e}\frac{d\phi}{dt} = \frac{\hbar}{2e}2\pi\Gamma \tag{3.1}$$

where Γ is the rate of phase slips. Thus the rate of phase slips entirely governs the voltage across and therefore the resistance of the superconducting nanowire. A theoretical model for the rate of phase slips can thus be compared to experimentally accessible data such as the resistance vs temperature (measured at low bias current) or the switching current at a

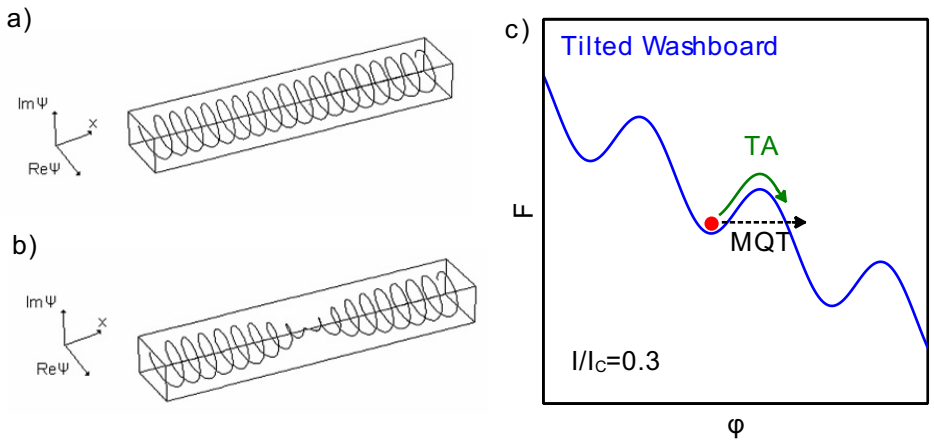

Figure 3.1: The phase slip process for one dimensional nanowires. a) The phase evolves with constant amplitude winding around in the complex plane. A phase slip is a reduction of the order parameter amplitude to zero thus allowing a turn of the helix to be added or removed. b) An energy barrier exists for the phase slip process similar to the tilted washboard for Josephson junctions. To change the phase by 2π the free energy barrier must be overcome by either thermal activating (TA) over the barrier or quantum tunneling through the barrier (MQT). The tilt of the washboard is controlled by the ratio I/I_C. As this ratio gets larger, the free energy barrier for phase slips becomes smaller.

particular temperature (measured at high bias current). Thus the more we can say about the phase slip rate, the more we can accurately describe our experimental data.

Driving a section of the wire normal during the phase slip has an energy cost associated with it that serves as a free energy barrier for the phase slip to occur. We can represent this barrier in similar form to the "tilted washboard" potential of a Josephson junction (since it must be 2π periodic) as shown in figure 3.1. A phase slip corresponds to an escape from a well of the potential. The simplest way for this escape to occur is by thermally activating over the barrier. Not surprisingly, the phase slip rate associated with this process of thermally activated phase slips (TAPS) is given by a simple Arrhenius law:

$$\Gamma_{TAPS} = \frac{\Omega}{2\pi} \exp\left(-\frac{\Delta F}{kT}\right) \tag{3.2}$$

The frequency in front, $\Omega/2\pi$, is the characteristic unit of time associated with the phase slip rate. While this frequency is theoretically challenging to calculate [33, 34], the exact value

is typically not particularly important as the exponential will dominate the expression. The phase slip rate, Γ is sometimes called the escape rate as it would represent the phase slip happening by "escaping" over the free energy barrier, ΔF. If the phase can be described as a quantum mechanical object, one would imagine that it would be possible for the phase to "tunnel" through the barrier in accordance with the laws of quantum mechanics. The rate associated with quantum tunneling of phase slip (QPS) is given most simply by a Wentzel-Kramers-Brillouin (WKB) approximation:

$$\Gamma_{QPS} = \frac{\Omega}{2\pi} \exp\left(-2\pi \frac{\Delta F}{\hbar \omega_p}\right) \tag{3.3}$$

where ω_p would be the plasma frequency. This is the heuristic MQT model for quantum phase slips proposed by Giordano [14,15], where ω_p is expected to be on the order of $1/\tau_{GL}$ for a nanowire. Again, Ω is a characteristic frequency which is theoretically difficult to calculate [14–16, 19] but its exact value will not be particularly important since it is dominated by the exponential. Following Martinis et al. [22], we note the similarity between equation (3.2) and (3.3). We will at times find it advantageous to write an effective temperature, T_q, where $k_B T_q = \hbar \omega_p / 2\pi$. We can then define an effective Arrhenius law:

$$\Gamma = \frac{\Omega}{2\pi} \exp\left(-\frac{\Delta F}{k T_{esc}}\right) \tag{3.4}$$

where $T_{esc} = T$ in the thermally dominated region and $T_{esc} = T_q$ in the quantum dominated region. The condition $kT < \hbar \omega_p / 2\pi$ is a necessary condition for the observation of QPS. Both thermal and quantum escape are strongly dependent on the free energy barrier, ΔF, associated with phase slips. We will need to develop theoretical descriptions of the free energy barrier as a function of current and temperature in order to describe the experimental data. First, however, we will look at the connection between these phase slip rates and the resistance vs temperature behavior.

3.2 Resistance as a function of Temperature

Equation (3.2) implies that the resistance associated with TAPS is proportional to the exponential. The characteristic unit of resistance is R_N so following Bezryadin [12] and Chu et al. [35], our TAPS resistance expression is:

$$R_{TAPS}(T) = R_N \exp\left(-\frac{\Delta F(T)}{kT}\right) \tag{3.5}$$

Likewise, our QPS resistance expression is

$$R_{QPS}(T) = R_N \exp\left(-2\pi\frac{\Delta F(T)}{\hbar\omega}\right)$$

Note that for TAPS in nanowires the more traditional resistance expression is that by Langer, Ambegaokar, McCumber and Halperin (LAMH) [33, 34]:

$$R_{LAMH}(T) = R_Q \frac{\hbar\Omega}{kT} \exp\left(-\frac{\Delta F(T)}{kT}\right) \tag{3.6}$$

where $\Omega = \frac{L}{\xi}\left(\frac{\Delta F}{kT}\right)^{1/2}\frac{1}{\tau_{GL}}$ and τ_{GL} is the GL relaxation time $1/\tau_{GL} = 8k(T_C - T)/\pi\hbar$. As suggested by Newbower et al. [5], improved fits can be obtained by including the normal resistive channel as a parallel shunt thus $R_{total}^{-1} = R_{LAMH}^{-1} + R_N^{-1}$. LAMH theory has been experimentally validated over several orders of magnitude in long tin whiskers [4,5]. However, despite excellent fits to short nanowires (again over several orders of magnitude) [6], concerns exist about the validity of using the McCumber-Halperin prefactor (which comes from time dependent GL theory) for short nanowires [36]. Overall, the prefactor's exact value is of limited importance as both equations (3.6) and (3.5) are entirely dominated by the behavior of the exponential. We avoid this question of validity by using the phenomenological Little fit of equation (3.5) rather than the LAMH expression (3.6). It should be noted that both fits produce similar fitting parameter values with Little fits typically having a slightly lower

T_C and $\xi(0)$ than LAMH fits.

3.3 Elements of Ginzburg Landau Theory

In order to determine the free energy barrier behavior as a function of current, we will need to describe some elements of GL theory pertaining to superconducting nanowires. In Ginzburg Landau theory, the density of the superconducting electrons (the superfluid density) is set equal to the magnitude squared of a complex order parameter i.e. $n_S = |\psi|^2$. Doing this allows the expression of the free energy density as an expansion of ψ:

$$f = f_{n0} + \alpha|\psi|^2 + \frac{\beta}{2}|\psi|^4 + \frac{1}{2m^*}\left|\left(\frac{\hbar}{i}\nabla - \frac{e^*}{c}\mathbf{A}\right)\psi\right|^2 + \frac{h^2}{8\pi} \tag{3.7}$$

where

$$\alpha = -\frac{e^{*2}}{m^*c^2}H_C^2(T)\lambda_{eff}^2(T) \tag{3.8}$$

$$\beta = \frac{4\pi e^{*4}}{m^{*2}c^4}H_C^2(T)\lambda_{eff}^4(T) \tag{3.9}$$

$$\lambda_{eff}^2 = \frac{m^*c^2}{4\pi|\psi|^2e^{*2}} \tag{3.10}$$

Note $m^* = 2m_e$ is the mass of a Cooper pair, $e^* = 2e$ is the charge of a cooper pair and λ_{eff} is the London penetration depth. Minimizing this free energy, using a variational approach, produces the GL differential equations:

$$\alpha\psi + \beta|\psi|^2\psi + \frac{1}{2m^*}\left(\frac{\hbar}{i}\nabla - \frac{e^*}{c}\mathbf{A}\right)^2\psi = 0 \tag{3.11}$$

$$\mathbf{J} = \frac{e^*}{m^*}|\psi|^2\left(\hbar\nabla\varphi - \frac{e^*}{c}\mathbf{A}\right) = e^*|\psi|^2\mathbf{v}_S \tag{3.12}$$

where $\mathbf{J}$ is the supercurrent, $\mathbf{v}_S$ is the supercurrent velocity and φ is the polar part of $\psi = |\psi|e^{i\varphi}$.

3.3.1 GL coherence length of a dirty superconductor

If we assume there are no fields, $\mathbf{A} = 0$, we can write equation (3.11) as:

$$\frac{\hbar^2}{2m^*|\alpha|}\frac{d^2f}{dx^2} + f - f^3 = 0 \tag{3.13}$$

where $f = \psi/\psi_\infty$ and $\psi_\infty^2 = -\alpha/\beta > 0$. This makes the characteristic length for variation or GL coherence length to be:

$$\xi^2(T) = \frac{\hbar^2}{2m^*|\alpha(T)|} \tag{3.14}$$

A true one dimensional superconductor is a system where at least 2 of the dimensions are much less than $\xi(0)$ and the third is much larger than $\xi(0)$. For our wires, typical dimensions are diameter 20-30 nm and length 100 nm while $\xi(0)$ could be expected to be on the order of 10 nm so they do not rigorously fit the limit of being a one dimensional superconductor. However it has been shown that wires up to 4.4 times the coherence length can still be considered quasi-one-dimensional since they are still too small to support a vortex [37]. Thus our wires are quasi-one-dimensional and display the properties of a true one dimensional wire.

For a dirty superconductor (the mean free path, ℓ, is much smaller than the coherence length, $\xi(0)$), the GL coherence length is related to the Pippard or BCS coherence length by:

$$\xi(T) = 0.855\sqrt{\frac{\xi_0\ell}{(1 - T/T_C)}}$$

where $\xi_0 = \hbar v_F/(\pi\Delta(0))$ is the BCS coherence length and $\Delta(0) = 1.76kT_C$ is the BCS energy gap at zero temperature Combining these equations we can write an expression for dirty superconductors relating $\xi(0)$ to the mean free path, the Fermi velocity ($v_F \approx 10^6\,\mathrm{m/s}$) and the critical temperature:

$$\xi(0) = 0.855\sqrt{\frac{l\hbar v_F}{\pi 1.76 k_B T_c}}$$

Our MoGe wires are certainly in the dirty limit as the mean free path, $l \approx 3 - 4\,\text{Å}$ is much smaller than the coherence length, $\xi(0) \approx 7\,\text{nm}$.

3.3.2 Free energy barrier

Obviously, to calculate the phase slip rate, Γ, we need to know the free energy barrier, ΔF. The free energy barrier necessary for the phase slips was first calculated by Langer and Ambegaokar [33]. The final form of the free energy is:

$$\Delta F = \frac{8\sqrt{2}}{3}\frac{H_c^2(T)}{8\pi}A\xi(T) \tag{3.15}$$

The form of $\Delta F(0)$ can be anticipated (besides a numerical factor of order unity) by remembering that the condensation energy of the superconducting state per unit volume is:

$$\frac{H_C^2}{8\pi} = f_n - f_s$$

Thus equation (3.15) is equivalent to the condensation energy per unit volume multiplied by the volume of a phase slip. The volume of a phase slip is taken to be roughly the cross-sectional area of the wire, A, times the coherence length, $\xi(T)$. The coherence length is the length scale on which a phase slip would be able to occur. Since $H_C(T) \propto 1 - T/T_C$ and $\xi(T) \propto (1 - T/T_C)^{-1/2}$, we can write a GL temperature dependence: $\Delta F \propto (1 - T/T_C)^{3/2}$. It is informative to rewrite equation (3.15) with the temperature dependence explicitly extracted: $\Delta F = \Delta F(0)(1 - T/T_C)^{3/2}$ where

$$\Delta F(0) = \frac{8\sqrt{2}}{3}\frac{H_C^2(0)}{8\pi}A\xi(0) \tag{3.16}$$

Note that by writing $\Delta F(T)$ in this form we can replace the GL temperature dependence with a more accurate temperature dependence and thus extend GL theory further from T_C than would otherwise be possible.

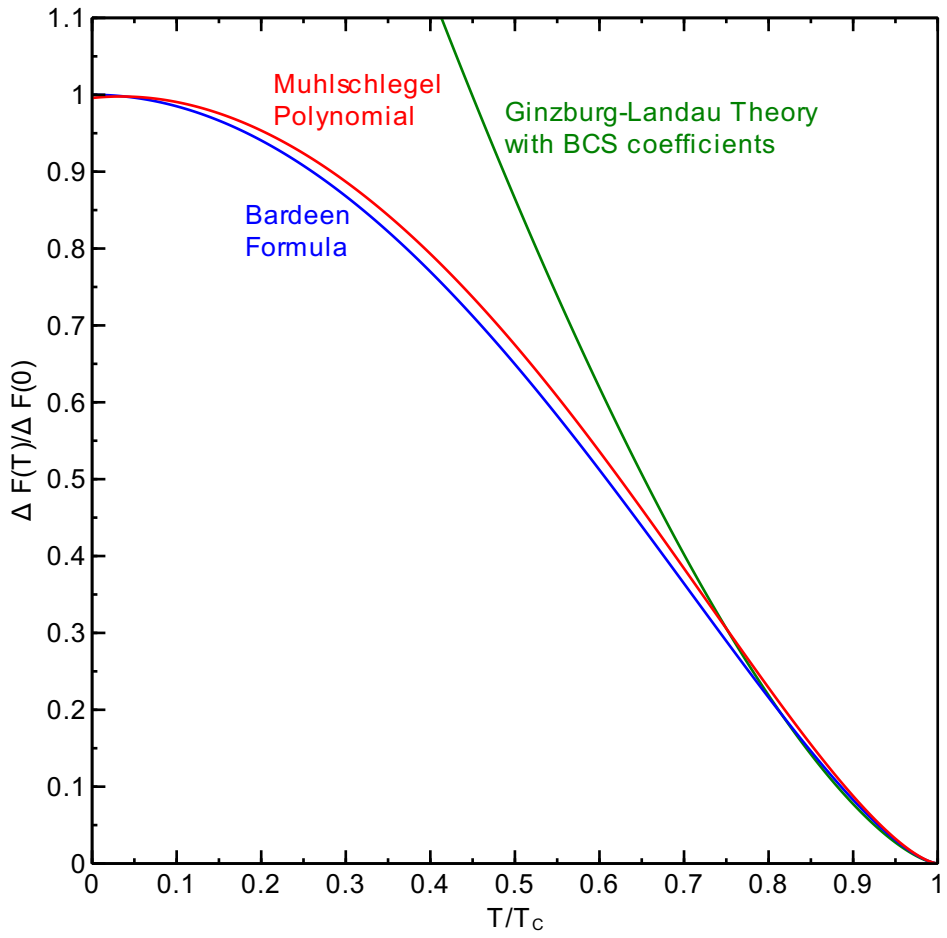

Figure 3.2: Comparison of the temperature dependences for the free energy barrier from Ginzburg Landau theory with coefficients from BCS theory (equation 3.17), the polynomial fit to Muhlschlegel's numerical data for $H_C(T)$ (equation 3.19 combined with the two-fluid temperature dependence of $\xi(T)$ (equation 3.18) and Bardeen's expression based on experimental approximations (equation 3.20). There is a high level of agreement between the two latter expressions indicating there is agreement on the temperature dependence of the free energy barrier at temperatures far below T_C. Close to T_C the GL expression agrees with the other two.

For example, using GL theory with coefficients calculated using BCS theory in the limit $T \approx T_C$: $Hc(T)/H_C(0) = 1.73(1 - T/T_C)$ and $\xi(T) = \Phi_0/(2\sqrt{2}\pi H_C(T)\lambda_{eff}(T))$ where $\Phi_0 = hc/2e$ is the flux quantum and $\lambda_{eff}(T)/\lambda_{eff}(0) = [2(1 - T/T_C)]^{-0.5}$. We can thus extract a more accurate GL temperature dependence for the free energy barrier

$$\Delta F(T)/\Delta F(0) = 1.73\sqrt{2}(1 - T/T_C)^{3/2} \tag{3.17}$$

Another method is to use the two-fluid temperature dependence of the coherence length: $\xi(T)$:

$$\frac{\xi(T)}{\xi(0)} = \sqrt{\frac{1 + (T/T_C)^2}{1 - (T/T_C)^2}} = \frac{\sqrt{1 - (T/T_c)^4}}{1 - (T/T_c)^2} \tag{3.18}$$

We can also express the temperature dependence of $H_C(T)$ from a polynomial fit to numerical work by Muhlschlegel [3, 23, 38]:

$$\frac{H_c(T)}{H_c(0)} = 1.73\left(1 - \frac{T}{T_c}\right) - 0.40087\left(1 - \frac{T}{T_c}\right)^2 - 0.33844\left(1 - \frac{T}{T_c}\right)^3 + 0.00722\left(1 - \frac{T}{T_c}\right)^4 \tag{3.19}$$

Alternatively, Bardeen [39] used experimental approximations to produce a closed form temperature dependence for critical currents (which is the same as the temperature dependence for the free energy barrier as I will show below):

$$\frac{\Delta F(T)}{\Delta F(0)} = \left(1 - (T/T_C)^2\right)^{3/2} \tag{3.20}$$

A comparison between these different temperature dependencies is shown in figure 3.2. As can be seen, there is a high level of agreement between the Bardeen expression and the polynomial expression with the GL expression diverging away from T_C. For simplicity, we will use the Bardeen expression.

3.3.3 Relationship between free energy barrier and critical current

From equation (3.15) we can derive an expression relating I_C to ΔF. Since $I_C = J_C A$, it can be shown from GL theory that

$$J_C = \frac{cH_C}{3\sqrt{6}\pi\lambda}$$

and

$$\Phi_0 = 2\sqrt{2}\pi H_C \lambda \xi$$

This implies

$$I_C \frac{\hbar 2\pi}{2e} = \frac{H_C}{3\sqrt{3}} 2H_C \xi A$$

$$I_C \frac{\hbar}{2e} = \frac{H_C^2}{8\pi} \frac{8}{3\sqrt{3}} \xi A = \frac{1}{\sqrt{6}} \Delta F$$

$$\Delta F = \sqrt{6} \frac{\hbar I_C}{2e} \tag{3.21}$$

which matches the expression from Tinkham and Lau [40]. This equation is the reason why we can use Bardeen's temperature dependence for critical currents, equation (3.20), for the free energy barrier.

For high bias currents, this expression is slightly modified. Tinkham found a closed form expression [41] which fits the Langer Ambegaokar (LA) model [33] for this case:

$$\Delta F = \frac{\sqrt{6}\hbar}{2e} I_C(T) \left(1 - \frac{I}{I_C(T)}\right)^{5/4} \tag{3.22}$$

3.4 Basics of Josephson Junction and RCSJ model

A very short wire, $L << \xi(0)$ should have a current phase relationship similar to a Josephson junction (JJ). Although all our wires are significantly longer than this limit ($L \approx 10\xi(0)$),

it is instructive to look at JJs for theoretical guidance in dealing with nanowires. I will derive in this section some of the well known properties of JJs primarily to set the stage for a similar look at nanowires.

We start from the Josephson relations [42, 43]:

$$I_S = I_C \sin\phi \text{ and } V = \frac{\hbar}{2e}\frac{d\phi}{dt} = \frac{\hbar}{2e}\dot{\phi} \tag{3.23}$$

where I_S is the supercurrent, I_C is the critical current and ϕ is the phase. If we assume the Josephson Junction (JJ) is shunted by a capacitor C and a resistor R (the normal resistance) and we bias the entire system with a current I, we can write down the total current as the sum of the currents through each of the three paths:

$$I = I_C \sin\phi + V/R + \dot{V}C \tag{3.24}$$

This is commonly known as the McCumber-Stewart resistively and capacitively shunted junction (RCSJ) model [44, 45]. Notice that if we instead assumed there was no shunting resistor and that we were applying a voltage, V_{app}, to a standard resistor, R_{std} to make a current source we could write:

$$\frac{V_{\text{app}} - V}{R_{\text{std}}} = I_C \sin\phi + \dot{V}C$$

which simplifies to:

$$\frac{V_{\text{app}}}{R_{\text{std}}} = I_C \sin\phi + \frac{V}{R_{\text{std}}} + \dot{V}C$$

Note if we let $R = R_{\text{std}}$ and $I = \dfrac{V_{\text{app}}}{R_{\text{std}}}$ in this expression, we recover equation (3.24). Therefore, in a current biased experiment, R can either be the shunting normal resistance (≈ 1 kΩ for our experiments) or it may be the standard resistor used for the current source ($\approx 100\,$kΩ) or a combination of the two.

Using the Josephson voltage relationship, the current equation (3.24) can be rewritten as:

$$I = I_C \sin\phi + \frac{\hbar}{2e}\frac{\dot{\phi}}{R} + \frac{\hbar}{2e}C\ddot{\phi} \tag{3.25}$$

We can solve for $\ddot{\phi}$:

$$\frac{\hbar}{2e}C\ddot{\phi} = I - I_C \sin\phi - \frac{\hbar}{2e}\frac{\dot{\phi}}{R}$$

$$\ddot{\phi} = \frac{2e}{\hbar C}(I - I_C \sin\phi) - \frac{1}{RC}\dot{\phi}$$

We should note that this equation looks analogous to a particle moving in some potential with a damping term given by the resistance term. If we ignore the resistance damping term (i.e. set $R = \infty$ so there is no damping), we can determine the total energy, E, by integrating power, $P = IV$, over time:

$$\int IV dt = \int I\frac{\hbar}{2e}\frac{d\phi}{dt}dt = \frac{\hbar}{2e}\int I d\phi$$

which implies for equation (3.25)

$$\frac{\hbar}{2e}\int I d\phi = \frac{\hbar}{2e}\int I_C \sin\phi d\phi + \left(\frac{\hbar}{2e}\right)^2 C\int \ddot{\phi}\dot{\phi}dt$$

$$\frac{\hbar}{2e}I\phi + E = -\frac{\hbar}{2e}I_C\cos\phi + \left(\frac{\hbar}{2e}\right)^2 C\frac{1}{2}\dot{\phi}^2$$

The total energy E is constant so we introduce it as an integration constant on the left hand side thus yielding

$$E = \left(\frac{\hbar}{2e}\right)^2 C\frac{1}{2}\dot{\phi}^2 - \frac{\hbar}{2e}I\phi - \frac{\hbar}{2e}I_C\cos\phi \tag{3.26}$$

Equation (3.26) is exactly analogous to the total energy, E (which is constant), for a particle of mass $m = C\left(\frac{\hbar}{2e}\right)^2$ moving (in ϕ space) in the one dimensional tilted washboard

potential:

$$U(\phi) = -\frac{\hbar}{2e}\left(I_C \cos\phi + I\phi\right) \tag{3.27}$$

U is the Gibbs free energy of the system. Note that we could reverse this entire argument and say that given equation (3.27) we have the current phase relation specified by the Josephson equation (3.23). We can also recover the current phase relation (3.23) by differentiating equation (3.27) with respect to ϕ and setting this derivative equal to zero i.e. the superconducting state corresponds to sitting in the minimum of the potential U.

3.4.1 Free energy for nanowire

We can derive a similar free energy for a nanowire and derive a corresponding current phase relationship. In the one dimensional case, the Ginzburg Landau equation (3.7) reduces to:

$$f = f_{n0} + \alpha|\psi|^2 + \frac{\beta}{2}|\psi|^4 + |\psi|^2\frac{1}{2}2mv_S^2 + \frac{h^2}{8\pi} \tag{3.28}$$

We will neglect the $\dfrac{h^2}{8\pi}$ since our wires are thin. Because:

$$|\psi|^2 = -\frac{\alpha}{\beta}\left(1 - \frac{m^*v_S^2}{2|\alpha|}\right)$$

we have

$$f = -\alpha\frac{\alpha}{\beta}\left(1 - \frac{m^*v_S^2}{2|\alpha|}\right) + \frac{\beta}{2}\left(\frac{\alpha}{\beta}\left(1 - \frac{m^*v_S^2}{2|\alpha|}\right)\right)^2 - \frac{\alpha}{\beta}\left(1 - \frac{m^*v_S^2}{2|\alpha|}\right)\frac{1}{2}m^*v_S^2$$

$$f = \frac{\alpha^2}{\beta}\left(1 - \frac{m^*v_S^2}{2|\alpha|}\right)\left[-1 + \frac{1}{2}\left(1 - \frac{m^*v_S^2}{2|\alpha|}\right) - \frac{m^*v_S^2}{2\alpha}\right]$$

Note that because α is negative, $|\alpha| = -\alpha$ so we get:

$$f = -\frac{\alpha^2}{2\beta}\left(1 - \frac{m^*v_S^2}{2|\alpha|}\right)^2$$

Using the GL relation:

$$\frac{\alpha^2}{2\beta} = \frac{H_C^2}{8\pi}$$

We can write:

$$f = -\frac{H_C^2}{8\pi}\left(1 - \frac{m^*}{2|\alpha|}\frac{\hbar^2}{m^{*2}}\frac{\phi^2}{L^2}\right)^2$$

where we have used the relation for supercurrent velocity:

$$v_S = \frac{\hbar}{m^*}\nabla\phi = \frac{\hbar}{m^*}\frac{\phi}{L} \tag{3.29}$$

Using equation (3.14) we know:

$$f = -\frac{H_C^2}{8\pi}\left(1 - \frac{\xi^2\phi^2}{L^2}\right)^2$$

$$f = -\frac{H_C^2}{8\pi}\left(-2\frac{\xi^2\phi^2}{L^2} + \frac{\xi^4\phi^4}{L^4}\right)$$

$$f = \frac{H_C^2}{8\pi}4\frac{\xi}{L}\left(\frac{\xi\phi^2}{2L} - \frac{\xi^3\phi^4}{4L^3}\right)$$

This is a free energy density so $F = fV = fAL$

$$F = \frac{H_C^2}{8\pi}4\xi A\left(\frac{\xi\phi^2}{2L} - \frac{\xi^3\phi^4}{4L^3}\right)$$

We also know from equation (3.21) and reference [40] that:

$$\Delta F(0) = \frac{8\sqrt{2}}{3}\frac{H_C^2}{8\pi}A\xi = \sqrt{6}\frac{\hbar}{2e}I_C$$

so

$$F = \frac{3}{2\sqrt{2}}\sqrt{6}\frac{\hbar}{2e}I_C\left(\frac{\xi\phi^2}{2L} - \frac{\xi^3\phi^4}{4L^3}\right)$$

Combining with the energy associated with a phase slip $\frac{hI}{2e}\phi$ we get:

$$F = \frac{\hbar}{2e}\frac{3\sqrt{3}}{2}I_C\left(\frac{\xi}{2L}\phi^2 - \frac{\xi^3}{4L^3}\phi^4\right) - \frac{\hbar}{2e}I\phi \tag{3.30}$$

This expression corresponds to the tilted washboard U in equation (3.27). Since it is a Gibbs free energy we can differentiate it with respect to ϕ and set the derivative equal to zero to recover the the current phase relationship of a nanowire as written by Likharev [37]:

$$I_S = I_0\left[\frac{\xi\phi}{L} - \left(\frac{\xi\phi}{L}\right)^3\right] \tag{3.31}$$

where $I_0 = \frac{3\sqrt{3}}{2}I_C$ and I has been replaced by I_S, the supercurrent.

3.4.2 Derivation of the current phase relationship of a nanowire

Alternatively we can derive the current phase relationship of a nanowire, equation (3.31), directly from GL theory:

$$J_S = -2e\frac{\alpha}{\beta}\left(1 - \frac{m^* v_S^2}{2|\alpha|}\right)v_S$$

$$J_S = -2e\frac{\alpha}{\beta}\left(v_S - \frac{m^* v_S^3}{2|\alpha|}\right)$$

Using equation (3.29)

$$J_S = -2e\frac{\alpha}{\beta}\left(\frac{\hbar}{m^*}\frac{\phi}{L} - \frac{m^*}{2|\alpha|}\left(\frac{\hbar}{m^*}\frac{\phi}{L}\right)^3\right)$$

Using equation (3.14)

$$J_S = -2e\frac{\alpha}{\beta}\left(\sqrt{\frac{2|\alpha|}{m^*}}\frac{\phi\xi}{L} - \sqrt{\frac{2|\alpha|}{m^*}}\left(\frac{\phi\xi}{L}\right)^3\right)$$

$$J_S = -2e\frac{\alpha}{\beta}\sqrt{\frac{2|\alpha|}{m^*}}\left(\frac{\phi\xi}{L} - \left(\frac{\phi\xi}{L}\right)^3\right)$$

Now $J_C = -2e\frac{2\alpha}{3\beta}\sqrt{\frac{2|\alpha|}{3m^*}}$ so we have

$$J_S = \frac{3\sqrt{3}}{2}J_C\left(\frac{\phi\xi}{L} - \left(\frac{\phi\xi}{L}\right)^3\right)$$

which matches equation (3.31).

Note that for small values of ϕ the current phase relationship is roughly linear and we will occasionally use this linear form:

$$I_S = \frac{3\sqrt{3}}{2}J_C\frac{\phi\xi}{L} \tag{3.32}$$

For example, by combining this linear form with the Josephson voltage equation, we can write $V = \frac{\hbar}{2e}\frac{2}{3\sqrt{3}}\frac{L}{I_C\xi}\frac{dI}{dt}$ which implies the kinetic inductance of a nanowire is

$$L_k = \frac{\hbar L}{3\sqrt{3}eI_C\xi} \tag{3.33}$$

3.5 Cubic approximation of Gibbs free energy in the limit of high current

As I approaches I_C, the tilted washboard potential (3.27) can be accurately represented by a cubic polynomial. I will work this out in detail for a JJ first (which is a well known result) and then use the same technique for a nanowire. We would like to represent the Gibbs free energy (the tilted washboard potential) of a JJ (or a nanowire) with a cubic:

$$f(x) = s_3x^3 + s_2x^2 + s_1x + s_0$$

Since this is a potential energy, I can add a constant to it without changing anything so I will assume $f(0) = 0$ i.e. $s_0 = 0$. The natural point to expand around is the point between the local maximum and minimum where the second derivative changes sign i.e. $f''(0) = 0$ so $s_2 = 0$ and $x = \phi - \phi_0$ where ϕ_0 is the point in the original function where the second derivative is zero. Essentially we are translating by a distance ϕ_0 such that we can expand around $x = 0$. As ϕ goes to ∞, f should go to $-\infty$ and as ϕ goes to $-\infty$, f goes to ∞ so I will replace s_3 with $-s_3^2$. We want the derivative at $x = 0$ to be positive so I will replace s_1 with s_1^2. Thus our cubic function is now:

$$f(x) = -s_3^2 x^3 + s_1^2 x = -s_3^2 x \left(x - \frac{s_1}{s_3}\right)\left(x + \frac{s_1}{s_3}\right) \tag{3.34}$$

where $x = \phi - \phi_0$.

If f accurately represents the effective potential, we can now easily calculate the free energy barrier height by differentiating f, finding the two points where the first derivative is zero and then subtracting the two associated values of U. First, we find the stationary points:

$$\frac{df}{dx} = -3s_3^2 x^2 + s_1^2 = 0$$

$$x = \pm \frac{s_1}{\sqrt{3} s_3}$$

Plugging these stationary points into f yields:

$$\Delta U = -2s_3^2 \left(\frac{s_1}{\sqrt{3} s_3}\right)^3 + 2s_1^2 \frac{s_1}{\sqrt{3} s_3}$$

$$\Delta U = (-2s_3^2 + 6s_3^2)\left(\frac{s_1}{\sqrt{3} s_3}\right)^3$$

Thus the free energy barrier for the cubic is given by:

$$\Delta U = \frac{4s_1^3}{3\sqrt{3} s_3} \tag{3.35}$$

3.5.1 Derivation of cubic representation for Gibbs free energy of a Josephson junction in the limit of high current

For a Josephson Junction, the Gibbs free energy is given by(3.27): We will need three derivatives:

$$\frac{dU}{dx} = \frac{\hbar}{2e} I_C \sin\phi - I$$

$$\frac{d^2U}{dx^2} = \frac{\hbar}{2e} I_C \cos\phi$$

$$\frac{d^3U}{dx^3} = -\frac{\hbar}{2e} I_C \sin\phi$$

We find ϕ_0 by using the fact that the second derivative of U is zero at ϕ_0 i.e. :

$$\frac{d^2U}{dx^2}(\phi_0) = 0 = \frac{\hbar}{2e} I_C \cos\phi_0$$

This implies $\phi_0 = \frac{\pi}{2}$. We choose the positive root instead of the negative root because near the positive root the first derivative is positive.

Doing a Taylor expansion for U around $\frac{\pi}{2}$:

$$U = -\frac{\hbar}{2e} I \frac{\pi}{2} + \left(\phi - \frac{\pi}{2}\right)\left(\frac{\hbar}{2e} I_C - \frac{\hbar}{2e} I\right) + \frac{1}{6}\left(\phi - \frac{\pi}{2}\right)^3 \left(-\frac{\hbar}{2e} I_C\right)$$

Note by adding a constant $\frac{\hbar}{2e} I \frac{\pi}{2}$ to the potential U (which has no effect on energy differences) we have a cubic in the form of equation (3.34):

$$U = -\left(\frac{1}{6}\frac{\hbar}{2e} I_C\right)\left(\phi - \frac{\pi}{2}\right)^3 + \left(\frac{\hbar}{2e} I_C - \frac{\hbar}{2e} I\right)\left(\phi - \frac{\pi}{2}\right)$$

so $s_3^2 = \frac{1}{6}\frac{\hbar}{2e} I_C$, $s_1^2 = \frac{\hbar}{2e} I_C - \frac{\hbar}{2e} I$ and $x = \phi - \frac{\pi}{2}$

Plugging in to equation (3.35) for the free energy barrier of a cubic:

$$\Delta U = \frac{4}{3\sqrt{3}} \frac{\sqrt{6}\left(\frac{\hbar}{2e} I_C - \frac{\hbar}{2e} I\right)^{3/2}}{\left(\frac{\hbar}{2e} I_C\right)^{1/2}}$$

$$\Delta U = \frac{4\sqrt{2}}{3} \frac{\hbar I_C}{2e} \left(1 - \frac{I}{I_C}\right)^{3/2} \tag{3.36}$$

which is the well known result for a JJ [3, 22].

The frequency of small oscillations for a JJ can also be calculated exactly. It is fairly straightforward to see by looking at the potential energy of a simple harmonic oscillator $V = \frac{1}{2} m\omega^2 x^2$ that the frequency of small oscillations for an arbitrary function will be given by

$$\omega^2 = \frac{V''(x_0)}{m} \tag{3.37}$$

where x_0 is the local minimum of the function. By differentiating U for a JJ, it can easily be shown that the stationary points of the potential are:

$$\phi = \sin^{-1}\left(\frac{I}{I_C}\right)$$

Using equation (3.37) and a bit of trigonometry we get:

$$\omega^2 = \frac{1}{m} \frac{\hbar}{2e} I_C \frac{\sqrt{I_C^2 - I^2}}{I_C}$$

which simplifies to:

$$\omega = \sqrt{\frac{2eI_C}{\hbar C}} \left(1 - \frac{I^2}{I_C^2}\right)^{1/4} \tag{3.38}$$

Equation (3.38) is also a well known result [3, 22].

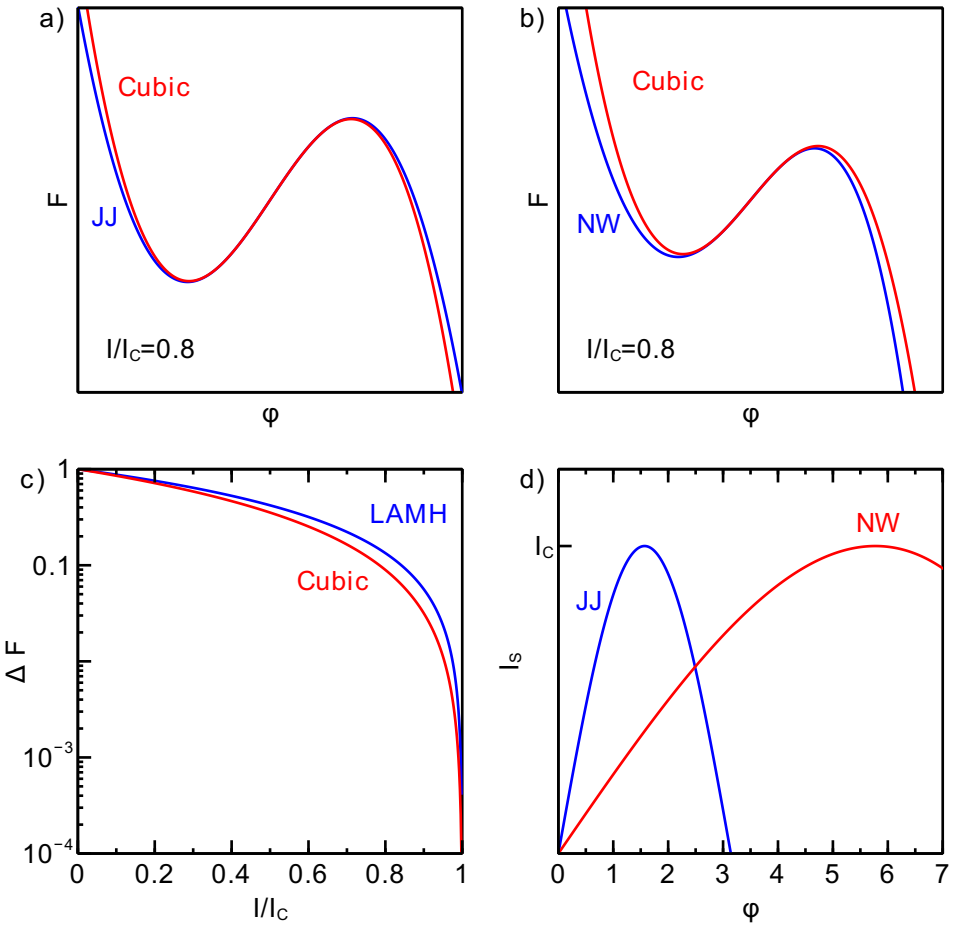

Figure 3.3: a) Cubic approximation of the JJ Gibbs free energy using the equations derived in the text for $I/I_C = 0.8$. b) Cubic approximation of the nanowire Gibbs free energy using the equations derived in the text for $I/I_C = 0.8$. c) Comparison of current dependence of the LAMH free energy with the GL free energy. The free energy axis is normalized to the LAMH free energy at zero current. Notice that for $I/I_C > 0.9$ they roughly agree. d) Comparison of the sinusoidal JJ current phase relation (valid for very short nanowires) with the Likharev current phase relation (valid for long nanowire). The multi-valued unstable branch of the Likharev current phase relation is not shown.

3.5.2 Derivation of cubic representation for the Gibbs free energy of a nanowire in the limit of high bias

We wish to show that the Gibbs free energy of a nanowire, equation (3.30) can be effectively represented by a cubic just like the Josephson Junction. If this is the case, all the MQT analysis for JJs (which is based on the fact that the effective potential looks like a cubic) can be applied to our nanowires. As before we need derivatives of U:

$$\frac{dU}{d\phi} = \frac{\hbar}{2e} I_0 \left(\frac{\xi}{L}\phi - \frac{\xi^3}{L^3}\phi^3 \right) - \frac{\hbar}{2e} I$$

$$\frac{d^2U}{d\phi^2} = \frac{\hbar}{2e} I_0 \left(\frac{\xi}{L} - \frac{3\xi^3}{L^3}\phi^2 \right)$$

$$\frac{d^3U}{d\phi^3} = -\frac{\hbar}{2e} I_0 \frac{6\xi^3}{L^3}\phi$$

To find ϕ_0 we again set the second derivative to zero at ϕ_0

$$0 = -\frac{\hbar}{2e} I_0 \left(\frac{\xi}{L} - \frac{3\xi^3}{L^3}\phi_0^2 \right)$$

$$\phi_0 = \pm \frac{L}{\sqrt{3}\xi}$$

We choose the positive root because we want the first derivative to be positive at $\phi = \phi_0$

$$U(\phi_0) = \frac{\hbar}{2e} I_0 \left(\frac{L}{6\xi} - \frac{L}{36\xi} \right) - \frac{\hbar}{2e} I \frac{L}{\sqrt{3}\xi}$$

$$U(\phi_0) = \frac{\hbar}{2e} I_0 \frac{5L}{36\xi} - \frac{\hbar}{2e} I \frac{L}{\sqrt{3}\xi} = \frac{\hbar}{2e} \frac{L}{\xi} \left(\frac{5I_0}{36} - \frac{I}{\sqrt{3}} \right)$$

so we shift the energy by this constant amount to make $U(\phi_0) = 0$

Expanding around ϕ_0:

$$U(\phi) = (\phi - \phi_0) \left(\frac{\hbar}{2e} I_0 \left(\frac{1}{\sqrt{3}} - \frac{1}{3\sqrt{3}} \right) - \frac{\hbar}{2e} I \right) + \frac{1}{6}(\phi - \phi_0)^3 \left(-\frac{\hbar}{2e} I_0 \frac{6\xi^2}{\sqrt{3}L^2} \right)$$

$$U(\phi) = \frac{\hbar}{2e}\left(\frac{2}{3\sqrt{3}}I_0 - I\right)(\phi - \phi_0) - \frac{\hbar}{2e}I_0\frac{\xi^2}{\sqrt{3}L^2}(\phi - \phi_0)^3$$

Comparing to our cubic function:

$$f(x) = -s_3^2 x^3 + s_1^2 x$$

we have $s_3^2 = \frac{\hbar}{2e}I_0\frac{\xi^2}{\sqrt{3}L^2}$, $s_1^2 = \frac{\hbar}{2e}I_0\frac{2}{3\sqrt{3}} - \frac{\hbar}{2e}I$ and $x = \phi - \frac{L}{\sqrt{3}\xi}$

Thus as before our free energy barrier is given by equation (3.35):

$$\Delta U = \frac{4}{3\sqrt{3}}\frac{\left(\frac{\hbar}{2e}I_0\frac{2}{3\sqrt{3}} - \frac{\hbar}{2e}I\right)^{3/2}}{\left(\frac{\hbar}{2e}I_0\frac{\xi^2}{\sqrt{3}L^2}\right)^{1/2}}$$

$$\Delta U = \frac{4}{3\sqrt{3}}\frac{\hbar}{2e}I_0\frac{2}{3\sqrt{3}}\frac{\left(\frac{\hbar}{2e}I_0\frac{2}{3\sqrt{3}}\right)^{1/2}}{\left(\frac{\hbar}{2e}I_0\frac{\xi^2}{\sqrt{3}L^2}\right)^{1/2}}\left(1 - \frac{I}{I_0\frac{2}{3\sqrt{3}}}\right)^{3/2}$$

$$\Delta U = \frac{4}{3\sqrt{3}}\frac{\hbar}{2e}I_0\frac{2}{3\sqrt{3}}\frac{L}{\xi}\sqrt{\frac{2}{3}}\left(1 - \frac{I}{I_0\frac{2}{3\sqrt{3}}}\right)^{3/2}$$

Notice that if we let $I_C = \frac{2}{3\sqrt{3}}I_0$ we recover an expression very similar to a Josephson Junction:

$$\Delta U = \frac{4}{3\sqrt{3}}\frac{L}{\xi}\sqrt{\frac{2}{3}}\frac{\hbar}{2e}I_C\left(1 - \frac{I}{I_C}\right)^{3/2} \tag{3.39}$$

with the difference being that the factor of $\frac{L}{\xi}\sqrt{\frac{2}{3}}$ has replaced a factor of $\sqrt{6} = 2.45$ Like the JJ case this cubic approximation is only valid near I_C. If you plug in $I = 0$ to the JJ expression you do not get the correct zero current free energy barrier. This approach is only valid if the switching current gets close enough to the critical current for the cubic approximation to be accurate. It should be noted that equation (3.39) differs from the result

from LA theory because they are derived under different assumptions. Tinkham [41] showed that the expression (3.22) accurately describes the result of LA theory [33]. However as shown in figure 3.3 for high enough currents the two theories agree.

3.6 Escape rates and switching current probability distributions

Now that we know the free energy barrier, we can consider further consequences of the escape rate. In particular, it is advantageous to relate escape rates and switching probability distributions (which we can measure). If we consider a particular value of I, Γ is just a constant. The persistence probability as a function of time is governed by an equation:

$$dW(t) = -\Gamma W(t)dt$$

This is equivalent to saying the number of particles that escape in a unit of time, dt, is the escape rate times that unit of time. By dividing by the total number of particles we get a probability distributions rather than the number of particles. I am using W to represent the persistence probability following the notation of Garg [46]. Writing this as a differential equation we have:

$$\frac{dW}{dt} = -\Gamma W(t)$$

The solution to this equation is:

$$W(t) = \exp(-\Gamma t)$$

This was for a stable value of current. Suppose now the current is slowly ramped up at a constant speed speed $\dot{I}$ starting from $I = 0$ such that $I = \dot{I}t$. (in actual practice the ramp does not have to be constant just sufficiently slow that the first derivative is not changing

dramatically. Then:

$$dW = -\Gamma(I(t))W(t)dt$$

$$\frac{dW}{W} = -\Gamma(I(t))dt$$

$$\ln W = -\int_0^t \Gamma(I(t'))dt'$$

$$W(t) = \exp\left(-\int_0^t \Gamma(I(t'))dt'\right)$$

We can change variable of integration from t' to I by using $I = \dot{I}t$ and $dI = \dot{I}dt$

$$W(I) = \exp\left(-\int_0^I \frac{\Gamma(I)}{\dot{I}}dI\right) \tag{3.40}$$

Note this is not the escape probability but the probability that the particle will persist up to current I.

To get the escape probability we note that the particle must be either escaped or not escaped i.e.:

$$\int_0^I P(I)dI + W(I) = 1$$

Differentiating this expression for I we have:

$$P(I) + \frac{dW}{dI} = 0$$

or

$$P(I) = -\frac{dW}{dI} = \frac{\Gamma(I)}{\dot{I}}\exp\left(-\int_0^I \frac{\Gamma(I)}{\dot{I}}dI\right) \tag{3.41}$$

This expression is the essential connection between escape rates and switching current distributions [46]. To compare to experiments it can be approximated by

$$P(I) \approx \frac{\Gamma(I)}{\dot{I}}\exp\left(-\frac{\Delta I}{\dot{I}}\sum_0^I \Gamma(I)\right) \tag{3.42}$$

where $\dot{I}$ is the sweep speed and ΔI is a small enough step (typically the bin size of the switching current distribution). The escape rates $\Gamma(I)$ is typically the model one wishes to compare with the data such as those for thermal and quantum phase slips given by equations (3.2) and (3.3) respectively. Alternatively, we could write this as:

$$P(I) = \frac{\Gamma(I)}{\dot{I}} W$$

Which is:

$$P(I) = \frac{\Gamma(I)}{\dot{I}} \left(1 - \int_0^I P(u)du\right)$$

which is the expression used by Fulton and Dunkelberger [47].

If we divide the current into bins (as for a histogram), we can express the rate of bin K as an approximate function of the probability distribution. We will assume the rate is constant in the bin and that the bin is small enough that $\Delta I = \dot{I}\Delta t$. We take $K = 1$ to correspond to the bin with maximum switching current thus $t = 0$ corresponds to bin K and $t = \Delta t$ corresponds to bin $K - 1$:

$$W = \exp(-\Gamma(K)\Delta t) = 1 - \int_{I(K)}^{I(K-1)} P(I)dI$$

Note that $\int_0^\infty P(u)du = 1 = \int_0^I P(u)du + \int_I^\infty P(u)du$ implies

$$\exp(-\Gamma(K)\Delta t) = \int_{I(K-1)}^{\infty} P(I)dI \Bigg/ \int_{I(K)}^{\infty} P(I)dI$$

Dividing by the second integral (which is ideally equal to one) removes the need for $P(I)$ to be normalized. Taking the logarithm and simplifying:

$$\Gamma(K)\Delta t = \ln\left(\int_{I(K)}^{\infty} P(I)dI \Bigg/ \int_{I(K-1)}^{\infty} P(I)dI\right)$$

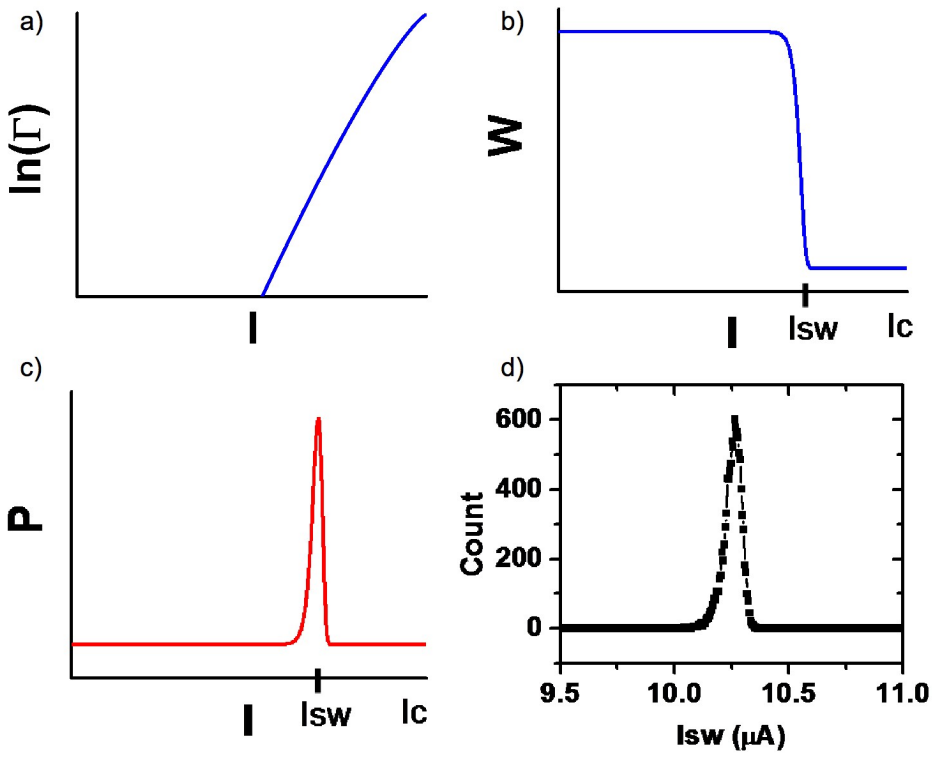

Figure 3.4: Connection between escape rates and distributions a) The escape rate, Γ, as given by equation 3.4. Note that as I approaches the mean switching current, Γ grows exponentially. b) The persistence probability, W, calculated from the escape rate in a as given by equation 3.40. Notice as I approaches the mean switching current, the persistence probability quickly drops from 1 to 0. c) The switching probability density as given by equation 3.41. The distribution is centered around the mean switching current. d) An actual measured switching current distribution which can be compared to theoretical distributions such as the one in c.

Replacing the integrals by sums yields:

$$\Gamma(K) = \dot{I}\frac{1}{\Delta I}\ln\left(\sum_{j=1}^{K} P(j) \Big/ \sum_{i=1}^{K-1} P(i)\right) \tag{3.43}$$

where $K = 1$ corresponds to the bin with the highest switching current. Equation (3.43) is the expression necessary to convert experimental switching current distributions into rates [47].

3.6.1 Mean and standard deviation of switching current probability distribution

Now in principle, given any rate, the switching current probability distribution is entirely known and properties of the distribution such as the mean switching current and standard deviation are straightforward to calculate. In practice, this is a somewhat involved calculation for a generic rate as shown by Garg [46]. We use the generic rate:

$$\Gamma = A\epsilon^{a+b-1}\exp(-B\epsilon^b) \tag{3.44}$$

where $\epsilon = 1 - I/I_C$. The mean and standard deviation to lowest order are [46]:

$$\langle\epsilon\rangle = \left(\frac{\ln X}{B}\right)^{1/b}$$

$$\sigma_\epsilon^2 = \frac{\pi^2}{6b^2}\left(\frac{(\ln X)^{-2+2/b}}{B^{2/b}}\right)$$

where $X = \dfrac{I_C}{\dot{I}}\dfrac{A}{bB^{1+a/b}}$

This implies the mean switching current is:

$$\langle I_{SW}\rangle = I_C\left[1 - \left(\frac{\ln X}{B}\right)^{1/b}\right] \tag{3.45}$$

and the standard deviation of the switching current, σ, is

$$\sigma = I_C\frac{\pi}{\sqrt{6}b\ln X}\left(\frac{\ln X}{B}\right)^{1/b} \tag{3.46}$$

Note we can relate standard deviation, mean switching current and critical current

$$\langle I_{SW}\rangle = I_C\left[1 - \sigma\frac{\sqrt{6}b\ln X}{I_C\pi}\right]$$

or

$$I_C = \langle I_{SW} \rangle + \sigma \frac{\sqrt{6} b \ln X}{\pi} \tag{3.47}$$

Equation (3.46) implies

$$\frac{1}{B} = \frac{kT_{esc}}{U_C} = \frac{1}{\ln X} \left(\frac{\sqrt{6} b \sigma \ln X}{I_C \pi} \right)^b \tag{3.48}$$

where $U_C = \sqrt{6}\hbar I_C/2e$. Equations (3.45) and (3.46) allow us to fit mean and standard deviation for a set of distributions while equations (3.47) and (3.48) enable us to estimate the parameters I_C and T_{esc} from a single distribution.

We can compare this expression with more standard forms for these quantities by noting that we are assuming constant sweep speed from zero so that $I = \dot{I}t$ i.e. $\Delta I = \dot{I}\Delta t$ (the best approximation for ΔI is σ). Note also that $\pi/\sqrt{6} = 1.28$ and that b is typically on the order of or slightly larger than 1 i.e. the term $\pi/\sqrt{6}b$ is quite close to one. Finally, the prefactor A is the characteristic frequency $\omega_p/2\pi$

In addition, if we assume $b \approx 1$ and $a \approx 0$ (a actually equals zero for a highly damped JJ) we get: $\dfrac{\sigma}{I_C} \approx \left(\dfrac{1}{B}\right)$ implying that

$$\Delta I \approx \sigma \approx I_C/B \tag{3.49}$$

For these same assumptions we also get

$$X = \frac{I_C}{B\dot{I}} A = \frac{\sigma}{\dot{I}} \frac{\omega_p}{2\pi} = \frac{\Delta I}{\dot{I}} \frac{\omega_p}{2\pi} = \frac{\omega_p}{2\pi} \Delta t \tag{3.50}$$

Thus assuming $b = 1$ inside the logarithm and that $\dfrac{\pi}{\sqrt{6}b} \approx 1$ we recover:

$$\sigma = \frac{I_C - \langle I_{SW} \rangle}{\ln(\omega_p \Delta t/2\pi)} \tag{3.51}$$

which is a well known expression [3]. For thermal activation, where $B = U_C/k_B T$, we can

write another well known expression for the mean switching current [3, 41]:

$$\langle I_{SW} \rangle = I_C - I_C \left(\frac{k_B T_{esc}}{U_C} \ln(\omega_p \Delta t / 2\pi) \right)^{1/b} \tag{3.52}$$

Together these equations imply:

$$\sigma = \frac{\left(\frac{k_B T_{esc}}{\sqrt{6}\hbar} \ln(\omega_p \Delta t / 2\pi) \right)^{1/b}}{\ln(\omega_p \Delta t / 2\pi)}$$

which yields the simple relation

$$\sigma \propto T_{esc}^{1/b} \tag{3.53}$$

Note that equation (3.53) immediately implies for thermal escape that:

$$\sigma \propto T^{2/3} \text{ for a cubic barrier or } \sigma \propto T^{4/5} \text{ for an LAMH barrier.}$$

Likewise, assuming a constant critical current, equation (3.53) implies for quantum escape that:

$$\sigma \text{ is constant vs } T$$

For thermal escape from a cubic (e.g. JJ) potential, theory predicts $b = 3/2$ regardless of damping. For quantum escape, theory predicts $b = 5/4$ (no damping) or $b = 1$ (high damping) [46]. Nanowires are expected to be highly damped with the hysteresis caused by Joule heating [41].

3.6.2 Sweep speed of a sine wave

The sweep speed, $\dot{I}$, appears in the expressions for mean switching current, equation (3.45), and standard deviation, (3.46) in the term $\ln X$. For a sine wave, the sweep speed is slightly

varying as the current is swept. We wish to figure out the sweep speed of the expression:

$$I(t) = I_A \sin(2\pi f t) \tag{3.54}$$

where I_A is the amplitude of the sinusoidal input current (typically $\approx 10\,\mu$A) and f is the frequency (typically $\approx 11\,$Hz). Taking a derivative with respect to time yields:

$$\dot{I} = I_A 2\pi f \cos(2\pi f t) \tag{3.55}$$

Using the trigonometry relation $\cos\theta = \sqrt{1-\sin^2\theta}$ we have $\dot{I} = 2\pi f I_A \sqrt{1-\sin(2\pi f t)}$. Using equation (3.54), we can write the sweep speed as:

$$\dot{I} = 2\pi f I_A \sqrt{1-\left(\frac{I}{I_A}\right)^2} \tag{3.56}$$

Notice that using equation (3.56), we can for any switching current (given the frequency and amplitude of the input current signal) determine the sweep speed.

3.7 Damping and condition for observing MQT

The basic condition for observation of MQT is that the quantum contribution, equation (3.3) dominates over the thermal contribution, equation (3.2). This is equivalent to requiring

$$kT < \hbar\omega_p/2\pi \tag{3.57}$$

For our nanowires, kinetic inductance is on the order of 1 nH (see equation 3.33) and capacitance is on the order of 1 fF [10] so using $\omega_p = 1/\sqrt{LC} \approx 10^{12}\,$Hz (i.e. $f \approx 100\,$GHz) we can estimate that quantum contributions will become important around $T \approx 1\,$K. For JJ, the plasma frequency is typically made a factor of 10 lower allowing quantum effects only to

be seen below 0.1 K though there are other advantages in doing so. Alternatively one could use the reciprocal of the Ginzburg Landau time ($\approx 10^{12} s^{-1}$ multiplied by L/ξ) which would yield an even higher frequency [34, 41]. Damping can also effect MQT. As mentioned above, nanowires are expected to be heavily damped [41]. For heavy damping, the new condition is that $kT < \hbar\omega_p^2 RC/3\pi$ [3, 46]. For typical wires, R is on the order of 1000 Ω and we again get the condition that quantum contributions will become important around $T \approx 1$. Note that there is a high level of uncertainty in these estimates since several parameters could vary as much as an order of magnitude. For example, it might be more appropriate to replace R by the impedance of free space which is on the order of 100 Ω.

It is worth noting that for a Josephson junction: $\omega_p = (2eI_{C0}/\hbar C)^{1/2}$. Thus $\omega_p^2 RC = 2eI_{C0}R/\hbar$. Thus for a heavily damped junction changing the capacitance would not change T_q (which is proportional to ω_p) but changing R would. For a heavily damped JJ (or any other process whose escape is from a cubic potential), the parameters in equation (3.44) are known for both thermal and quantum escape and are listed in table 3.7 ($\gamma = 1/RC$) [46, 48]. For comparison, I have listed the escape rates for nanowires derived from LAMH theory [23, 49] in table 3.7. I have made the assignments $1/\tau_{GL} = \omega_p$ and $U_C = \sqrt{6}\hbar I_C/2e$ to allow a more direct comparison.

Escape	Theory	A	B	a	b
Thermal	JJ	$\omega_p^2/2\pi\gamma$	U_C/kT	0	3/2
Quantum	JJ	$\left(3U_C\gamma^7/\hbar\omega_0^6\right)^1/2$	$3\pi\gamma U_C/\hbar\omega^2$	0	1
Thermal	NW	$(\omega_p/2\pi)(L/\xi(T))(U_C/kT)^{1/2}$	U_C/kT	3/8	5/4
Quantum	NW	$(\omega_p/2\pi)(L/\xi(T))(U_C/kT_q)^{1/2}$	U_C/kT_q	3/8	5/4

3.8 Naive WKB theory approach to decay

This is a rough, slightly inaccurate, derivation of quantum decay using naive WKB theory just to get a feel for the more complicated expressions for quantum escape e.g. with damping.

From WKB theory we have the transmission probability:

$$T = \exp\left[-\frac{2}{\hbar}\int_{q_0}^{q_1}\sqrt{2m(V(q)-E)}dq\right]$$

where the integral is over the classically unallowed part of the barrier.

Quasi-classically, the particle would have a chance to escape with some characteristic frequency $\Omega/2\pi$ so we can calculate the rate, Γ:

$$\Gamma = \frac{\Omega}{2\pi}T$$

or substituting in the WKB value:

$$\Gamma = \frac{\Omega}{2\pi}\exp\left[-\frac{2}{\hbar}\int_{q_0}^{q_1}\sqrt{2m(V(q)-E)}dq\right]$$

Note that Γ is just some number that depends on the shape of the potential. The shape of the potential is entirely dependent on the current I. Therefore looking at the form of T it is not surprising that Γ will always be given by a form of a characteristic frequency times an exponential dependent on the shape of the potential.

For the virtual ground state: $E = \frac{1}{2}\hbar\omega_0$ and assuming the potential is given by the generic cubic in equation (3.34), the integral we need to do is some what nasty:

$$T = \exp\left[-\frac{2}{\hbar}\int_{q_0}^{q_1}\sqrt{2m(-s_3^2q^3+s_1^2q-E)}dq\right]$$

To simplify things I am going to approximate the hump of the cubic we are integrating over with a quadratic: $g = -s^2q^2$. To do a Taylor expansion I need the derivatives of f:

$$f = -s_3^2x^3 + s_1^2x$$

$$\frac{df}{dx} = -s_3^2 3x^2 + s_1^2$$

$$\frac{d^2 f}{dx} = -s_3^2 6x$$

Expand around the stationary point $x = \frac{s_1}{\sqrt{3}s_3}$

$$f = -\frac{s_1^3}{3\sqrt{3}} + \frac{s_1^3}{\sqrt{3}s_3} - \left(x - \frac{s_1}{\sqrt{3}s_3}\right)^2 \frac{6s_1 s_3^2}{2\sqrt{3}s_3}$$

$$f = \frac{2s_1^3}{\sqrt{3}s_3} - \left(x - \frac{s_1}{\sqrt{3}s_3}\right)^2 \frac{3s_1 s_3}{\sqrt{3}}$$

which we can write as $g = -s^2 q^2$ where $s^2 = \frac{3s_1 s_3}{\sqrt{3}}$ and $q = x - \frac{s_1}{\sqrt{3}s_3}$ I have shifted the potential energy so that $g(0) = 0$ which is just adding a constant to potential energy.

Limits of integration: Find roots of $g(q) = -(\Delta U - E)$

$$g(q) = -s^2 q^2 = E - \Delta U$$

$$q = \pm \frac{1}{s}\sqrt{\Delta U - E}$$

$$T = \exp[-\frac{2}{\hbar}\int_{q_0}^{q_1} \sqrt{2m(-s^2 q^2 - (-\Delta U + E))}dq]$$

$$T = \exp[-\frac{2}{\hbar}\int_{q_0}^{q_1} \sqrt{2m(\Delta U - E - s^2 q^2)}dq]$$

Let $\delta^2 = \Delta U - E$

$$T = \exp[-\frac{2}{\hbar}\int_{q_0}^{q_1} \delta\sqrt{2m(1 - \frac{s^2}{\delta^2}q^2)}dq]$$

Let $\frac{s}{\delta}q = \sin\theta$ then $\frac{s}{\delta}dq = \cos\theta d\theta$

Limits of integration: $\sin\theta = \pm\frac{1}{\delta}\sqrt{\Delta U - E} = \pm 1$ so $\theta = \pm\frac{\pi}{2}$

$$T = \exp[-\frac{2}{\hbar}\int_{-\pi/2}^{\pi/2} \delta\sqrt{2m(1 - \sin^2\theta)}\frac{\delta}{s}\cos\theta d\theta]$$

$$T = \exp[-\frac{2}{\hbar}\int_{-\pi/2}^{\pi/2} D\sqrt{2m}\frac{\delta}{s}\cos^2\theta d\theta]$$

$$T = \exp[-\frac{2}{\hbar}\int_{-\pi/2}^{\pi/2} \sqrt{2m}\frac{\delta^2}{2s}(1-\cos 2\theta)d\theta]$$

$$T = \exp[-\frac{2}{\hbar}\sqrt{2m}\frac{\delta^2}{2s}(\theta - \frac{1}{2}\sin 2\theta)]|_{\theta=-\pi/2}^{\theta=\pi/2}$$

$$T = \exp[-\frac{2}{\hbar}\sqrt{2m}\frac{\delta^2}{2s}\pi]$$

$$T = \exp[-\frac{2\pi}{\hbar}\sqrt{2m}\frac{\Delta U - E}{\sqrt{2m}\omega}]$$

I am neglecting E compared to the much larger ΔU

$$T = \exp\left[-2\pi\frac{\Delta U}{\hbar\omega}\right]$$

So from this fairly simple and slightly wrong calculation we get:

$$\Gamma \approx \frac{\Omega}{2\pi}\exp\left[-2\pi\frac{\Delta U}{\hbar\omega}\right]$$

Compare the more accurate expression (with zero damping) [22]:

$$\Gamma = \frac{\Omega}{2\pi}\exp[-\frac{36}{5}\frac{\Delta U}{\hbar\omega}]$$

Besides a tiny numerical difference of order unity between: $2\pi \approx 6.28$ and $\frac{36}{5} = 7.2$ the expressions are the same. This numerical difference arises both because I am doing naive WKB and because I approximated a cubic with a quadratic to make the math easier.

Chapter 4

High bias voltage pulses effects on superconducting nanowires

We present a method for in-situ tuning the critical current (or switching current) and critical temperature of a superconducting nanowire using high bias voltage pulses. Our main finding is that as the pulse voltage is increased, the nanowires demonstrate a reduction, a minimum and then an enhancement of the switching current and critical temperature. Using controlled pulsing, the switching current of a superconducting nanowire can be set exactly to a desired value to within 10 nA. Normal resistance is at first unchanged and then reduces as switching current increases. These results correlate with in-situ transmission electron microscope imaging where an initially amorphous molybdenum germanium ($Mo_{76}Ge_{24}$) nanowire becomes polycrystalline and then transforms into a single crystal Mo_3Ge nanowire. We compare our transport measurements to thermally activated and quantum tunneling models of Little's phase slips in nanowires.

4.1 Introduction

Superconducting nanowires have been proposed as candidates for various solid state qubit implementations [25–27]. However, a crucial step towards certain implementations of nanowire qubits is exact control over the critical current of a nanowire which is difficult to achieve by controlling fabrication parameters alone. We describe here a post-fabrication technique using high bias voltage pulses that allows precise in-situ control over the critical current which may be very important in developing superconducting nanowire qubits.

We have performed experiments applying controlled high bias pulses to superconducting

MoGe nanowires in situ and have observed a decrease of switching current, I_{SW}, for a given temperature with a corresponding decrease in critical temperature, T_C. Initially, the wire maintains overall behavior consistent with being a homogeneous nanowire with a reduced switching current and critical temperature but no significant change in the normal resistance. As larger and larger pulses are applied, the switching current reaches a minimum and then starts to increase, returning to values similar to or exceeding the starting switching current. Critical temperature also returns and normal resistance is observed to drop. Using scanning electron microscope (SEM) and transmission electron microscope (TEM) analysis, we find that this is a permanent morphological change of the nanowire and not weak link formation. An interesting and useful application of this effect is to control the switching current of a superconducting nanowire, in-situ, opening the possibility to engineer nanowires with precise switching currents (and to a lesser extent critical temperatures). We demonstrate that the switching current can be set to within approximately 10 nA of a desired value (see figure 4.1). The switching current cannot be more accurately defined as its natural stochastic behavior results in a distribution with a standard deviation of the order of 10 nA [23].

4.2 Experiment

The nanowires were fabricated using the method of molecular templating [20]. Briefly, fluorinated single wall carbon nanotubes (SWNTs) are suspended across a trench in a Si substrate coated with SiO_2 and SiN films. $Mo_{76}Ge_{24}$ is deposited by DC sputtering forming a nanowire by using the nanotube as a nanoscaffold. Pattern definition by photolithography and the undercut of the trench allow only one conductance path, the nanowire, to be formed. The superconducting properties of the nanowires were measured in a He-4 (base temperature 1.5 K) or He-3 system (base temperature 0.3 K). The nanowires were measured in a standard current biased set-up with a low noise voltage source feeding a large value standard resistor R_{std} serving as a current source and separate voltage probes. The four-probe measurement

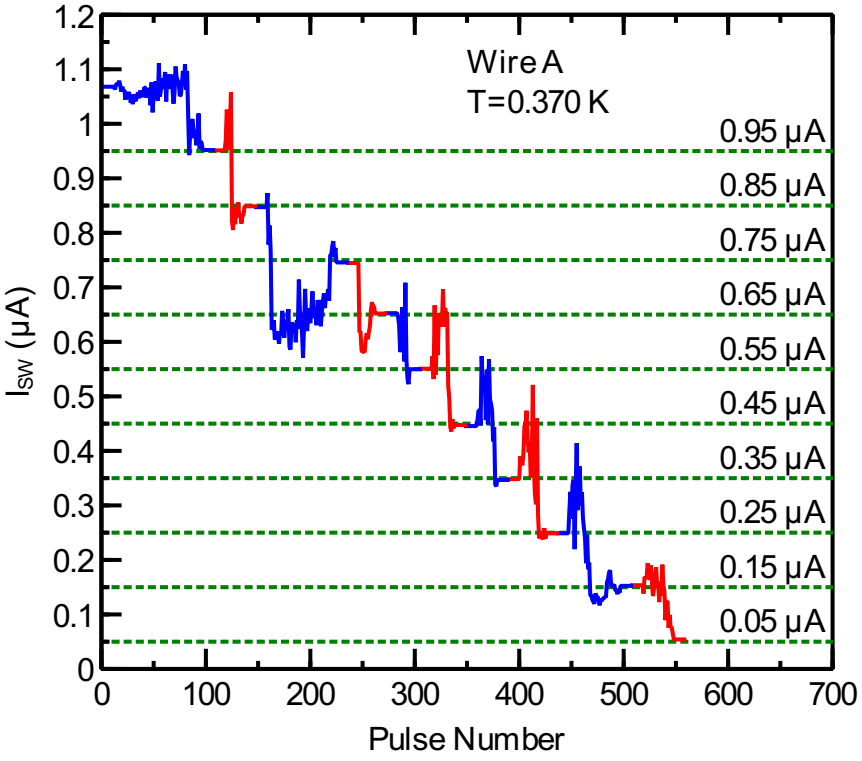

Figure 4.1: Setting I_{SW} exactly using voltage pulses. The switching current can be set exactly using a combination of large and small pulses. The last unpulsed switching current value is extended after each session of pulsing to indicate the set value. The flat regions correspond to the set value of switching current where no pulsing is applied. The noisy regions corresponds to the switching current being set to the desired value as pulsing is applied (pulses are always applied between switching current measurements). In this example, the starting switching current was 1.07μA and the chosen target values (shown by green dotted lines) were: 0.95μA, 0.85μA, 0.75μA, 0.65μA, 0.55μA, 0.45μA, 0.35μA, 0.25μA, 0.15μA and 0.05μA. In each of these 10 examples, the target value was achieved.

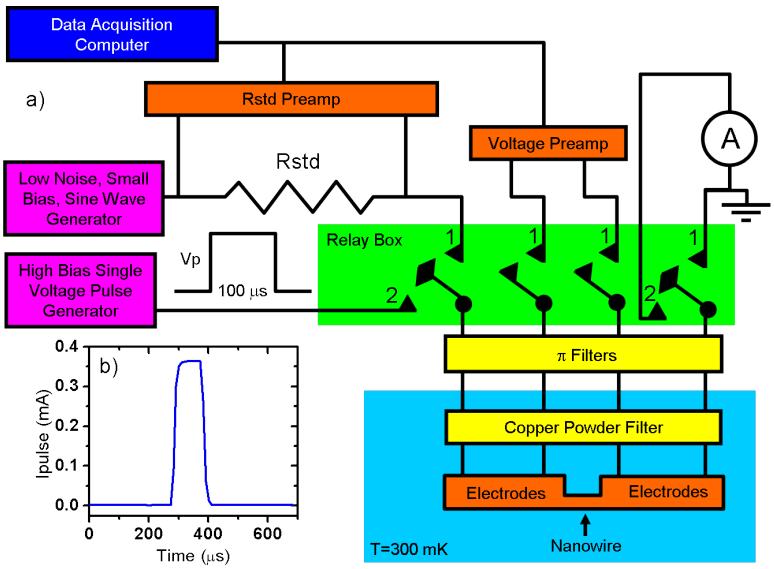

Figure 4.2: Experiment Set-up: a) 4 relays (voltage controlled switches) are used to switch between measurement and pulsing mode. In measurement mode (all relays in position 1), we can measure either voltage vs current curves (amplitude of current ≈1-10 μA) or resistance vs temperature curves (amplitude of current ≈10-20 nA). A sine wave generator connected through R_{std} = 0.1-1 MΩ forms a current source connected to the left lead. A small voltage (≈1-10 mV) is measured on the two center leads. The right current lead is grounded. In pulsing mode (relays in position 2), a single high bias voltage pulse (≈0.1-1 V) is sent in on the left current lead, the two center leads are disconnected and the pulse can be detected on the right lead using an ammeter (≈0.1-1 mA). b) Example measured current going through nanowire from a high bias voltage pulse measured with the ammeter. The pulse is 100 μs long and there are minor amounts of rounding of the pulse due to filtering in the cryostat.

is of the superconducting electrodes and not the nanowire itself but the superconducting electrodes are seamlessly connected to the nanowire so we label it a quasi-four probe measurement. In order to protect sensitive measurement equipment from high bias pulses (1 V or more), a switching system was employed to switch between measurement mode and pulsing mode (see Figure 4.2a). The wire was pulsed between sensitive measurements in order to change its morphology.

Both manually operated switches and automated relays (voltage powered switches controlled by a computer) were used. No difference in behavior of the nanowires was observed between the two. The relays were low bias, latching relays powered by a Keithley electrometer controlled by the measurement computer through GPIB. The latching design of the

relays allows the power to the relays to be removed without affecting the switch position of the relays. To test the relays, repeated switches were made with no pulse application. No effect on any nanowire was observed from just switching back and forth without pulse application. Square pulses were applied using a data acquisition (DAQ) card. Pulse duration was kept at 100 μs and pulse voltage amplitude was varied. Pulses of this length transmit fairly well through the filtering system on the cryogenic measurement systems maintaining their square shape with minimal rounding (see Fig. 4.2b). We have not systematically explored the effect of different length pulses (or different shaped pulses) but we do not expect significant dependence on these two factors for the following reasons. The response time of the nanowire should be on the order of picoseconds (the capacitance of the electrodes is on the order of a few fF [10] while the resistance is approximately 1 kΩ giving a RC time constant of approximately 1-10 picoseconds) so the wire will have reached equilibrium current early in the pulse. The wire is expected to reach its maximum temperature (due to Joule heating) during the pulse and cool back to base temperature after the pulse within 10-100 ns [23] so it should be well thermally equilibrated early in the pulse as well. It should be noted that our relay switching speed (approximately 1 second) is not fast enough to allow us to capture the cooldown back to base temperature after the pulse and the wire is well thermalized before switching currents are measured after a pulse.

In measurement mode, a low bias sine wave signal current source is applied to the nanowire and voltage is measured separately using the quasi-four probe measurement described previously (see figure 4.2a). Typical voltage versus current (VI) curves and the effects of pulsing on them are shown in figure 4.3. I_{SW} initially decreases with minimal change in R_N and I_R and the VI curves maintain single hysteretic loops characteristic of homogeneous wires. The hysteresis in the VI curve disappears as the switching current goes to a minimum (see figure 4.3d). A flat, superconducting region indicates a non-zero critical current always remains. Higher pulsing results in a return of the hysteretic VI curve with now increasing I_{SW} and decreasing R_N as pulse voltage is increased. When I_{SW} returns, we generally

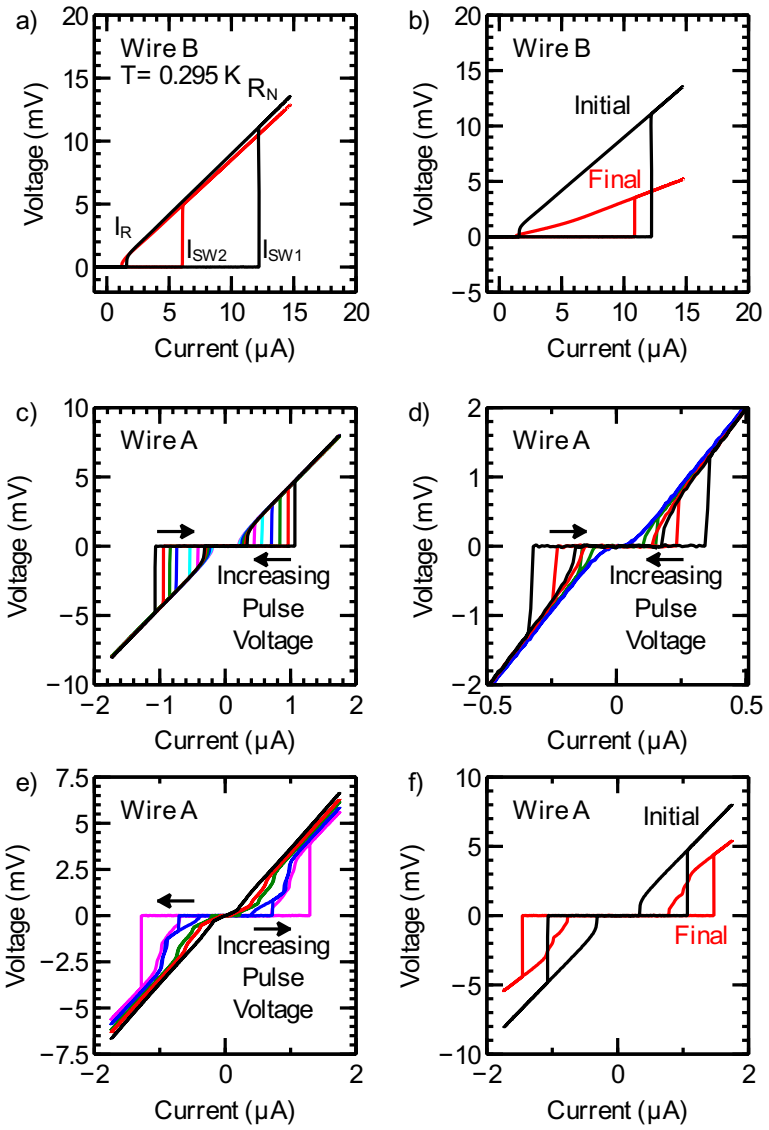

Figure 4.3: Voltage vs current (VI) curves demonstrating effect of high bias pulses. a) Initial application of high bias pulses decreases the switching current from I_{SW1} to I_{SW2} while minimally changing R_N and I_R. b) Further pulsing results in the return of I_{SW} and a drop in R_N. 'Initial' is the same curve as the one shown in black in graph a. 'Final' is the last VI curve before the sample broke. c) A different nanowire with a smaller initial I_{SW}. This graph shows many VI curves to indicate the gradual decrease of the I_{SW} as increasing pulses are applied d) Application of higher pulses results in a loss of hysteresis of the VI curve. However, the VI curve retains a flat, superconducting region with apparently non-zero critical current e) Still higher pulses results in the return of I_{SW} with a drop in R_N and evidence of phase slip centers. f) Still higher pulsing produces an almost uniform VI curve with I_{SW} exceeding the original switching current and a further drop in R_N. 'Initial' is the same curve as the one shown in black in graph c. 'Final' is the last VI curve before the sample broke.

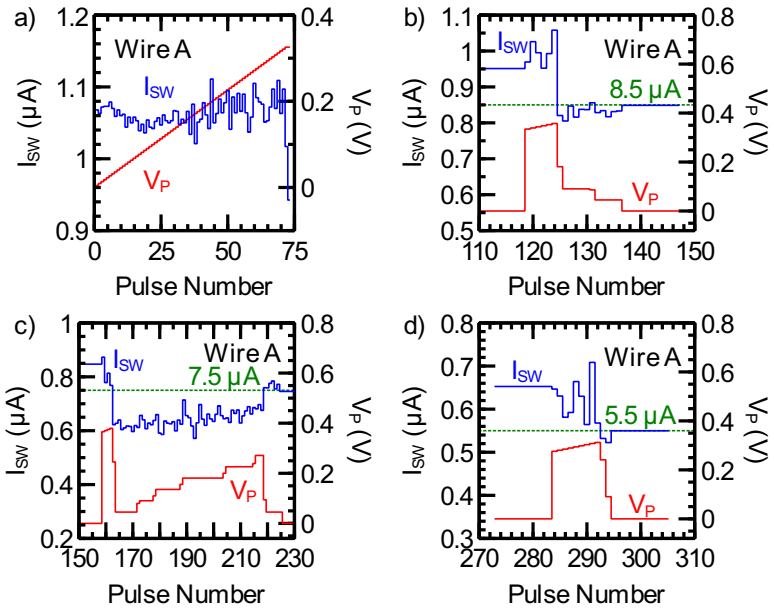

Figure 4.4: Effect on I_{SW} of large and small voltage pulses. a) Close up on effect of pulsing on nanowire's switching current as pulse voltage is increased from 0 to 0.326V. As pulse voltage grows, the nanowire's switching current becomes increasingly stochastic until at large enough pulses we observe a strong downward trend. In this case, the drop in switching current occurs at pulse number 73 for pulse amplitude 0.326V. This combination of downward trend and stochasticity can be used to set the switching current exactly to any value below it's starting switching current. b) Setting of I_{SW} to 0.85μA in figure 4.1 with accompanying voltage pulses. At first large pulses are applied to get the switching current near the desired value. Then smaller pulses are applied to bounce the switching current to the exact value desired (0.85μA shown by the dotted green line). c) Setting of I_{SW} to 0.75 μA in figure 4.1 with accompanying voltage pulses. In this example, the initial larger pulses dropped I_{SW} significantly below the desired value. The smaller pulses applied after the initial large pulses were chosen small enough to avoid significant further decrease of the switching current but large enough to produce enhanced stochasticity allowing a return up to the desired value (0.75μA shown by the green dotted line). d) Setting of I_{SW} to 0.55 μA in figure 4.1 with accompanying voltage pulses. In this example, the initial larger pulses primarily enhanced the stochasticity of I_{SW} allowing a value close to the desired value to be achieved. The final smaller pulses bounced I_{SW} to the exact desired value of 0.55μA shown by the green dotted line). In each of these cases, as the desired value of I_{SW} is reached, the pulsing is reduced to zero and so the wire remains at that value indefinitely.

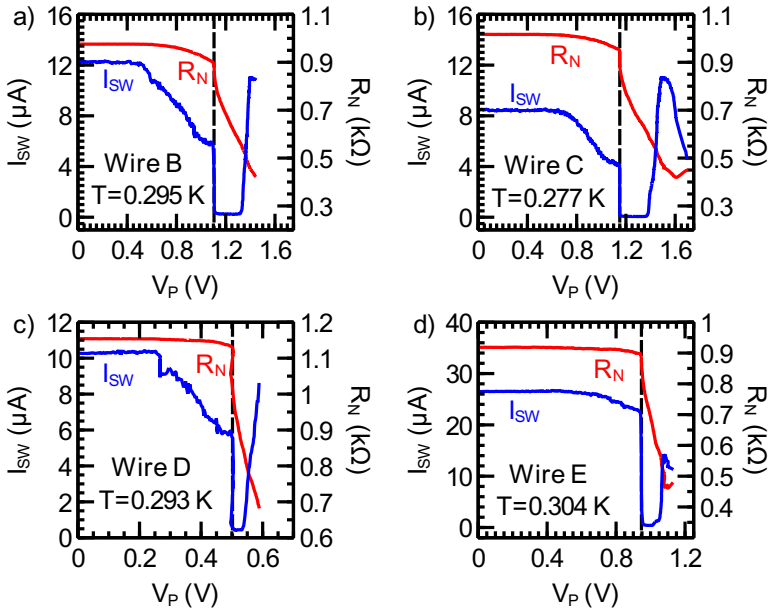

Figure 4.5: Switching current, I_{SW}, and normal resistance, R_N, vs the maximum pulse voltage, V_P, applied to the wire. The blue line is I_{SW} which decreases and then increases with increasing pulse amplitude. The red line is R_N which stays constant and then decreases. This is a counterintuitive result that has been reproduced on several nanowires of which a, b, c and d are four examples. The dashed line indicates where both R_N and I_{SW} begin to rapidly decrease. Applying pulses smaller than the maximum previous applied pulse does not lead to a significant change in I_{SW}. a) A nanowire with starting $I_{SW} = 12.2\mu$A. The dashed line is at 1.105V. I_{SW} returns to 11.0μA before the wire abruptly breaks. b) A wire with similar fabrication parameters to the one shown in a (the axes are the same for graphs a and b). The starting $I_{SW} = 8.5\mu$A. The dashed line is at 1.150V. I_{SW} returns to a maximum of 10.9μA (which is greater than the starting I_{SW}) before decreasing again until the wire breaks. c) A third example nanowire with starting $I_{SW} = 10.3\mu$A and ending $I_{SW} = 8.5\mu$A. The dashed line is at 0.502V. Images of this wire before and after pulsing are shown in Figure 4.7. d) A nanowire fabricated on a MWNT instead of a fluorinated SWNT with starting $I_{SW} = 26.5\mu$A and ending $I_{SW} = 11.4\mu$A. The dotted line is at 0.947V.

observe phase slip centers in the VI curves (see figure 4.3e) indicating less homogeneous nanowires. As pulse voltage is further increased, these phase slip centers gradually disappear. The wire can return to a I_{SW} approaching the starting I_{SW} (see figure 4.3b) or even exceeding it (see figure 4.3f). From these types of VI curves, we can extract the switching current, I_{SW}, using threshold detection and the normal resistance, R_N, using linear fitting and plot the data versus pulse number or pulse voltage, V_P, across the nanowire. The effect as V_P is increased from 0 to 0.326V in 5mV steps is shown in figure 4.4a. For the lowest voltage pulses, we primarily observe scatter from the natural stochasticity of the switching current [23]. In order to minimize this natural stochasticity, we averaged over 100 switching current measurements between pulses. As V_P is increased, we observe an increasing stochasticity of I_{SW} which quickly becomes greater than the natural stochasticity of the switching current. As the pulse voltage increase further, we see the irreversible drop of the switching current observed in the VI curves. We can use this combined downward trend and increased stochasticity to precisely set I_{SW} to a desired value. As shown in figure 4.1, I_{SW} is set to ten values chosen uniformly from 0.95μA to 0.05μA. Three examples of pulse sequences used to do this are shown in figure 4.4. Large pulses are used to approach the desired value and then smaller pulses (with their enhanced stochasticity) are used to 'bounce' the switching current to within $\approx$ 10nA of the desired value. For each of the ten chosen target values, the switching current was set to the desired value.

The decrease and return of I_{SW} seen in the VI curves can be plotted versus V_P in a similar fashion. It should be noted that as the switching current goes through its minimum it is poorly detected by this threshold detection scheme. The drop, saturation and return of I_{SW} can be see in figure 4.5. The initial drop of I_{SW} does not have a corresponding change in R_N. When I_{SW} reaches a minimum and begins to return, R_N begins to drop. This behavior was reproduced on many nanowires (of which figure 4.5 contains four examples). The resistance versus temperature curves taken after a series of pulsing (see figure 4.6a and 4.6b) show behavior consistent with the observed I_{SW} and R_N behavior (for the RT curve,

the low bias current signal was reduced from ≈1-10 μA to $10 - 20$ nA to measure the RT curve in the linear regime). The RT curves generally demonstrates one transition indicative of a homogeneous wire with fitting parameters similar to unpulsed nanowires (see figure 4.6c and 4.6d). The critical temperature of the nanowire decreases as pulse voltage increases saturating at a minimum. Further increase of pulse voltage results in the increase of T_C and the drop in R_N (see figure 4.6e and 4.6f).

SEM imaging (figure 4.7 a and b) before and after pulsing show virtually no change in the nanowire ruling out the formation of obvious weak links (small scale weak links below the resolution of the SEM are still possible). To more thoroughly study the pulses effect on the nanowires, we turn to in-situ TEM experiments. TEM experiments require different samples than those described previously. Most importantly, the nanowire must be across an open slit for TEM observation. We deposit multi-walled carbon nanotubes (MWNTs) across TEM compatible slits to generate these samples [28]. Briefly, we use a KOH etch to fabricate a V-shaped cut in a silicon chip coated on both sides with 100 nm of silicon nitride. The V-shaped cut almost pierces the chip except for approximately 5 microns of remaining silicon. This silicon is cracked by sonicating in deionized water for less than a second. A 30-60 second KOH etch removes the cracked silicon leaving an approximately 100 nm wide silicon membrane. This membrane is removed by RIE etching from the etch pit side. The membrane is supported during the RIE step by a piece of polydimethylsiloxane (PDMS). In the method previously described [28] we removed the silicon nitride entirely and oxidized the silicon to form an insulating layer. By etching the silicon nitride from the etch pit side, we are able to use the silicon nitride as the insulating layer thus skipping the oxidizing step. With these samples, we were able to perform in-situ TEM experiments to directly determine the high bias voltage pulses effects on metal coated nanotubes. MWNTs were used rather than the SWNTs used for regular nanowire samples. MWNTs are more robust and rigid and thus can more easily be deposited on the TEM compatible slits [28]. The change in scaffold does not affect the pulsing behavior (see figure 4.5d). The in-situ

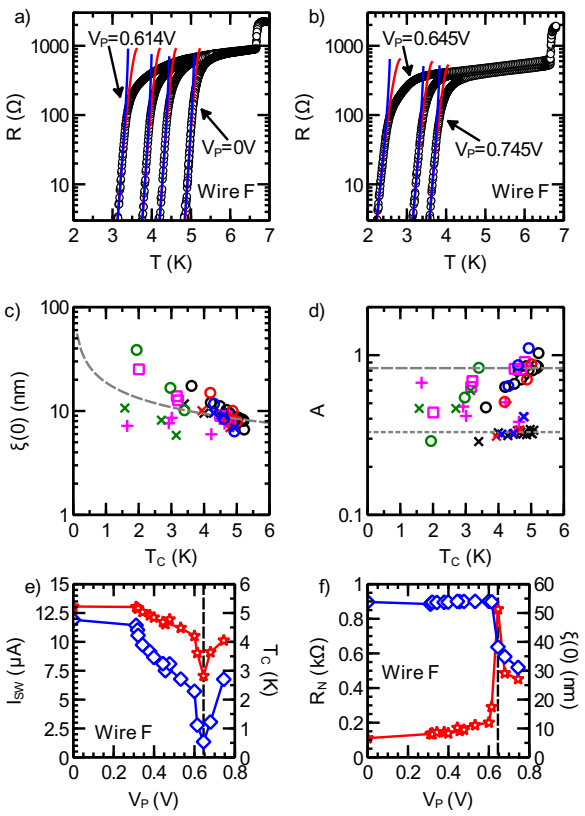

Figure 4.6: Resistance vs temperature curves and fits. a) Four RT curves taken as pulsing generally drives I_{SW} down with no change in R_N. From right to left, the corresponding pulse voltages are 0V, 0.456V, 0.600V and 0.614V. The red curves are best fits to a TAPS model while the blue curves are best fits to a QPS model (see text for details). b) Three RT curves taken when I_{SW} returns for the same wire as shown in a (the axes on a and b are the same). From left to right the pulse voltages are 0.645V, 0.679V and 0.745V. c) $\xi(0)$ plotted versus T_C. Circles and x's are fits to nanowires that have been pulsed using TAPS and QPS respectively. The different colors represent different wires. The squares and plus symbols are TAPS and QPS fits to unpulsed nanowires of different lengths and cross-sections. The dotted line is the theoretical estimate for $\xi(0)$. d) A_T and A_Q plotted versus T_C. Again circles and x's represent thermal and quantum fits respectively for pulsed wires with different colors representing different wires. Squares and plus symbols represent thermal and quantum fits respectively for unpulsed wires. The dotted lines are estimates for the factors $A_T = 0.83$ and $A_Q = 0.33$. e) Plot of I_{SW} and T_C (from the TAPS fit) vs V_P for the wire whose RT curves are shown in a and b (not all the RT curves were shown in a for clarity). The diamonds correspond to I_{SW} and the stars correspond to T_C. The dotted line is at 0.645V where the turn around from decreasing to increasing behavior occurs. f) R_N and $\xi(0)$ (from the TAPS fit) vs V_P. The diamonds correspond to R_N and the stars correspond to $\xi(0)$. Initially R_N is flat while $\xi(0)$ shows a growing trend (since T_C is dropping). After V_P reaches 0.645V (indicated by the dotted line) R_N begins to drop and $\xi(0)$ returns to a higher value (because of the return of T_C and the increase of the mean free path).

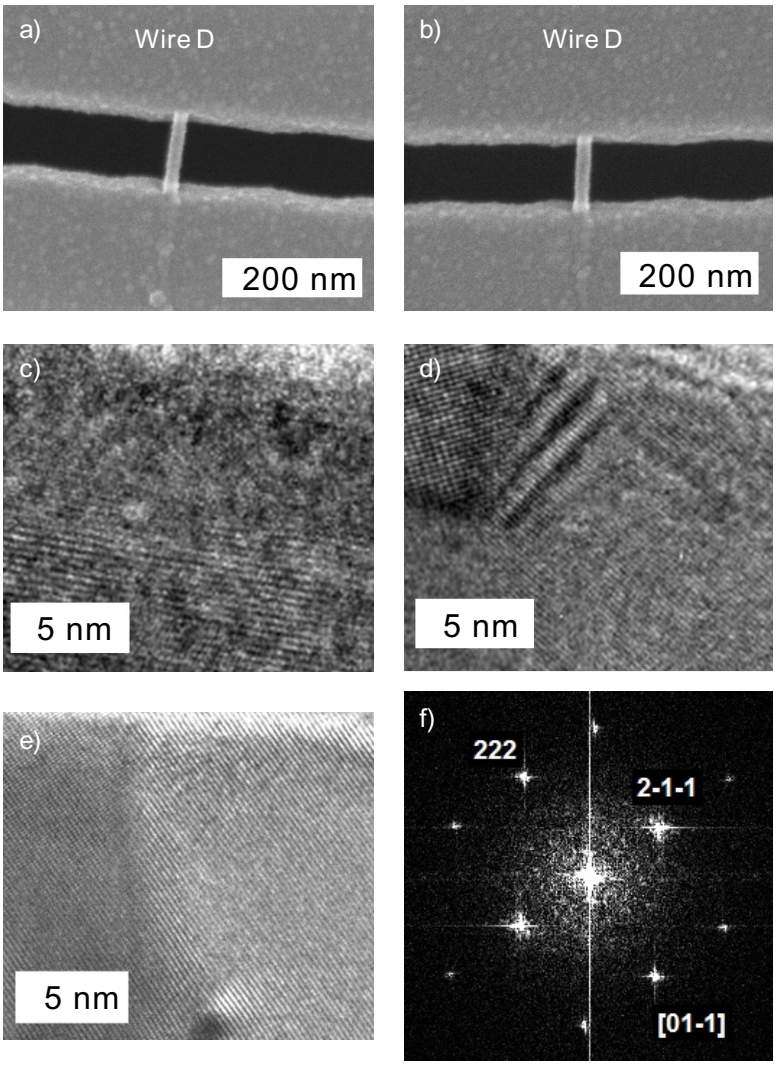

Figure 4.7: SEM and TEM analysis a) SEM image of a nanowire before pulsing at cryogenic temperatures b) the same nanowire as a after pulsing at cryogenic temperatures with a maximum pulse voltage applied of 588mV. Switching current of the wire was reduced from 10.3μA down to a minimum and then back to 8.5μA as shown in figure 4.5c. Note no obvious weak links are visible. c) In-situ TEM imaging of a nanowire (at room temperature) exposed to pulsing. Before pulsing, the nanowire is amorphous (the crystalline structure visible is the underlying MWNT). d) After pulsing to 2.935V, the wire becomes polycrystalline. e) After pulsing to 3.735V, the nanowire becomes a single crystal. f) Diffraction pattern of the crystal shown in e.

TEM experiments must be done at room temperature while superconducting measurements must be done at cryogenic temperatures. We do not expect this change in base temperature to produce a significant difference as both experiments are performed under vacuum and the nanowire itself is expected to reach a high temperature ($\approx$ 2000K) under high bias voltage ($\approx 0.5\,\mathrm{V}$). From the in-situ TEM experiments we see that initially the wire develops a polycrystalline section which expands as increasing pulses are applied. The crystals do not necessarily remain static for the duration of the experiment but rather are dynamic entities that develop and change. The polycrystalline nature of the wire gradually becomes dominated by fewer and fewer crystal domains and becomes an almost perfect single crystal nanowire. It should be noted that although inhomogeneities such as grain boundaries appear in the wire, the overall diameter of the wire does not appear to be significantly altered. The crystallization of MoGe from a high voltage pulse is not surprising in light of similar crystallization obtained by exposure of MoGe nanowires to electron beam radiation [50]. To avoid electron beam induced crystallization in our TEM images, dosage from the electron beam was minimized for all TEM images. As further evidence that the high bias pulses and not the electron beam of the TEM were responsible for the crystallization observed, the same crystallization was seen in nanowires constantly imaged during the pulse process as was seen in wires that were not imaged until the pulse process was complete. In the first TEM image, the multiwalled nanotube (with wall spacing 3.3 Å) covered with amorphous $Mo_{76}Ge_{24}$ is visible (see figure 4.7 c). The measured line spacing in the image is 3.2 ± 0.1 Å. After some pulsing, a polycrystalline structure is visible with the predominant line spacing being 2.2 ± 0.1 Å. Only in the upper left hand corner is the line spacing different 2.5 ± 0.1 Å(see figure 4.7 d). In the final TEM picture the single crystal line spacing is 2.2 ± 0.1 Å(see figure 4.7 e).

4.3 Discussion

SEM and TEM imaging do not show any formation of weak links due to pulsing. Thus the reduction of the critical current can not be explained by weak links and we need to find an alternative explanation. Note also that weak links would only account for the reduction of switching current and not explain the observed return of the switching current with increased pulse voltage. The dynamic, increased stochasticity of the critical current and the decrease and return of the critical current correlates well with the observed TEM behavior. Most forms of crystalline MoGe have lower T_C's than amorphous MoGe [51] so it is not surprising that the crystallization of MoGe would reduce the wire's critical temperature. It can be expected that any crystallization or segregation of the MoGe alloy from the large current pulse would produce a reduction of T_C. TEM imaging shows that a polycrystalline morphology appears with voltage pulsing. Following the work of Rogachev et al. [9], we can expect these polycrystalline wires to maintain homogeneous wire behavior and can fit them using standard nanowire theory. Also in agreement with these previous results, we see phase slip centers develop in the VI curve (see figure 4.3e) at temperatures near T_C (as we are changing T_C while keeping T fixed, these are most evident when T_C is small).

Electromigration is a well studied effect for modifying and fabricating nanostructures [52–54]. The observed crystallization of the MoGe is most likely caused by a combination of electromigration and Joule heating induced thermal effects. It appears that thermal effects are dominant since we observe the appearance of crystals at the center hottest spot of the wire and also do not observe the weak link formation associated with electromigration. As a rough approximation of the temperature of the nanowire, we can write the applied voltage as a function of temperature (assuming a constant resistivity): $V^2/4 = L(T^2 - T_0^2)$ where V is the voltage of the pulse, $L = 2.4 \times 10^{-8} W\Omega/K^2$ is the Lorenz number, T is the temperature of the wire center and T_0 is the temperature of the electrodes [55]. Typical values (V=0.5V) gives us an estimated temperature of $T = 1725$K close to the crystalizing temperature

of MoGe. This high temperature further indicates that the difference between cryogenic temperatures $T_0 = 0$ and room temperature TEM measurements $T_0 = 300K$ can safely be neglected. It should be noted that this rough approximation indicates that the natural choice of coordinates for figure 4.5 is pulse voltage (and not pulse current or power). The modification of critical temperature as a result of an applied voltage pulse is not surprising when one considers that the entire material properties of the nanowire may be changed. The particular crystal form of MoGe closest to our starting concentration of $Mo_{76}Ge_{24}$ is Mo_3Ge which is actually an A15 compound which are known to have high T_C's. Studies on Mo_3Ge reveal that its T_C is highly dependent on formation conditions (i.e. it can have a very low T_C) but under the correct formation conditions, the T_C can exceed 5.7K (comparable to the critical temperature of the starting amorphous MoGe) [51].

It has been observed experimentally that Mo_3Ge can be generated by heating amorphous MoGe to high temperatures [56]. Thus we propose that the return and sometimes higher I_{SW} is caused by the formation of relatively well-ordered crystal Mo_3Ge from Joule heating by the high bias pulses. The initial decrease of I_{SW} (or T_C) is caused by partial crystallization of the wire where nanocrystals are mixed with the amorphous phase. It should be noted that other effects may also play a role. The crystalline nature could lead to an enhanced proximity effect originating from the superconducting electrodes allowing an increased measured T_C. Another possibility is that carbon dopants being released from the carbon nanotube are affecting the critical temperature. The dependence on dopants seems unlikely as similar behavior was observed for both single walled fluorinated carbon nanotubes and multiwalled regular carbon nanotubes which would contain significantly different amounts of dopants (see figure 4.5 d).

By comparing x-ray diffraction data for Mo_3Ge [56] and our TEM images, we can confirm that Mo_3Ge is being formed by the pulses. In agreement with the x-ray diffraction data, our most commonly observed orientations are 210 (2.1993 Åfrom x-ray diffraction) and 211 (2.0031 Åfrom x-ray diffraction). Our measurement of 2.2 Å by itself is not accurate enough

to tell the difference between these two orientations. From further analysis of the TEM images, we retrieve that the spacing of the crystal in the 222 direction is 1.5 Å (compared to 1.4215 Å from x-ray diffraction). For the 211 direction, we measure 2.1 Å (compared to 2.0031 Å from x-ray diffraction). On the upper left hand corner of the polycrystal, we observe a spacing of 2.5 Å (compared to 2.4557 Å from x-ray diffraction) for the 200 and 3.3 Å for the 110 direction (compared to 3.4724 Å from x-ray diffraction). Both these orientations are significantly less common than the others which dominate the images. In all cases, there is significant correlation between our values and the x-ray diffraction data indicating that the crystal we are generating is indeed Mo_3Ge [56].

4.4 Analysis

To compare to previous experiments on nanowires we use a phenomenological Little fit [12]: $R(T) = R_N \exp\left(-\Delta F(T)/k_B T\right)$ where R_N is the normal resistance of the nanowire, $\Delta F(T)$ is the free energy barrier for phase slips, k_B is the Boltzmann constant and T is temperature [3, 12, 33, 35]. The temperature dependence of the free energy barrier is accurately given at all temperatures by the Bardeen formula [39]:

$$\Delta F(T) = \Delta F(0)\left(1 - (T/T_C)^2\right)^{3/2} \tag{4.1}$$

This temperature dependency expression is applicable in a much wider temperature range than the more traditional Ginzburg-Landau temperature dependence

$$\Delta F(T) = \Delta F(0)\left(1 - (T/T_C)\right)^{3/2}$$

which is only valid close to Tc. We can express $\Delta F(0)$ using experimentally accessible parameters [40]:

$$\Delta F(0) = A_T \frac{R_Q}{R_N} \frac{L}{\xi(0)} k_B T_C \tag{4.2}$$

where A_T is a numerical factor of order unity, R_Q is the resistance quantum, R_N is the normal resistance of the nanowire (which we define as the resistance immediately after the film goes superconducting), L is the length of the nanowire (which can be determined from SEM imaging), T_C is the critical temperature and $\xi(0)$ is the coherence length. We typically use T_C and $\xi(0)$ as fitting parameters (with $A_T = 1.76\sqrt{2}/3 = 0.83$ [40]) but to compare to the quantum phase slip models mentioned below we will at times fix ξ and use T_C and A_T as fitting parameters. Using our pulsing technique we can track the evolution of a single nanowire as it is pulsed. Since normal resistance shows initially no change while critical current drops, we expect the drop of critical current to have an associated drop in critical temperature. We can anticipate the evolution of the coherence length as critical temperature changes using the formula for coherence length of a dirty superconductor:

$$\xi(0) = 0.855\sqrt{\frac{l\hbar v_F}{1.76\pi k_B T_c}} \tag{4.3}$$

[3] where l is the mean free path of MoGe (≈ 3.5 Å) and v_F is the Fermi velocity ($\approx 1 \times 10^6$ m/s). It should be noted that as the wire becomes crystalline Mo_3Ge, we anticipate an enhanced coherence length due to the longer mean free path of the crystal compared to amorphous MoGe. From a simple Drude model of resistivity, a longer mean free path implies a decreased normal resistance in agreement with the observed drop in resistance with extended pulsing. The fitted TAPS coherence length increases with decreasing critical temperature but more drastically than would be predicted theoretically (circles in figure 4.6c). We only include fits for wires where R_N has not started to drop indicating that the coherence length is still similar to that of unpulsed MoGe. For comparison, fits to several unpulsed wires are also included as squares on the graph and the high level of overlap indicates that pulsed nanowires without reduced R_N are acting as homogeneous nanowires with reduced critical temperatures. It is possible that this observed deviation from the predicted coherence length is due to quantum phase slips dominating thermally activated

phase slips at low enough temperatures. Golubev and Zaikin have proposed a model where the rate of the quantum phase slips (and thus the resistance) is given by:

$$R(T) \approx R_N \exp\left(-A_Q R_Q L / R_N \xi(T)\right) \tag{4.4}$$

where A_Q is a numeric constant of order unity, R_Q is the quantum resistance, R_N is the normal resistance, L is the length and $\xi(T)$ is the coherence length, which is the only temperature dependent term [16, 19]. Since the expression (similar to the one for TAPS) is dominated by the exponential, the exact form of the pre-factor is not particularly important. For a more direct comparison to our TAPS fit, we have assigned the prefactor to be R_N. The Ginzburg-Landua temperature dependence for coherence length is $\xi(T)/\xi(0) = 1/\sqrt{1 - T/T_C}$. We can also consider a heuristic MQT model following Giordano:

$$R = R_N \exp\left(-\Delta F / (\hbar/\tau_{GL})\right) \tag{4.5}$$

where τ_{GL} is the Ginzburg-Landau time and $\hbar/\tau_{GL} = 8k_B/\pi T_C(1 - T/T_C)$ [14, 15]. We can simplify equation (4.5) by using equations (4.2) and the Ginzburg-Landau temperature dependence for the free energy (which is more appropriate when comparing to the temperature dependence from the Ginzburg-Landau time) to get:

$$R = R_N \exp\left(-\frac{1.76\pi\sqrt{2}}{24}\frac{R_q}{R_N}\frac{L}{\xi(0)}\left(1 - (T/T_C)\right)^{1/2}\right) \tag{4.6}$$

Note that we get the same general form and temperature dependence as the Golubev Zaikin model though the underlying physical reasoning involved in arriving at this result is different [19]. Following Giordano and Lau et al. equation (4.5) is often expressed with additional fitting parameters of order unity in the exponent and in the prefactor (e.g. see equation (2) in reference [13]). If we assume these fitting parameters of order unity are actually equal to 1, equation (4.6) gives us a very rough estimate for the numeric prefactor

A_Q to be $A_Q \approx 1.76\pi\sqrt{2}/24 = 0.33$. Thus we have a choice of either assuming A_Q is indeed equal to this value and using $\xi(0)$ as a fitting parameter (in a similar way to the TAPS fits) or assuming that $\xi(0)$ is given by equation (4.3) and using A_Q as a fitting parameter (to compare to the TAPS fits, we will likewise assume $\xi(0)$ is given by equation (4.3) and use A_T as a fitting parameter). As a final comparison, a macroscopic quantum tunneling (MQT) model based on the WKB approximation (in the same way as for a Josephson junction) would yield:

$$R = R_N \exp\left(-2\pi\Delta F/(\hbar\omega_p)\right) \tag{4.7}$$

Where $\omega_p = (2eI_C/\hbar C)^{1/2}$ is the plasma frequency [3]. By noting that the only temperature dependent term in ω_p is I_C (which we know the temperature dependence from equation (4.1)) and noting that MQT can only be detected if $\hbar\omega_p$ approaches $k_B T_C$ we can simplify equation (4.7) to:

$$R = R_N \exp\left(-A_Q \frac{R_q}{R_N}\frac{L}{\xi(0)}\left(1-(T/T_C)^2\right)^{3/4}\right) \tag{4.8}$$

Again the form and temperature dependence of this expression are similar to the Golubev-Zaikin model. Using these expressions, we can thus perform fits with both TAPS and QPS theories. We choose the temperature dependence from the WKB approximation (4.8) though the other models would not yield significantly different results as the temperature dependences are similar. If the chosen theory well describes the system, we should anticipate that $\xi(0)$ will closely follow equation (4.3) or equivalently that the prefactor A is a constant value of order unity preferably close to the theoretical estimates. Figure 4.6c) shows that the coherence length from the TAPS fit tends to diverge somewhat faster than can be accounted for by 4.3 while the predicted quantum coherence length (calculated by assuming that $A_Q = 0.33$) is more flat. Thus it is possible that some quantum effects are present which would explain the greater than expected coherence length from the TAPS fit. We can alternative assume $\xi(0)$ is given by equation (4.3) and use A_T and A_Q as fitting parameters (see figure 4.6d). In this case, both the quantum and thermal parameters start close to

their predicted values for high critical temperature and then diverge from nearly constant predicted values as T_C is reduced and it is not clear which is the preferred model. Thus it is premature to describe this effect as quantum as it appears that the TAPS model can produce at least as satisfactory a description of the behavior of the nanowires. More work needs to be done to distinguish between quantum and thermal effects using this approach. Note that there is a high degree of overlap between fitting parameters of pulsed nanowires (circles and x's) and unpulsed nanowires (squares and plus symbols) indicating that it is fair to treat a pulsed nanowire using a similar theoretical description to an unpulsed nanowire. As shown in figure 4.6e, the decrease and return of I_{SW} corresponds to a drop and return of T_C as expected. In figure 4.6f we see that while R_N is stable (indicating mean free path is not changing considerably) coherence length is gradually increasing (as expected from the corresponding decrease in T_C). When I_{SW} returns, there is a corresponding drop in R_N and the coherence length has returned to a higher value than it started from. This is not surprising as an increase in mean free path (from crystallization of the MoGe) would result in both a drop in R_N and a longer coherence length.

4.5 Conclusion

We have studied the effects of high bias voltage pulses on superconducting MoGe nanowires. We observed a repeatable decrease, minimum and then increase of the switching current as pulses get stronger. The normal resistance at first is constant and then decreases. The effective critical temperature of the nanowire decreases and then increases corresponding to the switching current behavior. SEM imaging reveals little change in the nanowire shape upon pulsing. In-situ TEM experiments indicate the nanowire goes from amorphous to polycrystalline to single crystal form. These forms of the nanowire correspond to the observed transport behavior of the nanowires with a reduced switching current and phase slip centers showing up in the polycrystalline form and an enhanced switching current and disappear-

ance of the phase slip centers in the single crystal form. Further analysis indicates that the crystalline form is Mo_3Ge, a high critical temperature A15 compound. The high bias pulse appears to change the nanowire by primarily Joule heating rather than electromigratory effects. We also demonstrate that controlled pulsing can be used to set precisely the switching current of the nanowire to a desired value, which enables various applications, the most obvious example being a superconducting nanowire qubit.

Chapter 5

MQT studies of single nanowires

We detect quantum phase slips (QPS) in thin superconducting wires by measuring the dispersion of the switching current. In particular, we examine a new regime of nanowires where the single phase slip behavior mimics the macroscopic quantum tunneling (MQT) behavior seen in Josephson junctions. By varying parameters of the system such as capacitance (using photolithography), resistance, critical current and morphology (all using controlled application of high bias voltage pulses), we can probe single phase slips in much more detail than was previously possible. Most importantly, by varying the damping parameters of the nanowires, we modify the crossover temperature of quantum phase slips in a manner entirely consistent with MQT in an overdamped system.

5.1 Introduction

MQT of phase slips or quantum phase slips (QPS) was recently detected in nanowires [23] by measuring switching current distributions. The data was successfully modeled at high temperatures using a theory for multiple thermally activated phase slips. In particular, this model explains why standard deviation decreases as temperature increases [23, 49] which is opposite of what is commonly observed for Josephson junctions (JJs) [24]. For sufficiently low temperatures, one can expect a single phase slip is sufficient to switch the wire to the normal state. The thermally activated multiple phase slip model ceased to fit the data at sufficiently low temperatures and the data was successfully fit using a model based on single quantum phase slips [23, 49]. Interestingly, there is no obvious transition visible in the

standard deviation vs temperature data indicating the onset of quantum tunneling. This is again unlike the case for JJs where it has been experimentally confirmed that the observed saturation of the standard deviation vs temperature is due to MQT [22]. This is quite surprising as the underlying theory for single phase slips and Josephson junctions are very similar. We build on these previous experiments to explore the relationship between critical current and dispersion of the switching current. By exploring new nanowire parameters, particularly nanowires with higher critical currents and critical temperatures, we observe the expected behavior in nanowires of constant standard deviation in the quantum dominated region and increasing standard deviation with increasing temperatures in the thermal region. We also use our recently developed pulse modification technique [57] to explore QPS in amorphous and single crystal nanowires. This technique allows us to follow dispersion vs critical current for a single nanowire. These results indicate that it is highly unlikely that other interpretations such as electromagnetic noise or inhomogeneity are the causes for the behavior of the dispersion observed.

5.2 Experiment

Superconducting nanowires were fabricated by molecular templating [20]. Briefly, a single wall nanotube is suspended across a trench etched in a silicon wafer coated with 500 nm silicon oxide and 60 nm silicon nitride. MoGe is deposited and the nanotube serves as a scaffold allowing the formation of a nanowire. A wire is selected for measurement by scanning electron microscope (SEM) imaging. Once a wire has been chosen, photolithography is performed to select a particular wire. The leads approaching the wire are 20 μm across leading to a shunting capacitance of approximately 1-10 fF [10]. For samples C and D, we instead used an electrode with width 5 μm effectively decreasing the expected capacitance by a factor of 4. The trench has been undercut to prevent additional conduction paths from one electrode to another except for the nanowire. The wires were measured in a

He-3 cryogenic system with π filters and copper powder filters whose noise has been well characterized [23]. The nanowires were measured in a standard four probe configuration with a low noise sinusoidal current source.

For resistance vs temperature measurements, a low bias current of 10-20 nA was applied at a frequency of approximately 11 Hz. For switching current distributions used for determining escape rate, mean switching current and standard deviation, a higher bias was applied (1-10 μA) again at approximately 11 Hz. For all distributions, 10,000 points were collected.

We used high bias pulses to both crystalize the nanowire and set the critical current [57]. Briefly, using relays (voltage controlled switches) the measurement apparatus is disconnected and high bias voltage pulses are applied. These allow us to systematically change the critical current. The critical current at first reduces and then returns when the amorphous molybdenum germanium ($Mo_{76}Ge_{24}$) becomes single crystal Mo_3Ge. The return of the critical current has an associated drop in normal resistance. This allows us to probe nanowires with similar critical currents but different normal resistances.

5.3 Results

In figure 5.1, the standard deviation vs temperature behavior for four unpulsed and two pulsed wire are shown as blue circles. At sufficiently low temperatures, it is predicted a single phase slip will be sufficient to drive the nanowire into a Joule heated normal state [23]. The rate for this process can be written as:

$$\Gamma = A(I) \exp\left(-B\left(1 - I/I_C\right)^b\right) \tag{5.1}$$

where $A(I) = \Omega(I)/2\pi$ is a characteristic frequency suitable for nanowires, I is the current and I_C is the critical current [46]. Furthermore, $B = U_C/kT_{esc}$ where U_C is the effective free

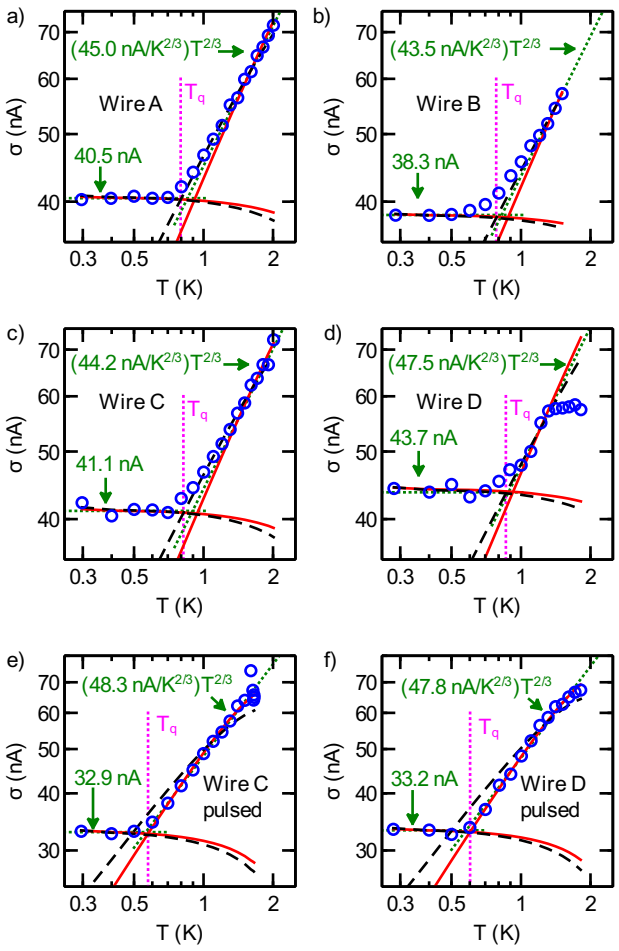

Figure 5.1: Standard deviation vs temperature for four unpulsed nanowires (a-d) and two pulsed nanowires (e-f) are shown as blue circles. The solid red line is the fit for expected standard deviation of the switching current using equation (5.2) with the LA model, $b = 5/4$, and $T_{esc} = T$ or $T_{esc} = T_q$. The dashed black line is a fit for the expected standard deviation of the nanowire using the cubic form, $b = 3/2$, with $T_{esc} = T$ or $T_{esc} = T_q$. The green dotted lines are straight line fits to a constant and a 2/3 power law. The dotted magenta line is at T_q from the best fit (see table 5.1 for values) and corresponds well with the visual crossover from quantum to thermal behavior. The nearly horizontal part to the left of the T_q line corresponds to the quantum regime and the angled part to the right of the T_q line is the thermally dominated region. The axes of graphs (a-d) are the same.

energy barrier at zero bias current and T_{esc} is the escape temperature [22]. In the thermally dominated region $T_{esc} = T$ (from a simple Arrhenius law argument) and in the quantum dominated regime $kT_{esc} = kT_q \approx \hbar\omega_p/2\pi$ using a Wentzel-Kramers-Brillouin (WKB) approximation (T_q represents the effective temperature associated with quantum escape). A

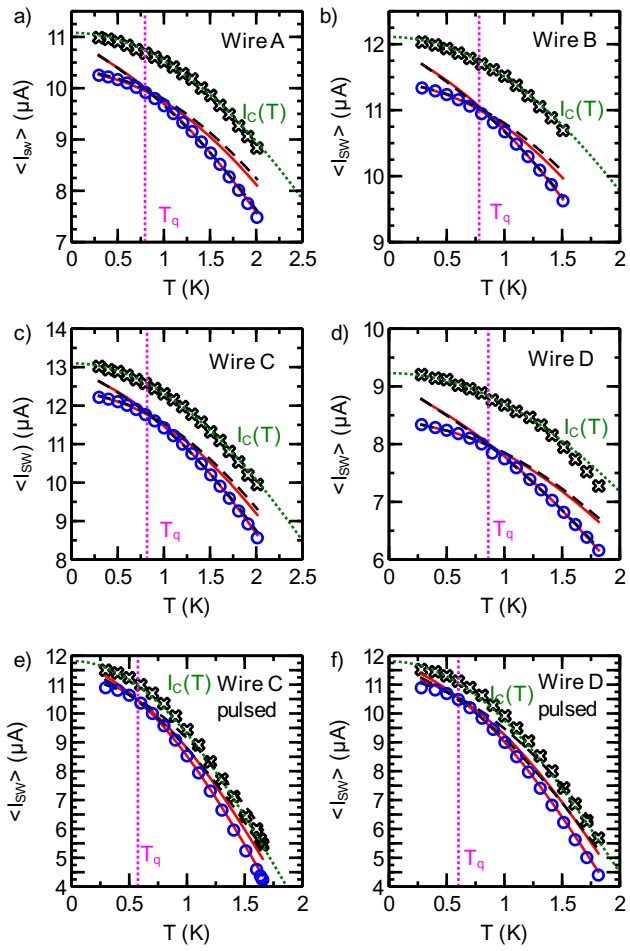

Figure 5.2: Mean switching current vs temperature for the four unpulsed nanowires (a-d) and two pulsed nanowires (e-f) shown in figure 5.1. The solid red line is the fit for expected mean switching current of the nanowire using the escape rate given in equation (5.1) with the LA model, $b = 5/4$. . The dashed black line is a fit for the expected mean switching current of the nanowire using the cubic form with $b = 3/2$. The magenta dotted lines are the T_q from the fit and correspond well to the transition from the thermally dominated to the quantum regime. The green dotted line is $I_C(T)$ using equation (5.3) and I_{C0} from table 5.1 and show that switching is premature in all cases. The black crosses are calculated from the mean switching current and standard deviation for each point using equation (5.5).

more precise formula for quantum escape with moderate damping has been calculated by Caldeira and Leggett [58]. Due to the temperature independence of T_{esc} in the quantum regime, the standard deviation will be roughly constant as a function of temperature. In the thermal regime, the temperature dependence will result in standard deviation increasing as temperature increases following a $1/b$ power. If the free energy barrier can be well

approximated by a cubic, it is well known that $b = 3/2$ [46]. A common way to show this dependence is to plot standard deviation vs temperature on a log log graph (see for example reference [24]). In figure 5.1 the constant quantum regime and the 2/3 power thermal regime are indicated by the green dotted lines with the full expressions for each line indicated in each graph.

As shown by Garg, the standard deviation, σ, of the resulting probability distribution induced by an escape rate with the form in equation (5.1) [46] is given to first order by the expression:

$$\sigma = I_C \frac{\pi}{\sqrt{6} b \ln X} \left(\frac{\ln X}{B} \right)^{1/b} \tag{5.2}$$

where $X \approx A\Delta t$ (Δt is the time spent sweeping through the transition). Since X only appears in the logarithm, its exact value is fairly unimportant. To estimate X, we assume that $\Delta t = \Delta I / \dot{I}$ where $\dot{I}$ is the experimental sweep speed and ΔI is approximately given by the experimentally measured standard deviation. Furthermore, we estimate that $A \approx 10^{12}/2\pi$ Hz since the kinetic inductance of our nanowires, L_k, is on the order of 1 nH while the capacitance, C, is given by the geometry of the leads and is approximately 1 fF [10] (which implies the characteristic frequency associated with our nanowires is $\Omega = (L_k C)^{-1/2} \approx 10^{12}$ Hz).

For one-dimensional superconducting nanowires, the Langer-Ambegaokar (LA) model [33] indicates $U_C = \sqrt{6}\hbar I_C/2e$ and $b = 5/4$ [41] (in contrast to the previously mentioned cubic model where $b = 3/2$). In figure 5.1, we plot fits for both the LA model, $b = 5/4$ (shown by the red solid curve), and the cubic model, $b = 3/2$ (shown by the black dashed curve). We show fits for both thermally activation, $T_{esc} = T$, and quantum tunneling, $T_{esc} = T_q$, where T_q is a fitting parameter that is constant as a function of temperature. We assume the zero bias current free energy barrier is given by a modified LA expression: $U_C = D\sqrt{6}\hbar I_C/2e$

where D is a fitting parameter close to 1. I_C is given by the Bardeen expression [39]:

$$I_C = I_{C0}\left(1 - (T/T_C')^2\right)^{3/2} \tag{5.3}$$

where I_{C0} and T_C' are fitting parameters. I_{C0} is the critical current at zero temperature while T_C' corresponds to the critical temperature (we denote it with a prime to distinguish it from the critical temperature arrived at using resistance vs temperature fits which we label T_C). While fitting the standard deviation vs temperature behavior, we simultaneously fit the corresponding mean switching current (shown as blue circles in figure 5.2) using the expression for the mean switching current to first order [46]:

$$\langle I_{SW}\rangle = I_C\left[1 - \left(\frac{\ln X}{B}\right)^{1/b}\right] \tag{5.4}$$

In figure 5.2, we plot fits for both the LA model, $b = 5/4$ (shown by the red solid curve), and the cubic model, $b = 3/2$ (shown by the black dashed curve). As before, we plot fits for both thermally activation, $T_{esc} = T$, and quantum tunneling, $T_{esc} = T_q$. T_q for the best fit is indicated by a vertical dotted line in both figures 5.1 and 5.2. Equations (5.4) and (5.2) can be combined to yield an expression for estimating the critical current, I_C, from a given mean switching current and standard deviation:

$$I_C = \langle I_{SW}\rangle + \sigma\frac{\sqrt{6}b\ln X}{\pi} \tag{5.5}$$

We plot this estimate in figure 5.2 as black crosses and it agrees well for all points with equation (5.3) which is shown as a green dotted line.

The fitting parameters for the best fit are shown in table 5.1. For the unpulsed wires, the best fit was found with the cubic model, $b = 3/2$, and for the pulsed wires the best fit was found with the LA model, $b = 5/4$. It should be noted that b was assumed to be the same for the thermal and quantum regimes for ease of fitting.

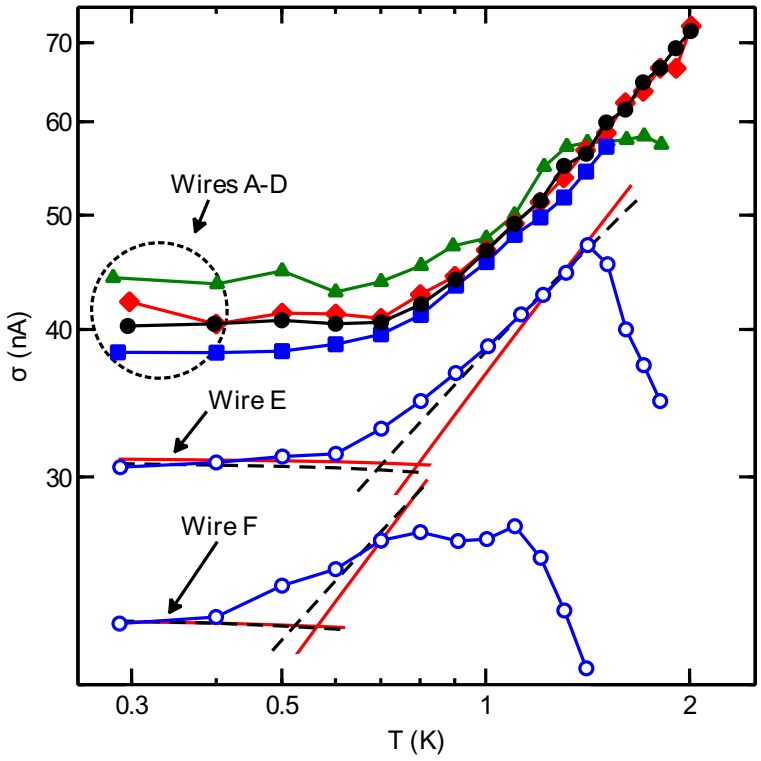

Figure 5.3: Standard deviation vs temperature for all 6 unpulsed nanowires (A-F). The fits for wires E and F corresponding to the fits for wires A-D in figure 5.1 are shown. The reduction of standard deviation for high temperature seen in wires E and F is expected to be due to multiple thermally activated phase slips.

Note that for all wires the critical current at zero temperature, I_{C0}, is slightly higher than the switching current at base temperature, I_{SW0}. The critical temperature used to fit the mean and standard deviation of the switching current, T_C' is relatively close to the critical temperature used to fit the resistance vs temperature behavior, T_C. The resistance vs temperature curves are fit using a phenomenological Little fit [12]: $R(T) = R_N \exp\left(-\Delta F(T)/kT\right)$ where R_N is the normal resistance of the nanowire and $\Delta F(T)$ is the free energy barrier for phase slips given by:

$$\Delta F(T) = 0.83 \frac{R_q}{R_N} \frac{L}{\xi(0)} kT_C \left(1 - (T/T_C)^2\right)^{3/2} \tag{5.6}$$

where R_Q is the resistance quantum, R_N is the normal resistance of the nanowire, L is the

Table 5.1: Table of fitting parameters

Wire	b	I_{C0} (μA)	I_{SW0} (μA)	T_C' (K)	T_C (K)	D	T_q (K)	σ_0 (nA)	R_N (Ω)	L (nm)
A	3/2	11.08	10.25	5.51	5.01	1.095	0.796	40.3	1152	115
B	3/2	12.11	11.33	5.48	4.92	1.226	0.781	38.3	1864	221
C	3/2	13.10	12.22	4.99	4.81	1.184	0.818	42.2	975	100
D	3/2	9.23	8.34	5.09	4.69	0.932	0.860	44.3	1011	94
C (p)	5/4	11.82	10.89	2.60	3.56	0.669	0.575	33.0	426	100
D (p)	5/4	11.81	10.89	2.90	3.58	0.694	0.602	33.4	463	94
E	3/2	5.94	5.34	4.57	4.49	1.074	0.691	30.6	1393	91
F	3/2	4.25	3.82	3.29	3.20	1.094	0.521	22.5	1507	130

length of the nanowire (which can be determined from SEM imaging), T_C is the critical temperature and $\xi(0)$ is the coherence length [3, 33, 35, 39, 40]. Finally, D is close to 1 and the quantum escape temperature T_q is represented by the vertical dashed magenta line in both figure 5.1 and 5.2 and in all cases corresponds closely to the visible crossover from quantum to thermal behavior.

Standard deviation vs temperature for the four unpulsed wires (A-D) are shown together in figure 5.3 along with unpulsed wires E and F which have lower T_C. Wires E and F show the onset of thermally activated multiple phase slips which results in the reduction of standard deviation at high temperature. This figure shows the transition from the standard deviation increases with increasing temperature behavior expected of single phase slips to the standard deviation decreases with increasing temperature behavior observed in Sahu et al [23]. Fits to the standard deviation vs temperature for wires E and F corresponding to the fits for wires A-D in figure 5.1 are shown in figure 5.3.

Figures 5.4a and 5.4b shows distributions and rates for wire A. The rates are calculated from the distributions using the formula of Kurkijärvi, Fulton and Dunkelberger:

$$\Gamma(K) = \dot{I}\frac{1}{\Delta I}\ln\left(\sum_{j=1}^{K} P(j) \Big/ \sum_{i=1}^{K-1} P(i)\right) \tag{5.7}$$

where $K = 1$ corresponds to the bin with the highest switching current [46, 47]. The rates are fit using the cubic form ($b = 3/2$) of equation (5.1) with fitting parameters A and T_{esc}

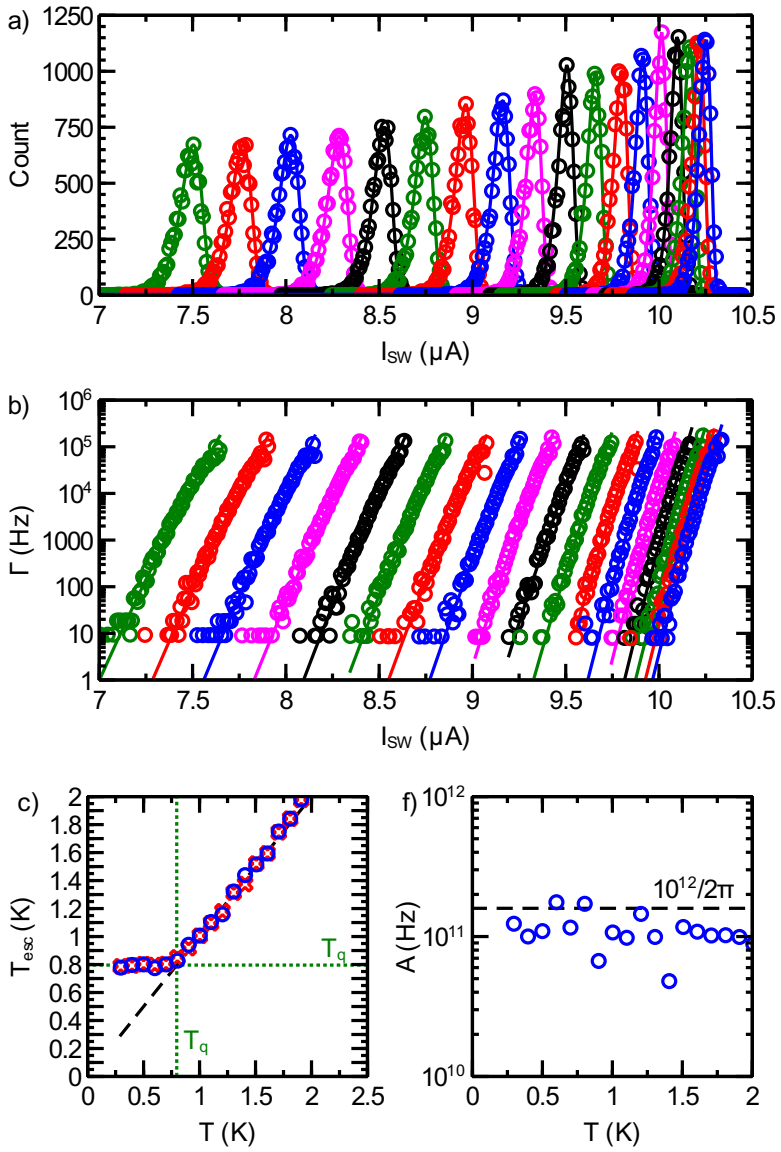

Figure 5.4: Distributions and rates for wire A. a) Measured switching current distributions shown as points with expected values from the fit to the rate using equation (5.8) shown as solid lines of the same color . b) Rates derived from the distributions shown in a using equation (5.7) represented with circles. The solid lines of the same color are fits using equation (5.1) with fitting parameters A and T_{esc} where $B = U_C/kT_{esc}$, $U_C = D\sqrt{6}\hbar I_C/2e$, $D = 1.095$ and I_C is given by equation (5.5). c) The fitting parameter T_{esc} vs temperature is shown as blue circles. The estimated T_{esc} from equation (5.2) is shown as red crosses. The black dashed line is $T_{esc} = T$. The green dotted lines are $T_q = 0.796$ from the mean and standard deviation fit (see table 5.1). d) The prefactor A vs temperature. The dashed black line is the estimate ($A = 10^{12}/2\pi$) used for the mean and standard deviation fits shown in figure 5.1.

where $B = U_C/kT_{esc}$, $U_C = D\sqrt{6}\hbar I_C/2e$, $D = 1.095$ and I_C is given by equation (5.5) and are shown as solid lines of the same color as their respective data in figure 5.4b. These fits are then transformed back into distributions using the approximation:

$$P(I) \approx \frac{\Gamma(I)}{\dot{I}} \exp\left(-\frac{\Delta I}{\dot{I}} \sum_{0}^{I} \Gamma(I)\right) \tag{5.8}$$

where $\dot{I}$ is the sweep speed [46]. The resulting distributions are shown as solid lines of the same color as their respective data in figure 5.4a. The fitting parameter T_{esc} for wire A is plotted versus temperature in figure 5.4c. For reference, the T_q from the mean and standard deviation fit shown in figures 5.1 and 5.2 is plotted on both the horizontal and vertical scales as a dotted green line . There is excellent agreement between thermal dominated escape $T_{esc} = T$ (shown by a black dashed line) above T_q and quantum escape with an effective temperature $T_{esc} = T_q$ below T_q. T_{esc} can also be estimated by combining equations (5.2) and (5.4) to yield:

$$\frac{1}{B} = \frac{kT_{esc}}{U_C} = \frac{1}{\ln X}\left(\frac{\sqrt{6}b\sigma \ln X}{I_C\pi}\right)^b \tag{5.9}$$

The estimates from equation (5.9) are plotted as red x's in figure 5.4c and correspond well with the T_{esc} arrived at by fitting the rates (shown as blue circles). The fitting parameter A for wire A is plotted versus temperature in figure 5.4d as blue circles. A compares fairly well with the estimated value of $10^{12}/2\pi$ used for the fits in figures 5.1 and 5.2 (shown by the dashed black line) though it appears this was a slight overestimate.

Figure 5.5a shows a plot of T_q vs T_C (T_q is from the mean and standard deviation fit and is listed in table 5.1). For comparison, samples S1 through S5 from Sahu et al. [23] are plotted on the same graph. There is a fair amount of overlap between the data shown here and the data from Sahu et al. except for the case of sample S5 which has a surprisingly large T_q. The line is the best fit to the data shown with blue circles. Figure 5.5b shows a plot of σ vs $d(\ln\Gamma)/dI$ for base temperature where the derivative was estimated by doing a linear fit

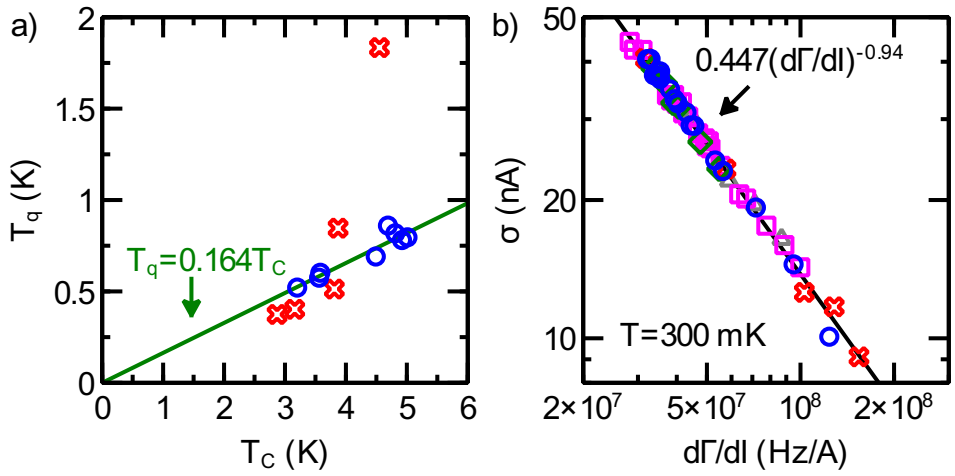

Figure 5.5: Comparison of fitting parameters a) T_q vs T_C for the wires A-F are shown as blue circles. The best linear fit to this data is shown as a green line. The fitting parameters for samples S1-S5 from Sahu et al. are shown as red crosses. Note the general dependence $T_q \propto T_C$ holds for all samples except S5. b) Standard deviation vs $d\ln\Gamma/dI$ at base temperature where the derivative is determined by a linear fit to $\ln\Gamma(I)$. The black line is the best fit to the power law shown. The blue circles are from pulsing wire A, the green diamonds are from pulsing wire B, the magenta squares are from pulsing wire C, the grey triangles are from unpulsed wires (including wires E and F) and the red crosses are from the base temperature distributions for the 5 samples (S1-S5) which appear in Sahu et al.

of $\ln\Gamma(I)$ vs I. This graph includes distributions from pulsed nanowires where temperature sweeps were not performed. The function plotted is the best fit to all data. Figure 5.6 shows a plot of σ vs $\langle I_{SW}\rangle$ for all samples including pulsed wires where temperature sweeps were not performed.

5.4 Discussion:

For multiple thermally activated phase slips, it has been theoretically predicted and experimentally observed that standard deviation decreases as temperature increases [23, 49]. A similar effect has been observed in Josephson junctions where the decrease in standard deviation with increasing temperature is described by multiple retrapping [59,60]. At sufficiently low temperatures, this thermally activated multiple phase slip model ceases to fit well with the data. In this regime, it is predicted a single phase slip will be sufficient to drive the

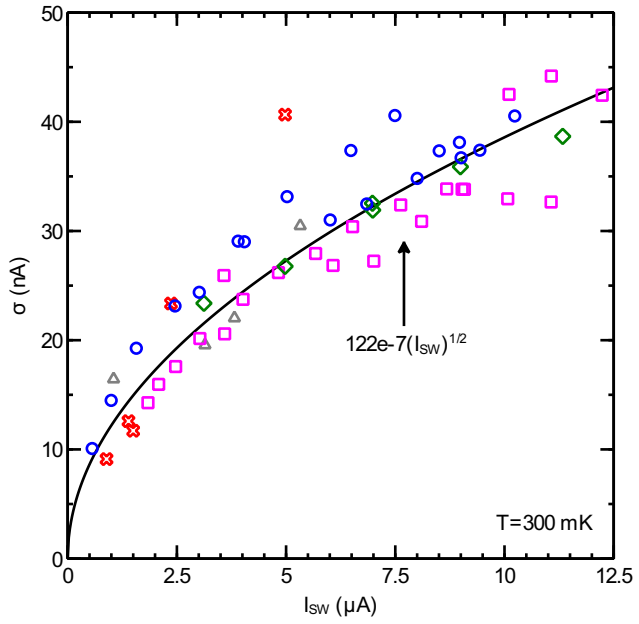

Figure 5.6: σ vs I_{SW} The general dependence that wires with larger critical temperatures typically have larger critical currents is the source of the dependence between I_{SW} and σ (since wires with larger critical temperatures will have larger T_q and thus increased σ). The data is fairly well described by a power law as shown. The blue circles are from pulsing wire A, the green diamonds are from pulsing wire B, the magenta squares are from pulsing wire C, the grey triangles are from unpulsed wires (including wires E and F) and the red crosses are from the base temperature distributions for the 5 samples (S1-S5) which appear in Sahu et al.

nanowire into a Joule heated normal state [23]. The phase slip rate in this case is virtually identical to the escape rate of a Josephson junction (JJ) yet similar behavior to the JJ model was not observed previously. We see that for unpulsed wires, $b = 3/2$ corresponding to a cubic potential more accurately describes the behavior of the wire than the $b = 5/4$ expected from LAMH theory. This is indicative that the free energy barrier for single phase slips is well approximated for a cubic though it should be noted that the barrier at zero bias current agrees well with the predictions of LAMH theory. For heavily pulsed wires, which we expect to be single crystalline Mo_3Ge [57], $b = 5/4$ provides a better fit to the data. This might be due to the increased coherence length of the single crystal form which would make the wire more in the one-dimensional limit than the amorphous MoGe nanowire. Conversely the increased coherence length would also lead to a shorter effective length of the nanowire putting the nanowire closer to the Josephson junction limit. This would explain why the zero current free energy barrier for the pulsed nanowires $\approx 0.68\sqrt{6}\hbar I_C/2e$ is a fair amount lower than the LAMH prediction for nanowires.

Wires C and D have $5\,\mu$m wide electrodes compared to the $20\,\mu$m wide electrodes for wires A and B thus we can expect them to have 4 times less capacitance (and 4 times the damping) of the wide electrode wires. For an underdamped JJ, such a decrease in capacitance would result in a factor of 2 increase in T_q since $kT_q = \hbar\omega_p/2\pi \propto (I_C/C)^{1/2}$. However, for an overdamped JJ, this expression is modified to [3, 46, 48]:

$$kT_q = \hbar\omega_p^2 RC/3\pi \propto R/L_k \tag{5.10}$$

Note the dependence on capacitance disappears. Nanowires are expected to be heavily damped with the hysteresis in the VI curves caused by Joule heating [41]. Thus it is not surprising that we observe T_q of wires C and D are comparable to wires A and B since one would not expect a dependence on the capacitance for an overdamped system such as a nanowire. From the microscopic theory of Golubev and Zaikin for nanowires [19] we have

that

$$\Delta F(0)/kT_q \propto I_{C0}/kT_q \propto R_q L/R_N \xi(0)$$

Tinkham and Lau [40] showed that

$$I_{C0} \propto \frac{LT_C}{R_N \xi(0)} \tag{5.11}$$

so we arrive at the simple relation for nanowires that

$$T_q \propto T_C \tag{5.12}$$

Equation (5.12) indicates again that it is not surprising that wires A-D have similar T_q since T_C of all four wires are fairly similar (see table 5.1).

When wires C and D are fully pulsed into the single crystal state, they recover similar switching currents to the unpulsed wires A-D yet they have R_N and T_C reduced roughly by a factor of 2. Likewise, their T_q is reduced by a factor of 2 as one would predict from the reduction of T_C using equation (5.12) or the reduction in R_N by equation (5.10) (assuming the resistive damping is dominated by the normal resistance i.e. $R = R_N$). The switching of the pulsed wires C and D is also less premature as one would expect for a more heavily damped nanowire (see figure 5.2). Wire B is about twice as long as wires A, C and D resulting it in having roughly twice the normal resistance. The overdamped JJ expression (5.10) incorrectly predicts that this wire because of its high resistance should have about twice the T_q of wires A, C, and D. However, the nanowire expression, equation (5.12) correctly predicts that T_q for wire B should be comparable to the other wires since its T_C is comparable or equivalently that R_N/L of wire B is comparable to the other nanowires. This is indicative that we are indeed measuring quantum phase slips in the nanowire and not the quantum escape of a weak link acting as a JJ. As further evidence, the various pulsed nanowires follow the same behavior as the unpulsed nanowires. Pulsing radically changes the morphology of the wire

so a weak link dominated model could be expected to perform erratically under pulsing.

Figure 5.5a shows T_q vs T_C and excellent agreement with the expected proportionality $T_q \propto T_C$ expected for nanowires. Notice that this graph is comparing the T_q arrived at from a low temperature, high bias current, sweep to the T_C found from fitting the higher temperature, low bias current, resistance vs temperature fit. The points from Sahu et al. show an agreement with this trend for all samples except sample S5. It should be noted that inserting the mean and standard deviation for the base temperature distribution of sample S5 into equation (5.9) yields a $T_q \approx 1\,\mathrm{K}$ which would put sample S5 much more in line with the other values. The slope of the best fit line implies for the Golubev Zaikin theory [19], a value for the fitting factor of order unity namely $A_Q = 0.83/0.164 = 5.06$. This is in excellent agreement with the results of Rogachev et al. where they concluded that $A_Q > 4$ would result in QPS tails being undetectable in resistance vs temperature curves for similar nanowires to ours [9].

Figure 5.5b shows σ vs $d\ln(\Gamma/dI)$ where $d\Gamma/dI$ is estimated by a linear fit to the log-linear graph of $\Gamma(I)$ at base temperature. Since $\ln(\Gamma(I))$ is nearly a straight line versus I as shown in figure 5.4, T_{esc} corresponds to this slope through the equation:

$$T_{esc} = \frac{b\sqrt{6}\hbar}{2ek(d(\ln\Gamma)/dI)}(1 - I_{SW}/I_C)^{b-1}$$

Assuming b is sufficiently close to one that the dependence on switching current is unimportant, we arrive at the relationship:

$$T_{esc} \propto \frac{1}{d(\ln\Gamma)/dI} \tag{5.13}$$

We also know that roughly:

$$\sigma \propto T_{esc}^{1/b} \tag{5.14}$$

Using equations (5.13) and (5.14), the power law fit in figure 5.5b provides the indepen-

dent estimate that in the quantum regime $b = 1/0.94 = 1.06$. This is lower than the powers used in both the cubic and LAMH fits ($b = 3/2 = 1.5$ and $b = 5/4 = 1.25$ respectively). It should be noted that the assumption that b is the same for both the thermal and quantum rates was only made to reduce the number of fitting parameters (from equation 5.4 it is fairly obvious that changing b at the crossover temperature results in two different values for $\langle I_{SW} \rangle$ at the same temperature if all other parameters are kept fixed). The value $b = 1.06$ is in excellent agreement with $b = 1$ which is the expectation for quantum tunneling from a heavily damped JJ (or any other system where the free energy can be approximated by a cubic) [46,48]. The trends in figures 5.5a and b would not occur if the enhanced escape temperature we attribute to QPS were due to noise or inhomogeneity or even mischaracterized thermal escape.

Figure 5.6 shows σ vs I_{SW}. The general trend that wires with larger critical currents typically have larger critical temperatures and thus larger T_q and σ is reflected in the data. From equation (5.11) we can expect a roughly power law dependence between I_C and T_C (assuming R_N/L is constant) since $\xi(0)$ is expected to be proportional to $T_C^{-1/2}$ (though this does not explain the $I_{SW}^{1/2}$ power observed). It should be noted that it has been experimentally observed that $\xi(0)$ appears to increase significantly more quickly than the proportionality $\xi(0) \propto T_C^{-1/2}$ would predict [57] which could explain the 1/2 power dependence observed in graph 5.6.

Chapter 6

Nano-slits in silicon chips

6.1 Introduction

[1]Potassium hydroxide (KOH) etching of a patterned $< 100 >$ oriented silicon wafer produces V- shaped etch pits. We demonstrate that the remaining thickness of silicon at the tip of the etch pit can be reduced to ≈ 5 microns using an appropriately sized etch mask and optical feedback. Starting from such an etched chip, we have developed two different routes for fabricating 100 nm scale slits that penetrate through the macroscopic silicon chip (the slits are ≈ 850 m wide at one face of the chip and gradually narrow to $\approx 100 - 200$ nm wide at the opposite face of the chip). In the first process, the etched chips are sonicated to break the thin silicon at the tip of the etch pit and then further KOH etched to form a narrow slit. In the second process, focused ion beam (FIB) milling is used to etch through the thin silicon at the tip of the etch pit. The first method has the advantage that it uses only low-resolution technology while the second method offers more control over the length and width of the slit. Our slits can be used for preparing mechanically stable, transmission electron microscope (TEM) samples compatible with electrical transport measurements or as nanostencils for depositing nanowires seamlessly connected to their contact pads.

KOH etching of a $< 100 >$ silicon wafer is anisotropic. KOH etches the $< 100 >$ and $< 110 >$ planes of single crystal silicon at a much higher rate than the $< 111 >$ plane. This creates a V-shaped etch pit bound by the $< 111 >$ crystal planes of silicon. This etching

[1]The contents of this chapter are published as: Thomas Aref, Matthew Brenner and Alexey Bezryadin *Nanotechnology* **20**, 045303 (2009)

property of silicon is commonly used for making silicon nitride membranes. Large, $\approx 100\mu$ m wide slits can be easily fabricated in bulk silicon wafers using standard photolithography and KOH wet etching [61]. Small, ≈ 100 nm wide slits can be fabricated in silicon-on-insulator (SOI) substrates [62, 63]. However, this method of nanoscale slit making cannot be directly extended to a bulk silicon wafer because it relies on the tiny thickness variation of the thin silicon layer in the SOI substrate [64]. Careful control of the KOH etching of bulk silicon wafers has allowed features in the sub-micrometer range such as silicon nanopores [65] and thin silicon membranes [66]. We demonstrate sub-micrometer slits fabricated in bulk silicon wafers using KOH etching, both with and without the assistance of focused ion beam (FIB) milling.

We observed that by carefully controlling the KOH etch of a silicon chip, the tip of the V-shaped etch pit can be brought to within $\approx 5\,\mu$m of penetrating the silicon chip. To do this, we periodically inspect the etch pit in an optical microscope with a strong back light. When the silicon is thin enough, visible light can penetrate through the thin silicon at the tip of the etch pit. Starting from a silicon chip with such an etch pit, we have developed two different processes of fabricating 100 nm scale slits that penetrate the silicon chip. In the first process, sonication breaks the thin silicon at the tip of the etch pit. Continuing the KOH from this point creates a narrow silicon nitride membrane ($\approx 100 - 200$ nm wide). Removing the silicon nitride membrane with a phosphoric acid strip creates a slit. We have produced slits down to 125 nm wide using this method. This process does not use FIB milling and the slits propagate the entire length of the etch pit. The second process uses FIB milling to etch through the thin silicon and silicon nitride at the tip of the etch pit. The first method uses only low-resolution technology while the second method offers greater control over the length and width of the slit (see figure 6.1). These slits are useful as substrates for combining electrical transport measurements and transmission electron microscope (TEM) imaging. We show TEM imaging with simultaneous in-situ measurement of a multi-walled carbon nanotube (MWNT) deposited on a sonication-induced slit. We demonstrate TEM

imaging and measurement of superconducting nanowires deposited on a FIB-milled slit. The fragile superconducting nanowires would typically not survive on a less mechanically stable TEM sample (such as slits in a silicon nitride membrane) because stress from handling of the sample or cryogenic cooling would fracture the nanowire. The slits are also useful for nanostencil lithography. A nanostencil is nanoscale shadow mask typically consisting of a silicon nitride membrane with nanoholes or nanoslits micromachined into it. Nanowires or nanoparticles can be formed when material is deposited through the nanoholes or nanoslits in the nanostencil. A variety of nanoparticles and nanowires have been formed using this method [67–71]. We show a 200 nm wide gold nanowire fabricated by nanostencil deposition through a sonication-induced slit. The flexibility of a traditional silicon nitride membrane makes it difficult to fabricate certain patterns in a nanostencil. For instance, a nanostencil for one-step deposition of a nanowire seamlessly connected to larger contact pads would require a thin slit connected to two larger holes. While this geometry would be unstable in a silicon nitride membrane nanostencil, our slits are supported by macroscopic silicon walls. We demonstrate deposition of a 330 nm wide gold nanowire seamlessly connected to its contacts using a FIB milled slit.

6.2 Experimental Details

The silicon wafers used for this paper are 3" diameter, $< 100 >$ lightly n-doped Czochralski (Cz) double side polished (DSP) silicon wafers with 100 nm of low stress, low pressure chemical vapour deposition (LPCVD) silicon nitride deposited on both sides (Surface Process Group). The wafers are $600 \pm 5\,\mu$m thick. A tight specification on thickness makes choosing the initial mask size easier. The wafers have a total thickness variation (TTV) $< 3\,\mu$m. A small TTV makes the point at which to stop the KOH etch fairly uniform across the wafer. Cleavage lines for the chips are defined by the KOH etch using a corner compensation technique to get rectangular chips [29]. Alternatively, rectangular chips can be defined by dicing

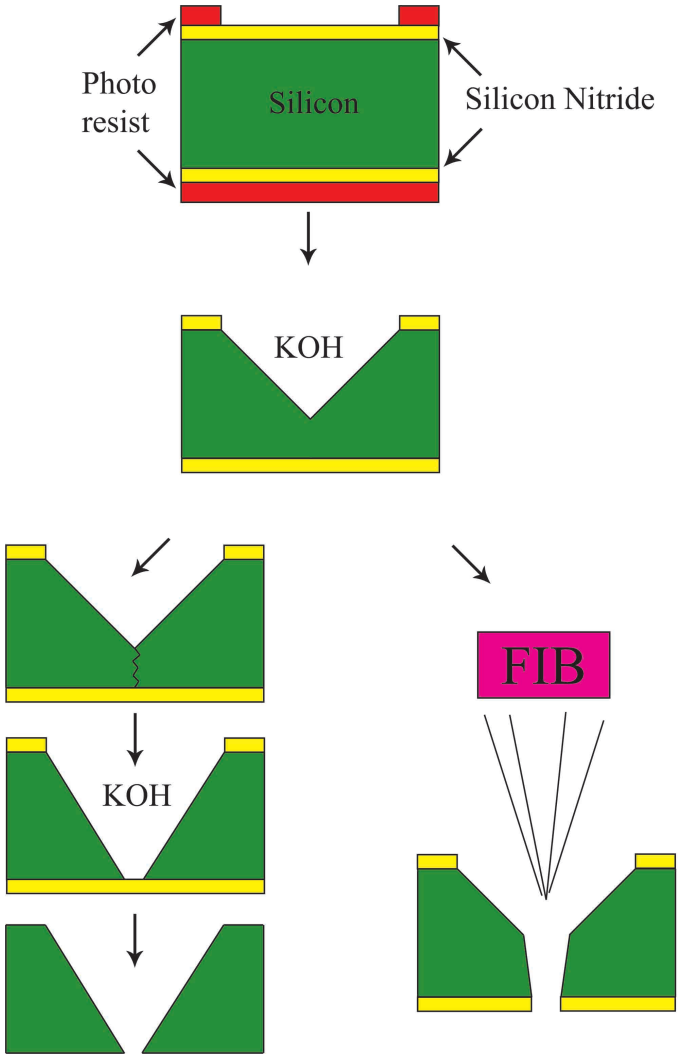

Figure 6.1: Two processes for fabricating nano-slits in macroscopic silicon chips: Starting with a silicon wafer coated with silicon nitride, photolithography followed by reactive ion etching (RIE) is used to define a hard mask in the silicon nitride. KOH etching is used to produce a V-shaped etch pit. The KOH etch is monitored using optical microscopy. When the remaining silicon at the bottom of the etch pit is thin enough, light will penetrate through when the sample is back-lit. From this point, two different fabrication routes can be followed. On the left, $\approx 100\,\text{nm}$ scale slits are produced using only low- resolution technology. The thin silicon is first cracked using brief sonication in deionized water. Further KOH etching of the crack produces a silicon nitride membrane $\approx 100 - 200\,\text{nm}$ wide. Stripping the silicon nitride produces a narrow slit. On the right, focused ion beam (FIB) milling is used to directly make $\approx 100\,\text{nm}$ scale slits through the thin silicon. This method offers more control over the length and width of the slit than the process on the left but relies on high-resolution technology.

after the KOH etch. A transparency mask (5080 dpi transparency printer) was used to define etch pits and cleavage lines using photolithography. We achieved the best accuracy in transparency masks by coding the mask directly in the postscript programming language accepted by the printer rather than using a computer assisted drawing program (CAD) and translating it to postscript. After photolithographic patterning with an appropriately sized mask, the pattern defined in the photoresist was transferred into the silicon nitride by reactive ion etching (RIE) using a CHF3/O2 plasma. The photoresist was then stripped in acetone. The wafer was placed in 70 °C KOH (45% by weight, Sigma Aldrich) to etch the silicon anisotropically. A timed etch was performed using a programmable hotplate (Torrey Pines Scientific HS40). Empirically, we found a time of 6 hours to be a satisfactory starting point. At the end of 6 hours, the hot plate automatically switches off. The actual initial etch is longer than 6 hours since etching continues as the KOH etchant cools. Because the $< 111 >$ plane etches much more slowly than the $< 100 >$ or $< 110 >$ plane, a V-shaped etch pit is produced. After the initial etch, etching is continued as before but is now monitored at periodic intervals. Every $15 - 30$ minutes, the wafer is removed from the KOH and placed in a flat polystyrene petri dish (FALCON 351007) filled with the minimum amount of deionized water needed to cover the sample. The wafers are inspected in an optical microscope with a strong back light (VWR VistaVision T-RTP). When the silicon is sufficiently thin (we estimate $\approx 5\,\mu$m from FIB cross sections), a thin red line will be visible in the optical microscope from the back light penetrating the chip. At this point, KOH etching is stopped by a rinse in deionized water, nitric acid, deionized water, and then isopropanol. The wafer is then blown dry with nitrogen gas. These red-line samples are the starting point for the various processes described. Using a wafer with a tight TTV as described, the majority of the wafer will become red-line chips at around the same time. The chips were cleaved and separated at this point before further processing was performed to minimize stress on the slit. The mask used was designed by calculating the width of the mask required to just etch through the wafer. Using simple trigonometry, it can be derived (from the angle the etch

pit makes relative to the surface of the chip, $\tan^{-1}\sqrt{2} \approx 54.7$) that this width follows the formula $w = h\sqrt{2}$ where h is the thickness of the wafer and w is the width of the mask required to just etch through the wafer. For a $600\,\mu$m thick wafer, the width of the mask should be $600 \times \sqrt{2} \approx 849\,\mu$m. The variation in wafer thickness of $\pm 5\,\mu$m implies the mask width should be between $595 \times 2 \approx 841\,\mu$m and $605 \times 2 \approx 855\,\mu$m. Because we manually align to the flat of the wafer, we get some undercut from the etch so an undersized mask was used. If we use only one size mask, the etching time can vary by several hours just from the variation in thickness between separate wafers. Therefore, we performed a test etch with varying size etch pits on a small piece of the wafer. The test mask had etch pits ranging from $790 - 830\,\mu$m in $5\,\mu$m increments. The test mask and corresponding wafer sized masks can all be included on a single transparency. We have also tried this fabrication process on wafers with a much larger uncertainty in thickness ($\pm 25\mu$m). The large variation in thickness made it more difficult to choose an appropriate sized photomask. We had to use a significantly under sized mask and use long etching times. If the photomask used is significantly undersized, the KOH etch cannot be completed in a reasonable amount of time (several hours). In this case, tetramethylammonium hydroxide (TMAH) (Sigma Aldrich) etch was used since it etches the $< 111 >$ plane of silicon more quickly than KOH. In this case, we did an etch of TMAH for three hours and KOH etch for one hour until we reached a red-line state. However, with more uniform wafers, a properly sized mask and a test mask, this step was unnecessary. Wafers with less tight TTVs tended to reach the red-line state at different etching times across the wafer. This required stopping the etch when some of the samples were ready, separating out samples that were not ready and continuing the etch independently for each samples that did not yet have light penetrating it when back lit. Using a wafer with TTV$< 3\,\mu$m had most of the wafer reach the red line state at roughly the same time and allowed stopping of the etch on the entire wafer simultaneously. Once a red-line chip is formed, we can fabricate ≈ 100 nm scale slits in it using only sonication and wet etching. A red-line chip is briefly (less than 1 second) sonicated in deionized water.

This sonication breaks the silicon along the thinnest point, which is the tip of the V-shaped etch pit. The silicon nitride on top of the silicon does not typically break. The chip is then etched in 70 °C KOH for $1 - 5$ min. Every 30 seconds, the chip is removed from the KOH, placed in a petri dish with the minimum amount of DI water needed to cover the chip and examined under an optical microscope. When the slit appears to have etched to an appropriate size, the chip is cleaned in nitric acid, deionized water, isopropanol and then blown dry with nitrogen gas. Once dry, the chip is inspected under the optical microscope again. Although the optical microscope is inherently inaccurate at this small scale, we have produced slits down to 125 nm wide (see figure 6.3). The inaccuracy of the optical microscopy feedback and sizing by eye produces a spread in slit sizes of ≈ 100 nm amongst different chips. A more accurate form of feedback than the optical microscope should allow smaller slits and a smaller spread in slit size. The silicon nitride typically survives to form a membrane across the narrow silicon slit. To form an actual slit, the silicon nitride is stripped in 115 °C phosphoric acid for 40 minutes. A few isolated sections of the slit are unusable from damage done by the sonication step but the majority of the slit is a usable, uniform $\approx 100 - 200$ nm slit. Without the sonication step, the Cz silicon does not open up into a uniform slit. We have also tried this fabrication process with float zone (Fz) silicon wafers with LPCVD silicon nitride on both sides (SVMI). Fz wafers can be opened up into a slit on the order of 100 nm wide without the sonication step described for Cz silicon. This is because Fz crystal is intrinsically more pure than Cz crystal because of oxygen absorbed during formation of Cz silicon. However, Fz crystal is also intrinsically more fragile than Cz crystal. Thus slits formed in Fz silicon often had cracks running parallel to the slit, making them unusable (see figure 6.2). Slits formed in Cz silicon rarely display cracks. However, Cz samples do not open into a 100 nm scale slits from KOH etching alone but typically form a triangular shape slit propagating from one end of the etch pit. This triangular shape was avoided by introducing the sonication step described. These sonication-induced slits can be used as nanostencils. We inverted a 125 nm slit onto a silicon nitride membrane and

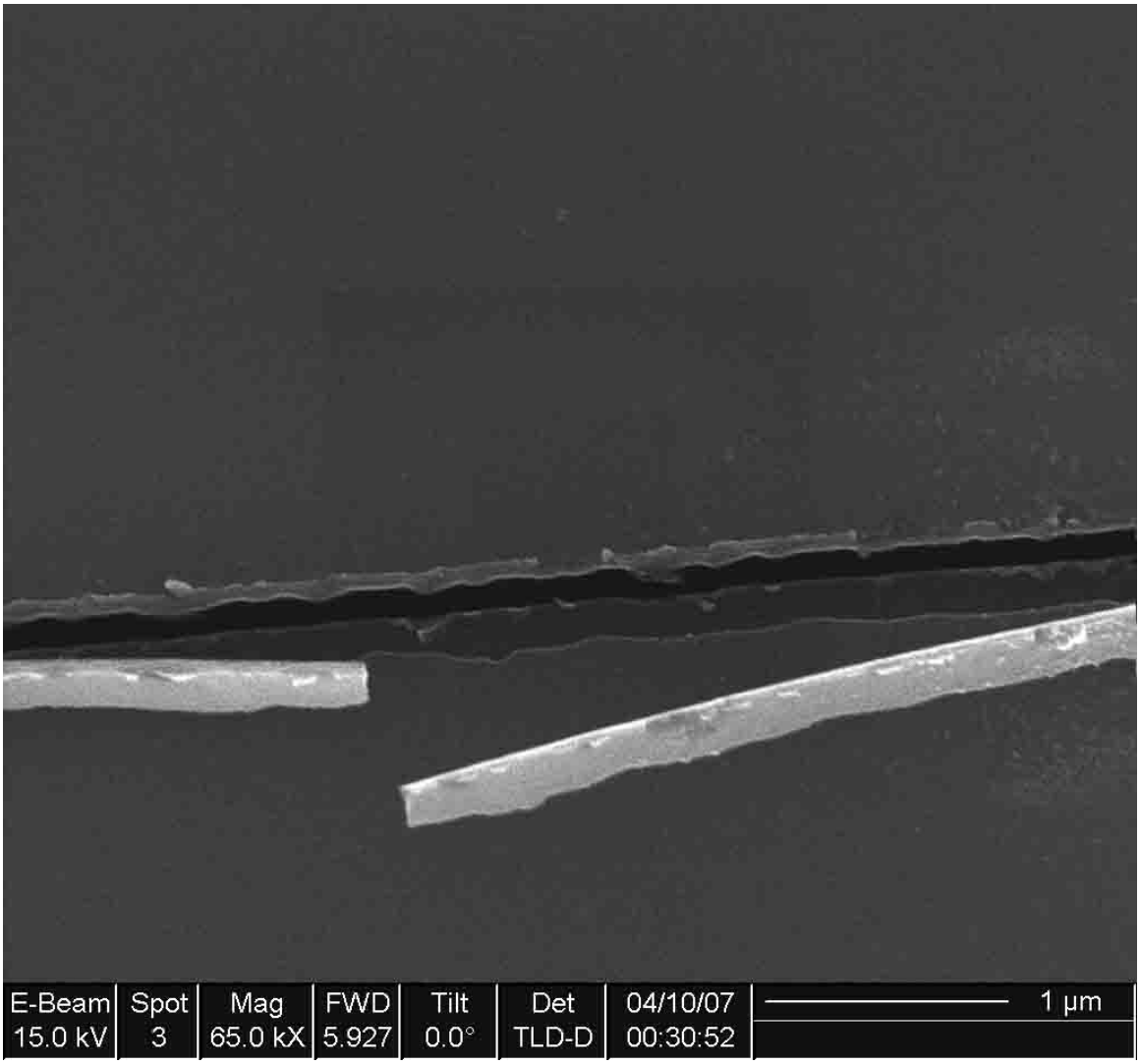

Figure 6.2: A crack in a slit formed in fragile Fz silicon. A thin piece of silicon has cracked parallel to the slit and broken off destroying the slit.

deposited 5 nm of titanium and 30 nm of gold using e-beam evaporation. This resulted in a 200 nm wide nanowire (see figure 6.3). The nanowires larger width compared to the slit indicates that conformal contact between the slit and the substrate were not made. The conditions for nanostencil deposition were not optimized.

We also use these sonication-induced slits to perform simultaneous TEM imaging and in-situ electrical transport measurement on individual multi-walled carbon nanotubes (MWNTs). After the silicon nitride is stripped from the silicon chip, thermal oxide is grown on the silicon for electrical insulation. The slit was shadow masked with strips of polydimethylsiloxane

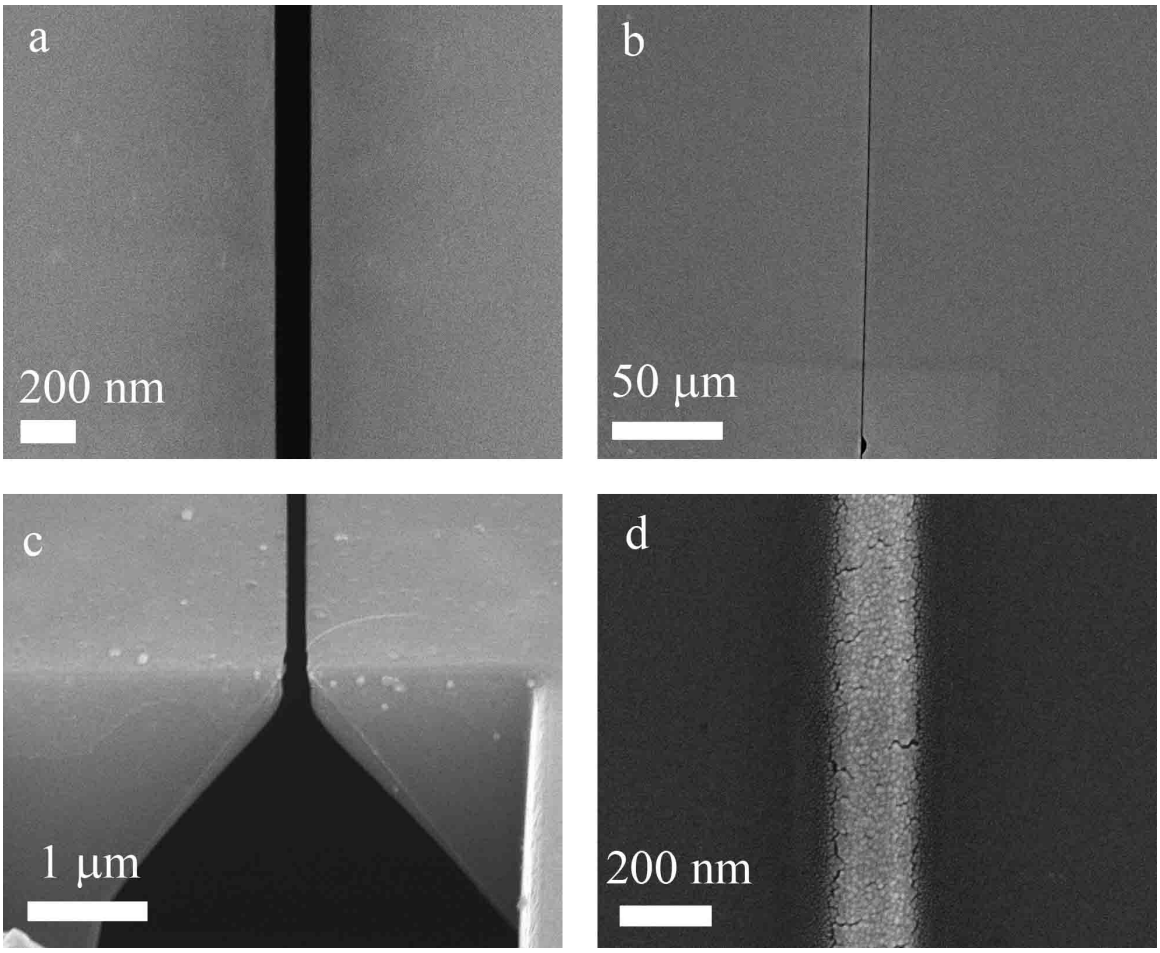

Figure 6.3: a) Close-up of 125 nm slit formed using only transparency mask photolithography, sonication and wet-etching b) the slit shown in (a) remains 125 nm for over 100 μm. A small, isolated damaged region can be seen at the bottom of the micrograph c) a cross section milled by the FIB of a slit formed by photolithography, sonication and wet etching. d) A 200 nm nanowire formed by nanostencil deposition through a slit formed using only photolithography, sonication and wet etching.

(PDMS, Sylgard 184). To form electrodes, 5 nm of Ti and 30 nm of gold were evaporated onto the slit at 5×10^{-6} Torr. Slits for transport measurements were purposefully made larger than 100 nm because the thermal oxide growth and subsequent deposition of metal reduce the width of the final slit. MWNTs were applied by crushing MWNT powder between two pieces of PDMS and then applying the PDMS to the slit [30, 31]. Unwanted nanotubes and debris crossing the slit were removed using FIB milling. Care was taken so the nanotube to be measured was not exposed to the ion beam. The sample was mounted in a specially designed TEM specimen holder that allows electrical contact to the sample in situ [32]. Electrical transport measurements and simultaneous TEM imaging were performed (see figure 6.4).

For the most mechanically stable TEM compatible samples that can also be used for transport measurements, slits are cut in the red-line chips using a FIB. FIB milling takes place from the etch pit side. Because the thickness control of the thinnest point is only feedback by eye from an optical microscope, the time needed to cut through the silicon must be varied. Initial ion currents used are $1000 - 3000/$,pA. Milling times were $1 - 10$ minutes for a 40 μm long slit. We determined the appropriate etching time by cutting a cross section that showed whether a given FIB cut penetrated or not. When an FIB cut is close to being through, the ion current can be reduced to $100 - 300$ pA for the final cut. Alternatively, an ion detector beneath the sample would allow in situ determination of the breakthrough point. Slits down to $\approx 150 - 200$ nm wide can routinely be fabricated. The slits formed are very stable by nature of their construction (see figure 6.5).

We formed superconducting nanowires across FIB-milled slits using molecular templating [20]. Carbon nanotubes are deposited across the slit and superconducting metal is deposited on them by a DC sputtering process. FIB milling is used to remove extra nanowires and separate the two electrodes defined by the slit. Alternatively, photolithography followed by wet etching can be used to remove the extra nanowires and define the electrodes. Care is taken so the nanowire to be measured is not exposed to the ion beam. The resistance versus

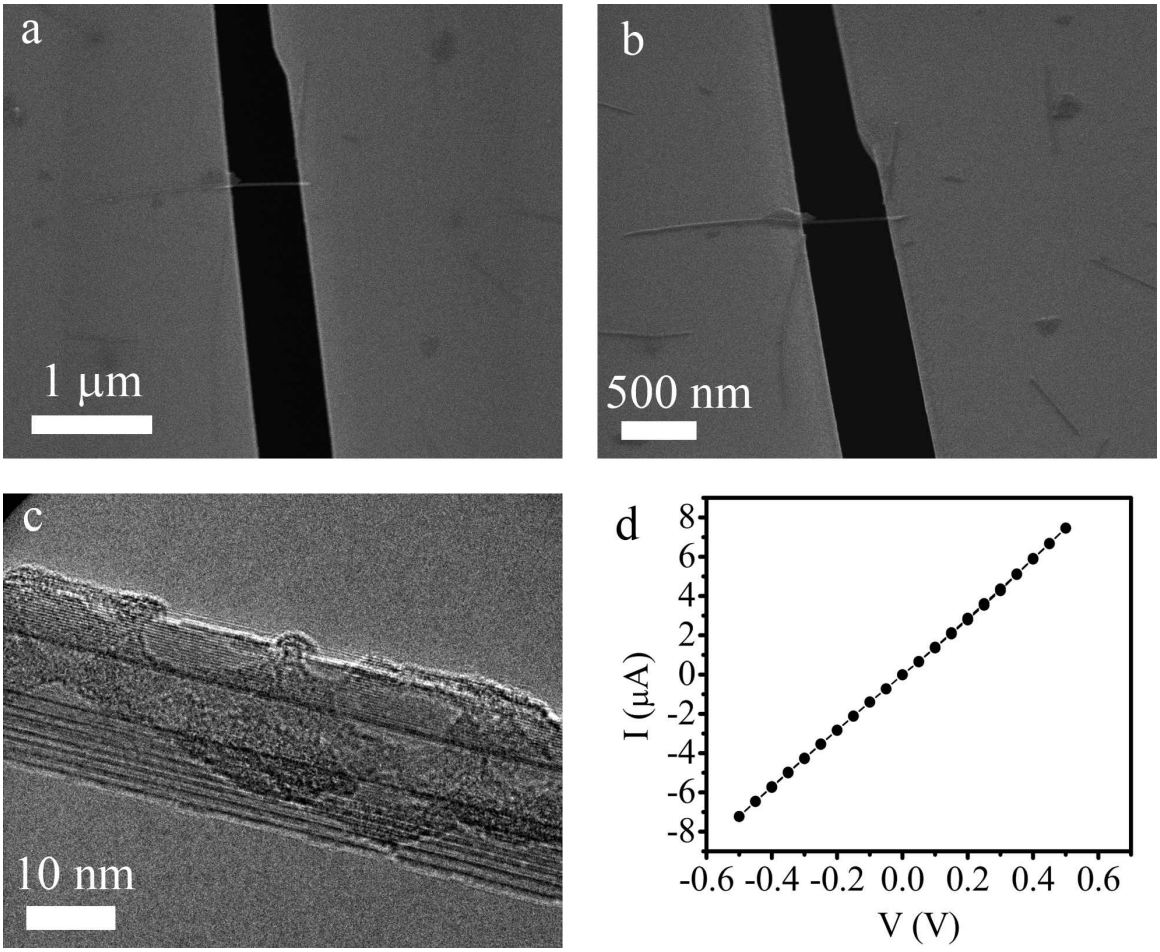

Figure 6.4: a) A scanning electron microscope (SEM) micrograph of a multi-walled carbon nanotube (MWNT) suspended across a TEM compatible slit made only with transparency mask photolithography, sonication and wet etching. The sample was oxidized and gold electrodes were deposited before the nanotube was deposited, so a transport measurement could be made. b) An SEM micrograph of the same MWNT shown in (a) taken at 52o tilt. c) A TEM micrograph of the MWNT shown in (a) d) Current vs. voltage graph for the nanotube shown in (a) measured in situ in the TEM.

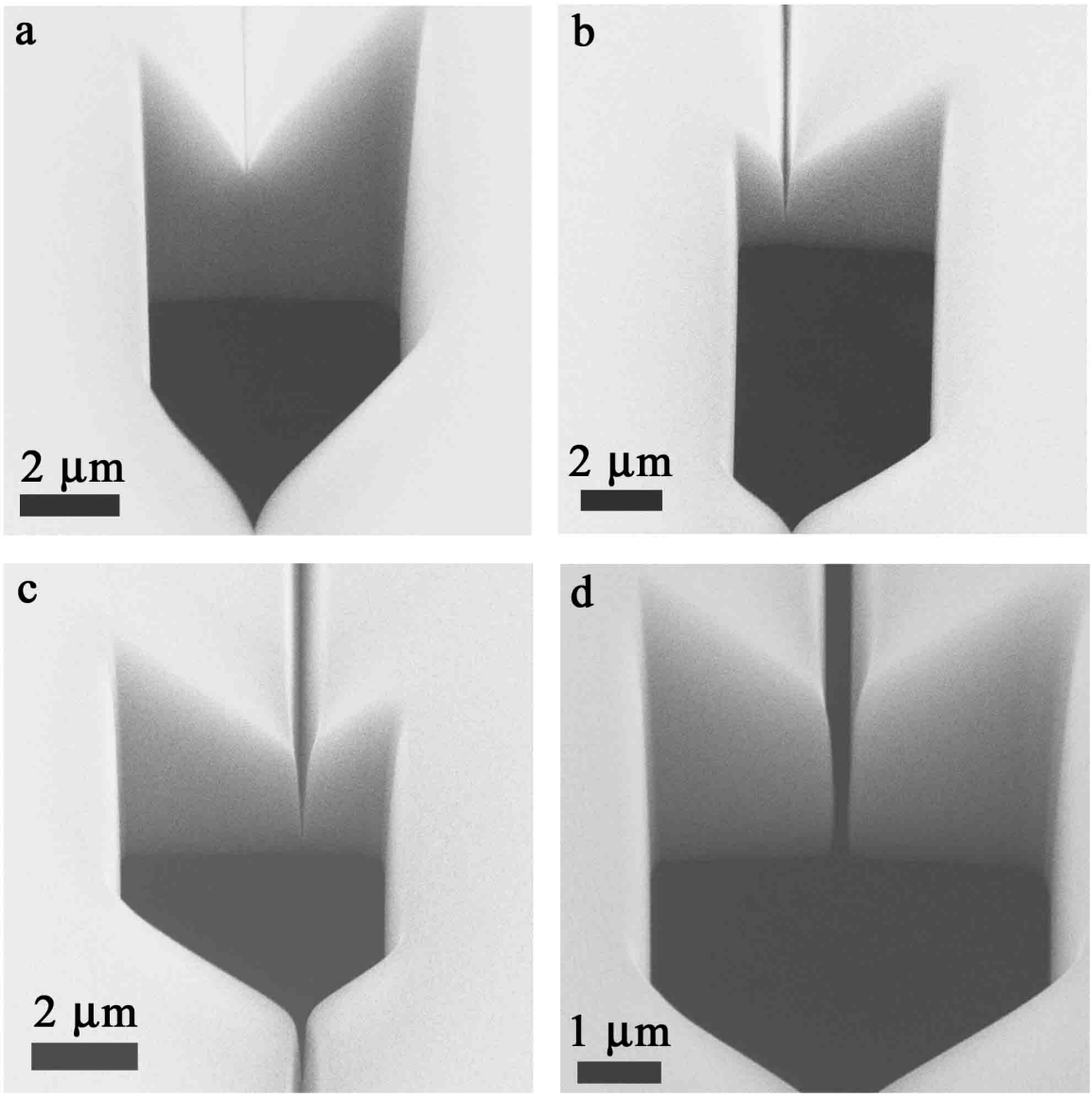

Figure 6.5: a) SEM image of an FIB milled cross section of the etch pit side of an unmodified red-line chip viewed at 52° tilt b) after 30 seconds of etching a 30 μm long slit with an FIB beam of 3000 pA from the etch pit side viewed at 30° tilt c) after 45 seconds of etching a 30 μm long slit with an FIB beam of 3000 pA from the etch pit side viewed at 30° tilt d) after 60 seconds of etching a 30 μm long slit with an FIB beam 3000 pA from the etch pit side viewed at 30° tilt. The slit penetrates the silicon and is 200 nm wide. The slits and cross-sections shown in a-d were etched on different portions of the same sample. The slit was cut before the cross-section was cut.

temperature curve of the nanowire formed on this type of slit shows the same behaviour as superconducting nanowires formed on more conventional non-TEM compatible trenches (see figure 6.6) [8, 20, 72]. Resistance versus temperature measurements on superconducting nanowires fabricated on less stable TEM compatible slits did not show the same behaviour or even go superconducting, typically because of cracks in the nanowire. Sonication induced slits were not sufficiently mechanically stable for superconducting nanowires because the slit propagates the entire length of the etch pit (1 mm). FIB milled slits are much more mechanically stable because the slit can be made shorter than the length of the etch pit and the supporting silicon near the edge of the slit is significantly thicker ($\approx 5\mu$m thick for FIB milled slits compared to a few hundred nanometres for the sonication induced slits). We observed that superconducting nanowires formed on slits 100μm or longer routinely showed cracks in the nanowire (see figure 6.7. Nanowires on slits 40μm long or shorter showed similar behaviour to nanowires fabricated on more conventional non-TEM compatible samples. Cooling the sample slowly (by not including exchange gas) helped ensure the nanowire survived the resistance versus temperature measurement. We had difficulty routinely depositing SWNTs that lay fully on top the slits by solution deposition. SWNTs that did not lie fully on top of the slit showed signs of bad contacts (visible by SEM imaging) between the wire and the contact pad after metal was deposited on them. Using the PDMS deposition method described, we can routinely deposit MWNTs but not SWNTs that are fully on top of the slits. Superconducting nanowires fabricated on MWNTs on our TEM slits showed the same behaviour as superconducting nanowires fabricated on MWNTs on regular non-TEM compatible trenches. Superconducting nanowires fabricated on MWNTs typically have multiple transitions as they go superconducting, unlike the superconducting nanowires fabricated on SWNTs, because MWNTs have a larger diameter than SWNTs thus affecting the geometry of the nanowire.

For use as nanostencils for nanowires with seamless connected contact pads, FIB milling in a different pattern was used. A red-line chip was fabricated as described above. At the tip

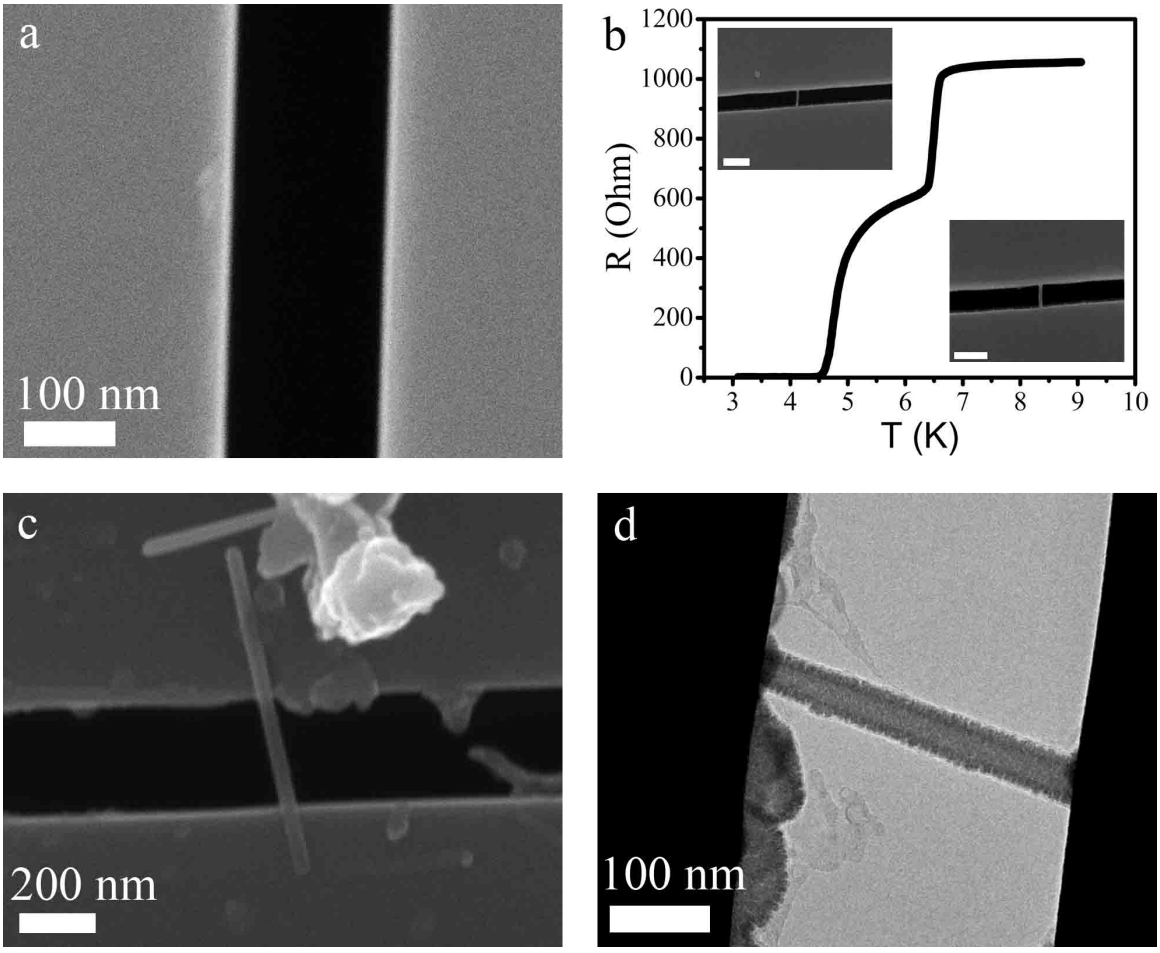

Figure 6.6: a) SEM image of a TEM compatible 165 nm wide slit made by FIB milling from the etch pit side. The image is taken from the front side i.e. the side opposite the etch pit side. The SEM image was taken in a FEI Dual-Beam 235 FIB. b) Resistance versus temperature measurement of two MoGe nanowires suspended on a TEM compatible slit made by FIB milling. The nanowires superconducting transition is similar to wires prepared on conventional non-TEM compatible trenches indicating the stability of the slits. The insets show the two wires. The wires are formed by coating a single walled carbon nanotube (SWNT) with MoGe. c) A MoGe coated multi-walled nanotube (MWNT) spanning a FIB milled TEM compatible slit. d) The same MoGe coated nanotube as in (c) imaged in 2010F JEOL TEM.

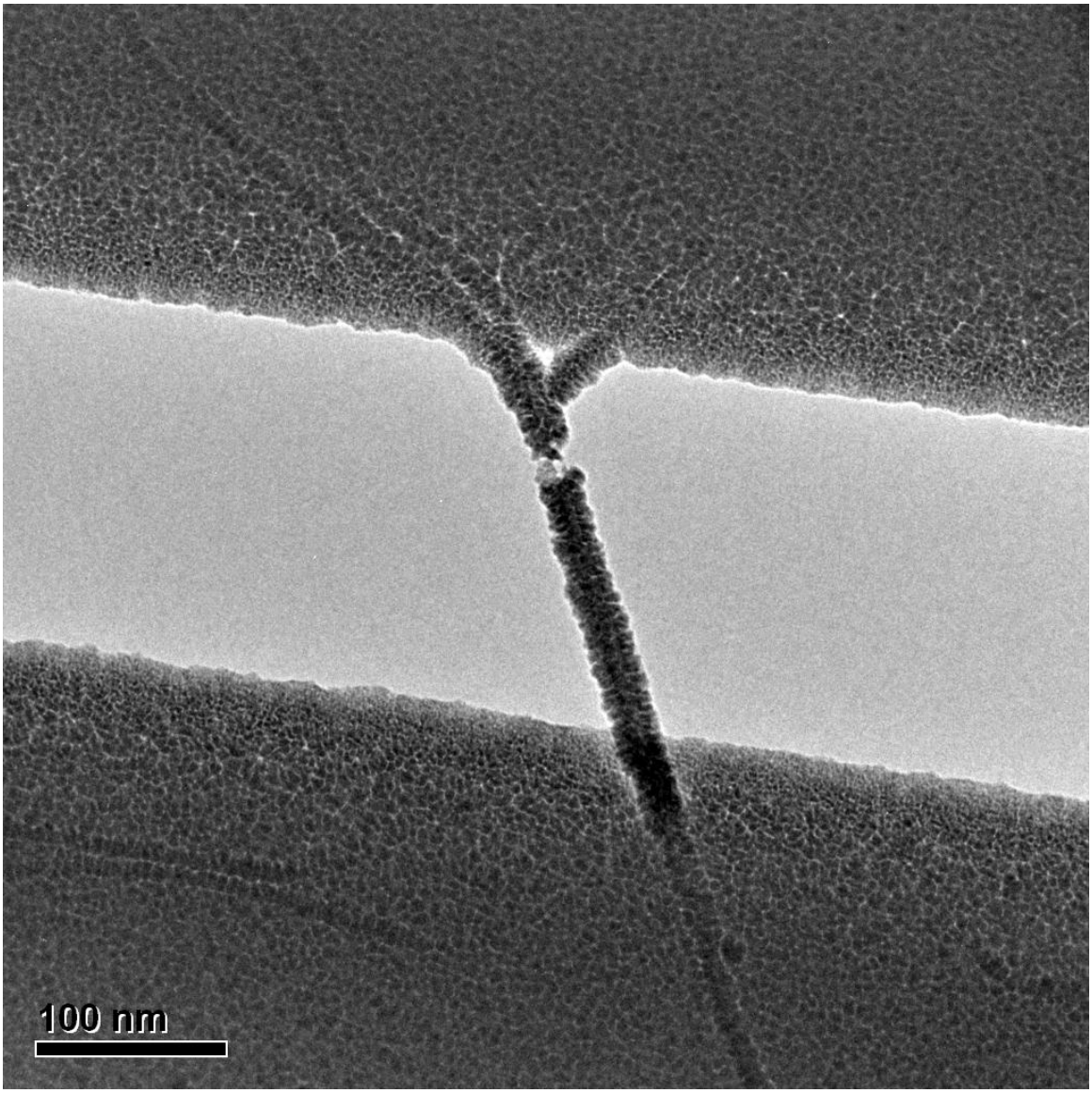

Figure 6.7: a) TEM image of a cracked nanowire formed by depositing metal on a SWNT on a less stable, 1 mm long TEM compatible slit. b) A SEM image of a cracked nanowire formed by covering a MWNT in MoGe on a 100 μm long FIB milled TEM compatible slit after a cryogenic measurement where the wire did not go superconducting. A crack in the wire is discernible at the left edge of the slit. Nanowires fabricated on slits 100 μm or longer often display these cracks. This was true for nanowires fabricated on both SWNTs and MWNTs.

of the V- shaped etch pit, a few 10 μm by 10 μm holes piercing the silicon were cut from the etch pit side. The chip was then flipped over and FIB etching proceeded from the front. The holes cut from the etch pit side aided in locating the thin silicon at the tip of the V-shaped etch pit when imaging from the front side. An area was selected above the etch pit and scanned with an ion beam of 5000 pA. The area scanned gradually etches down until the thinnest section breaks through. Breakthrough occurred at the edge of the area scanned. At this point, the ion current was reduced to 500 pA and scanning proceeded until a slit was visible. This created a recessed slit ($\approx 5\mu$m from the surface). A slit 200 nm wide was fabricated using this method. Larger contact pad slits were cut at a lower magnification and higher ion current taking care not to damage the nanowire slit. After the nanostencil was fabricated, it was removed from the FIB and placed face down on a silicon nitride membrane. 5 nm of Ti and 30 nm of Au were evaporated at 5×10^{-6} Torr. The 200 nm nanostencil formed a 330 nm wide nanowire seamlessly connected to 5 μm wide contact pads (see figure 6.8). The nanowire is wider than the slit because the slit is recessed from the surface. FIB milling from the etch pit side would allow the nanostencil to be in closer contact with the surface reducing the increase in pattern size. We chose to etch from the front side to reduce the thickness of the silicon supporting the nanostencil to minimize potential clogging. No attempt was made to optimize the conditions for nanostencil deposition. Because of the unique design of the silicon supporting the nanostencil, the nanowire connected contact pads could be fabricated in a one step deposition process.

6.3 Discussion

Transparency photomasks are a relatively inexpensive and simple way to make microscale features. They typically have a minimum resolution of $\approx 5 - 10$
$, mu$m. Using only transparency mask photolithography, sonication and wet etching, we have made $\approx$ 100 nm slits in silicon. We have demonstrated these slits can be used either for TEM

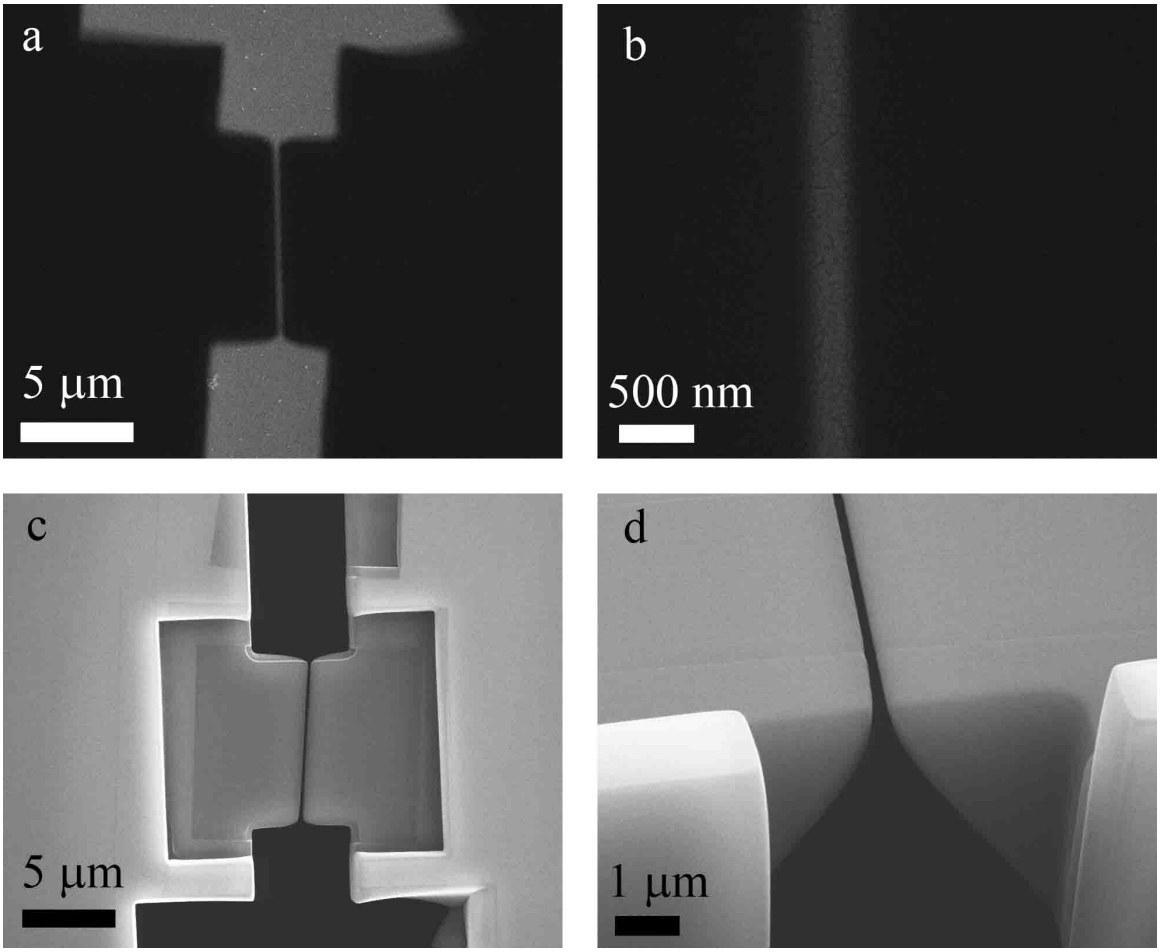

Figure 6.8: a) 330 nm nanowire with seamless contact pads fabricated in one nanostencil deposition step b) Close-up of the 330 nm nanowire shown in (a) c) The nanostencil used to make the nanowire shown in (a) and (b). The nanostencil was fabricated by FIB milling from the front side. The nanostencil consists of a narrow slit connected to two larger holes. When metal is evaporated through the nanostencil, a nanowire seamlessly connected to contact pads is formed. d) Cross section of the nanostencil shown in (c). The sloped design makes this nanostencil more mechanically stable than one cut in a silicon nitride membrane.

samples compatible with electrical transport measurements or nanostencil lithography. This relates to other methods in which conventional microfabrication techniques are pushed into the nanoscale using unconventional approaches. For example, in phase-mask photolithography [73, 74], micron scale photolithography is extended down into the nanoscale by the destructive interference of light. In step edge lithography, micron scale photolithography is used to fabricate nanoscale wires [75, 76] along the edge of a smooth step by a combination of anisotropic deposition and anisotropic etching A variety of transmission electron microscope (TEM) compatible grids such as carbon, metal and silicon nitride membrane window grids exist. However, the majority of these samples are not compatible with both imaging in a TEM and performing electrical transport measurements, either simultaneously in- situ or after imaging ex-situ. At the same time, a strong interest in combining transport measurements with TEM imaging exists [77–80]. There is no obvious way to perform transport measurements on a sample deposited on a standard TEM carbon or metal grid. Silicon nitride membrane window grids can be adapted to allow transport measurements in at least two ways. First, slits can be formed (e.g. by focused ion beam milling) in the silicon nitride and the sample and electrodes can be deposited on the slit [81, 82]. The slit both suspends the sample for TEM imaging and separates the electrodes for transport measurements. However, making a slit through a thin membrane in this manner compromises the mechanical stability of the already flexible membrane. An alternate possibility is to make connections on top of the membrane (e.g. by electron beam lithography) and perform TEM imaging of the sample directly through the underlying membrane. This results in a significant loss in resolution of the TEM image due to the membrane present underneath the specimen. Although successful measurements have been made, the membranes themselves tend to be quite fragile and prone to breaking. The flexibility of the membrane can lead to poor contacts to the nano-object being measured, affecting the transport measurement. A more rigid TEM substrate can be made by using a thicker membrane such as a silicon-on-insulator (SOI) membrane. In this thicker membrane, a slit can be etched, for example,

by deep reactive ion etching (DRIE) [80, 83]. However, the large thickness of the silicon typically limits the slit width to $\approx 1\,\mu$m or more (assuming a 10:1 aspect ratio in a $10\,\mu$m thick membrane). Slits formed in SOI membranes by KOH etching are difficult to adapt for nanostencil lithography or TEM samples compatible with transport measurements because of the geometry of the samples [62–64]. While it may be possible to balance membrane thickness with small slit size, even a thicker membrane might still be too flexible to form high quality contacts to the nano-object being measured. An ideal TEM support compatible with transport measurements would be a long ($10\,\mu$m or greater), narrow ($\approx 100\,$nm) slit that quickly broadens out to a thicker support for improved mechanical stability. Our etched chips approximate this ideal. The sonication induced slits allow us to easily measure and simultaneously TEM image a MWNT deposited on the slit. The FIB milled slits are stable enough to allow TEM imaging and subsequent cryogenic measurement of fragile superconducting nanowires. Nanowires have been formed by nanostencil lithography before, primarily using slits in silicon nitride membranes [68–71]. However if one wishes to contact such a nanowire for electrical transport measurements, further fabrication steps are required to form contacts. The most obvious way to form contacts is by drilling larger holes in the silicon nitride membrane contacting the narrow slit. On a silicon nitride membrane, the flexibility of the membrane would affect the fidelity of the deposited nanostructure. Methods to improve the fidelity of silicon nitride membranes when tackling complex geometries have been described, by placing corrugated supports on the silicon nitride membranes [84]. Our slits are supported by a silicon chip so a nanostencil nanowire with seamless contacts can be deposited in a one step process.

6.4 Conclusion

We have fabricated macroscopic silicon chips penetrated by 100 nm scale slits. We have demonstrated two methods for making these slits, one using only microscale processing

equipment and the other using FIB milling. We have demonstrated these slits have a variety of applications such as fabricating TEM compatible samples that are also compatible with electrical transport measurements and nanostencil deposition of nanowires seamlessly connected to contact pads.

Chapter 7

Modifying nanostructures with highly focused electron beams

[1]A highly focused electron beam can be used to shape nanodevices. We demonstrate electron beam etching of nanoholes through multiwalled carbon nanotubes, MWNTs and niobium nanowires. Nanoholes, as small as 2.5 nm in diameter, can be reproducibly fabricated. This technique can also be used to fabricate constrictions and larger nanoholes in MWNTs. We argue that with some improvement, this technique might be used to pattern suspended graphene by the removal of targeted single atoms.

7.1 Introduction

The ultimate goal of nanotechnology is to make structures and devices with atomic precision. One method for fabricating atomic structures, such as quantum corrals, is based on a scanning tunneling microscope [85, 86]. This approach is very powerful but is not typically used to fabricate electronic devices. Here we propose a different approach, one which might in the future be developed into a technique for fabrication of electronic devices with atomic precision. This approach is the electron-beam expulsion of single atoms (EBESA) from nanoscale objects such as carbon nanotubes, graphene layers, and metallic nanowires . The most interesting target for EBESA would be graphene, which is a stable monoatomic layer of carbon atoms. It was recently shown that it is possible to produce atomically thin graphene, i.e., isolated graphite layers [87]. Graphene is an ideal choice for single atom manipulation due to its exotic Dirac electronic spectrum. In particular, this spectrum explains the dependence

[1]The contents of this chapter are published as: Thomas Aref, Mikas Remeika, and Alexey Bezryadin*Journal of Applied Physics* **104**, 024312 (2008)

of the metallicity of carbon nanotubes on their crystal orientation. [88] In graphene, the electronic properties of the Dirac electrons are extremely sensitive to boundary conditions on the atomic scale [89]. By controlling the geometry, one expects that various transistors and switches can be fabricated from graphene if it is properly shaped [90]. Tunable nonlinear devices, such as a signal multiplier, might be fabricated from a graphene nanoribbon with perfect edges [91]. Atomically perfect ribbons may find further applications in spintronics [92, 93] and in quantum information processing [94]. Although graphene is naturally a zero-gap semiconductor, the inducement of an energy gap has already been demonstrated for epitaxially grown graphene on a SiC substrate [95]. This indicates that atomic manipulation of samples on a suitable substrate, such as SiC, could lead to semiconductor devices. The ability to introduce atomic defects [96] into a graphene layer is also of fundamental interest for connecting electron transport measurements with relativistic Dirac scattering [91]. A schematic representation of EBESA, as applied to graphene, is shown in figure 7.1. Here, the circles represent the atoms of graphene. They form the well-known honeycomb lattice. The electronic beam red is focused on individual single atoms and is expelling the targeted atoms thereby forming cuts in the graphene layer with atomic precision. In the example of figure 7.1, a schematic tripod device is being fabricated, with three graphene strips coming together at a single hexagon black . The actual geometry of a working device might be different from this example. We show a high resolution although not yet atomic resolution nanofabrication with the help of a high energy, highly focused electron beam. This method was not directly applied to graphene as fabricating transmission electron microscope TEM compatible suspended graphene samples is an arduous, although not impossible, task [97]. Instead, we applied this method to multiwalled carbon nanotubes MWNTs , which are composed of a number of rolled-up graphene layers. We demonstrate etching of nanoholes with diameters as small as 2.5 nm in carbon nanotubes (see figure 7.2). We also fabricated larger nanoholes, as large as 11 nm in a 26 nm diameter nanotube, and constrictions in a nanotube (see figure 7.3). In addition, we etched nanoholes with diameters as small as 2.5 nm in nio-

bium nanowires (see figure 7.4). This work is a continuation of our previous effort to locally modify nanowires with an electron beam [50]. We describe the details of the fabrication and consider possible applications of this method. The level of precision in removal of material with a TEM beam required for EBESA has not yet been achieved. Previously, pores, wires, constrictions, and other structures have been fabricated with a TEM using a similar method. Direct etching of resists by a focused electron beam has been explored [98, 99] Nanopores in silicon nitride and silicon oxide membranes have been fabricated [100, 101]. Constrictions in niobium have also been made [50]. Gold nanogaps have also been fabricated [102]. Wires, constrictions, loops, and other structures were recently reported [103, 104]. Nanoholes in carbon and various other materials have also been reported [105]. Exposure of carbon nanotubes to uniform electron beams have been extensively investigated and effects such as bonding [106], etching [107–109], and amorphization [110] have been seen. Focused electron beams have been used to cut bundles of SWNTs [111]. A focused electron beam was also used to etch a single wall of a MWNT [112] and to create dislocations in SWNTs [113]. Cuts have been etched in boron nitride nanotubes as well [114].

7.2 Experiment

We etched nanoholes in both MWNTs deposited directly on TEM compatible i.e., transparent to the electron beam membranes and MWNTs suspended across slits. We used low stress silicon nitride membranes (SPI Supplies, Inc.) which were 100 by 100 nm^2 and 100 nm thick. The silicon frame supporting the membrane was 3 by 3 mm^2 and 200 μ m thick to fit into a standard TEM holder or a hot stage. Using potassium hydroxide KOH etching, we also fabricated our own 50 nm thick membranes in a 5 by 8 mm^2 and 400 μm thick silicon frame. We built a custom TEM holder to accommodate our membranes. Arc discharge MWNTs (Alfa Aesar) were deposited by crushing the soot powder containing the MWNTs between two pieces of polydimethylsiloxane (PDMS Sylgard 184, Dow Corning), thus dispersing the

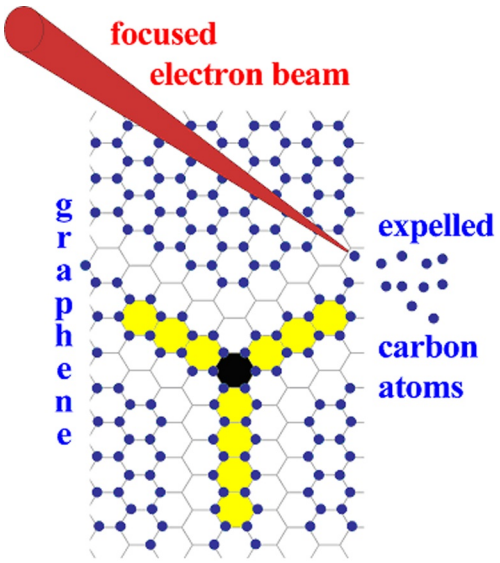

Figure 7.1: Schematic drawing illustrating the idea of atomic scale nanofabrication with EBESA. The process is illustrated with a graphene layer, which is a monolayer of carbon atoms in a hexagonal lattice. The electron beam, focused into a spot of a size smaller than the distance between the atoms, is used to expel unwanted atoms from the graphene layer. By this approach, nanofabrication with atomic resolution might be achieved. The drawing illustrates a hypothetical tripod electronic device yellow and black . The exact shape of the device can be tailored to the desired function of the device.

nanotubes. Touching and removing the nanotube covered PDMS to the membrane or slit transferred nanotubes to the sample [30]. This ensured that the nanotubes were only on one side of the membrane facing away from the TEM beam when the sample was inserted into the TEM. Because the silicon nitride is electron transparent, the nanotube is visible (see figure 7.5). The main disadvantage of placing the nanotube directly on the silicon nitride is the loss of detail from the amorphous silicon nitride obscuring the nanotube. Suspending nanotubes across an open slit in a substrate improves the resolution of the TEM images (see figure 7.2 or 7.3). 200 nm by 1 μm wide slits were formed by making cuts with a focused ion beam FIB machine starting on the membrane and ending on the silicon support chip. The increased thickness of the silicon support provided more rigidity than slits cut directly in the membrane but limited the length of slits to 3 μm.

We also etched nanoholes in metallic nanowires (see figure 7.4) . The fabrication of

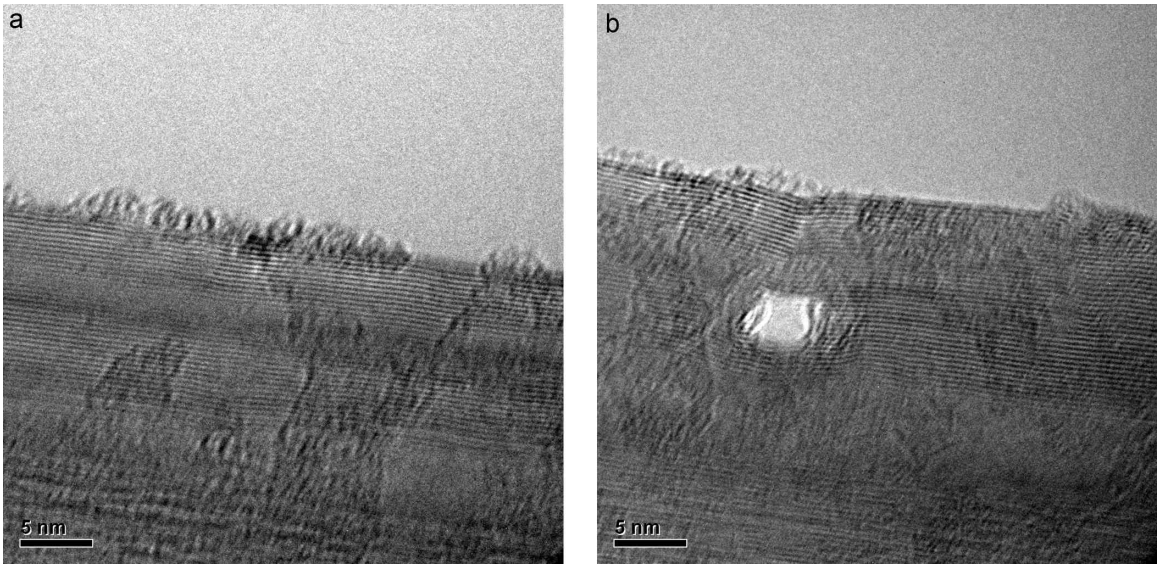

Figure 7.2: Electron beam modification of a freely suspended MWNT. a) Freely suspended arc discharge MWNT (scale of bar=5 nm). b) Freely suspended arc discharge MWNT with an e-beam drilled 2.5 nm diameter nanohole. The majority of the nanotube is unchanged (scale of bar=5 nm). Modification was in a hot stage at 500 °C.

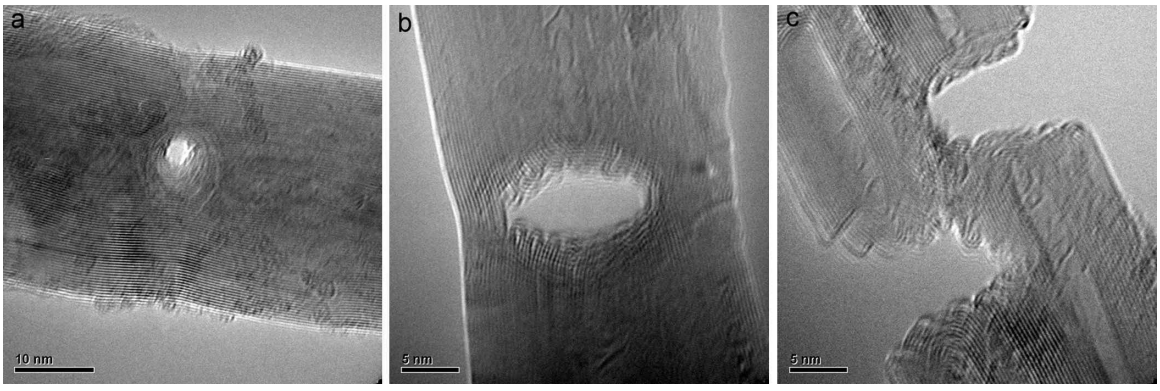

Figure 7.3: Various modifications of MWNTs with a focused electron beam. a) A small 2.5 nm diameter nanohole in a MWNT (scale of bar=10 nm), b) a large 11 nm across elliptical nanohole in a 26 nm diameter MWNT (scale of bar=5 nm), and c) a constriction in a MWNT fabricated by etching in from both sides (scale of bar=5 nm). Modification was in a hot stage at 500 °C.

metallic nanowires was done by molecular templating which has been previously described [20]. We fabricated several 100-200 nm by 10 μm long slits directly on a 500 nm thick silicon nitride membrane (SPI supplies) by FIB milling. Subsequently, fluorinated single walled carbon nanotubes (FSWNTs) were deposited on the slits by dipping the chips in a nanotube solution. FSWNTs (Carbon Nanotechnologies Inc.) used for molecular templating were suspended in isopropanol. The nanotubes were deposited on the samples by dipping the samples into the isopropanol/FSWNT suspension followed by a dip in clean isopropanol and then blown dry with a nitrogen gun. Metal was deposited on top of the nanotube by dc sputter deposition process to form a wire [20]. The TEM used was a JEOL 2010F, which uses a field emission gun operating at 200 kV. The TEM compatible sample with the nanotubes or nanowires was loaded into the TEM. For heating the sample, a Gatan hot stage was used. Standard alignment procedures were followed to obtain an image. Images were captured at low magnification with low beam intensity. A charge coupled device CCD camera captured the image using a Gatan Micrograph software. For etching, high magnification 800000-1.5×10^6 was used. The beam is focused to a caustic spot which is used for etching. Low intensity illumination around the caustic spot is used for visual feedback. However, at room temperature, the beam is intense enough to cause amorphization of the nanotube as is known to happen for high enough beam intensities [110]. Heating the MWNTs to 500 °C in a hot stage minimized this amorphization effect [112]. Overfocusing the microscope causes a distorted magnification effect, making it easier to get direct visual feedback of the etching process. Etching is confirmed by the observation of the appearance of black edged rings since overfocused objects have a black diffraction edge when underfocused they have a white diffraction edge [115]. In this case, the edges of the hole as they are being formed are what we are seeing. Small holes are formed by keeping the beam in one spot. Larger holes, slits, and constrictions are formed by sweeping the beam manually with the beam shift (see figure 7.3). Etching is viewed on the green phosphor screen intensity of caustic spot is too high to view in the CCD . Typically, spot size= 1 and $\alpha = 3$ were used but milling was also

observed with different spot sizes and αs. Finding optimum conditions for etching requires some on the fly adjustment of focus and beam intensity, but the etching effect itself is quite reproducible in all materials.

7.3 Discussion

We etched nanoholes in both carbon nanotubes and niobium nanowires. For metals [115] and nanotubes [116], beam heating should be negligible and the dominant modification effect should be knock-on displacement of the atoms by collision with the electrons . The maximum energy transferred when a relativistic electron strikes an atom follows the formula $T_{max} = 2E(E + 2m_e c^2)/Mc^2$, where T_{max} is the maximum energy transferred to the atom struck by the electron, E is the energy of the electron, m_e is the mass of the electron, c is the speed of light, and M is the mass of the atom struck [116]. Assuming 200 keV for the energy of the electrons since the 2010F has a 200 kV acceleration voltage, we can calculate the maximum transferred energy for C where $T_{max} = 43.7\,\text{eV}$ and for Nb where $T_{max} = 5.64\,\text{eV}$. The displacement energy of materials the energy needed to displace an atom is typically between 5 and 50 eV and depends on the type of chemical bond of the material. For C (MWNT) $E_d = 15\text{-}20\,\text{eV}$ [116] and for Nb $E_d = 24\,\text{eV}$ [115]. If the energy transferred exceeds the displacement energy, the material will be expelled. The energy needed to displace a carbon atom is exceeded so the carbon atoms are quickly expelled and a nanohole is cleanly etched through the carbon nanotube. For Nb, the energy imparted is not enough to expel the atom from a bulk sample. However, the energy required for sputtering knocking an atom from the edge of a surface is typically about 50 percent or less of the displacement energy [115]. Furthermore, other effects such as radiation induced diffusion or impurity enhanced displacement which this simple model does not take into account may also enhance the etching [116]. The less energetic expulsion of atoms from the niobium nanowire may be the source of the grains we observed near the nanoholes. The nanoholes etched in

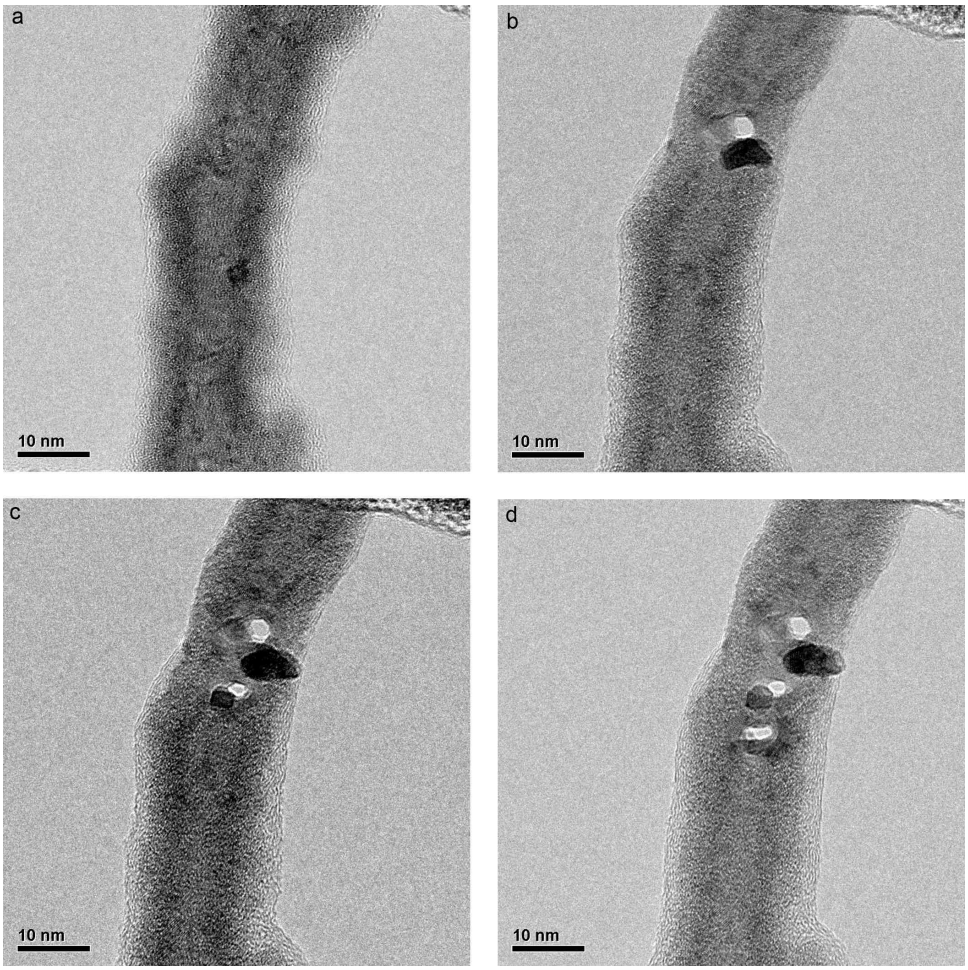

Figure 7.4: Drilling multiple holes in a niobium nanowire with a 200 keV electron beam. The width of the wire is about 20 nm. a) Initial unmodified niobium wire scale of bar=10 nm. b) Single nanohole drilled with a focused electron beam scale of bar=10 nm. c) Two nanoholes drilled with a focused electron beam scale of bar=10 nm . d) Three nanoholes drilled with focused electron beam scale of bar=10 nm. The sizes of the holes are 3, 2, and 2 nm, respectively. The distances between the holes are 6 and 9 nm. Grains of the material typically form near the holes drilled and are visible as darker spots. Modification was at room temperature.

niobium were still comparable in size to those obtained in carbon nanotubes (see figure 7.4). MWNTs and metallic nanowires have interesting and potentially useful transport properties. Local modification of a MWNT or nanowire might extend the usefulness of these properties. The constriction shown in figure 7.3 could be expected to impede electron flow and have significantly different transport properties from an unmodified nanotube. Two constrictions in series could possibly be used to make a single electron transistor, perhaps even one operating at room temperature. The nanoholes might be used as nanoscale magnetometers. On a side note, modification of the silicon nitride membrane near the MWNT is also possible. Such a sample design might be applicable to DNA/nanopore sequencing. It has been shown that a DNA molecule can be made to translocate through a nanopore lengthwise with each base pair going through the nanopore one by one [117–121]. It has been suggested that a nanopore articulated with nanotube electrodes might be able to detect differences between these base pairs and thus sequence DNA. By modifying the silicon nitride membrane near the nanotube, a nanopore articulated with a SWNT or a modified MWNT could be fabricated (see figure 7.6). The nanotube near the nanopore might even be modified to be a room temperature single electron transistor [50, 122, 123]

This approach might allow an unprecedented amount of information about the molecule translocating the nanopore to be detected [121, 124] In the above section we demonstrated that the electron beam can be used to etch extremely small nanoholes, as small as 2.5 nm in diameter. The next goal would be to achieve true EBESA, i.e., removal of single atoms. Here we argue that with existing technology this goal should be possible to realize. We choose graphene as our example. One requirement is that the layer on which EBESA is to be performed should be extremely thin, i.e., a monolayer or just a few atomic layers. Otherwise, scattering of electrons will not allow the beam to focus on a small enough area. TEM compatible graphene samples with a graphene monolayer suspended on TEM grids have been produced [97]. Graphene samples with a graphene monolayer suspended across a trench have also been produced [125]. EBESA requires a beam of electrons focused onto a

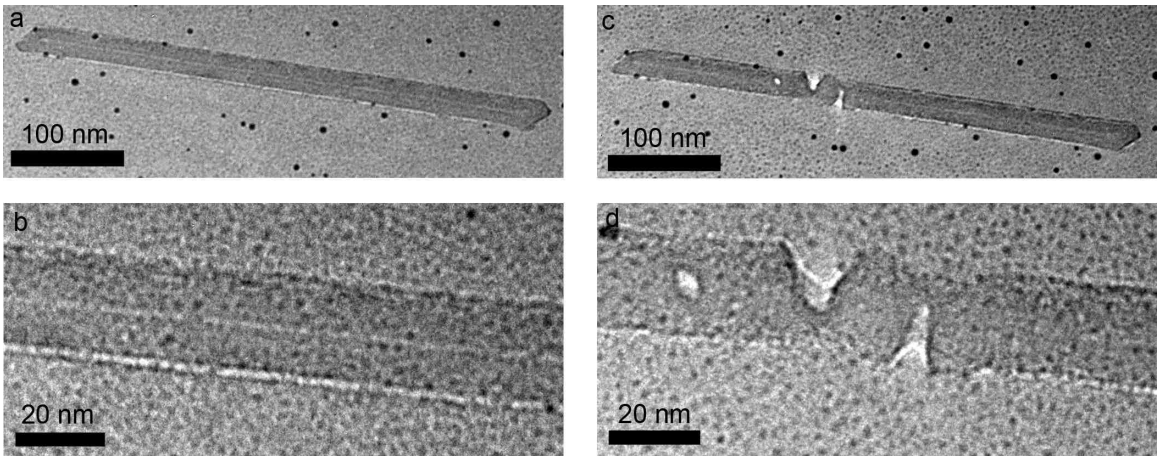

Figure 7.5: Electron beam modification of a MWNT on a silicon nitride membrane. a) TEM micrograph of an unmodified nanotube placed on the surface of a 50 nm low-stress silicon nitride membrane scale of bar=100 nm. The gray colored background corresponds to the amorphous SiN membrane. The image is underfocused creating white diffraction lines at the edges to contrast the nanotube against the amorphous layer. The black spots are from the deposition process. b) Close-up TEM micrograph of the unmodified tube in a scale of bar=20 nm. c) TEM micrograph of the nanotube after modification with the electron beam of the TEM scale of bar=100 nm. d) Close-up TEM micrograph of the modified nanotube with a nanohole on the left, 2.5 4 nm2 and two nanoconstrictions. In the nanoconstrictions, the silicon nitride can still be seen scale of bar=20 nm. Modification was at room temperature.

spot comparable or smaller than the distance between the atoms in an atomic layer. The beam of electrons in existing TEMs can be focused on such a small size. Spot sizes as small as 0.75 Åhave been demonstrated [126]. This is two times smaller than the smallest distance between atoms in graphene, which is 1.4 Å. Furthermore, it is known for single wall carbon nanotubes that the threshold energy, i.e., the energy the electrons require to knock out a carbon atom from the nanotube, is 80-140 keV [110]. The threshold energy for graphene can be expected to be similar. Modern TEMs such as the 2010F we used routinely operate at 200 kV so this energy requirement is easily satisfied. While it seems feasible to fabricate devices with atomic resolution using this method, there are still several technological difficulties to overcome. Keeping the modification localized to a single atom area and imaging a single atom dislocation in a TEM are the most obvious examples.

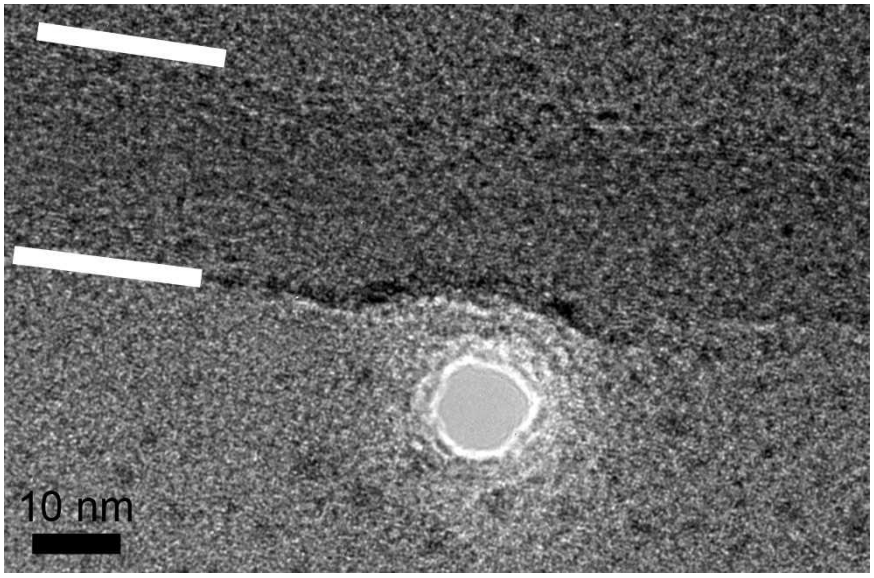

Figure 7.6: A TEM micrograph of a nanopore etched in a SiN membrane with a 200 keV focused electron beam scale of bar=10 nm. The white lines indicate the location of the MWNT. The hole is purposefully positioned near a MWNT. This sample design might be useful for experiments where molecules or nanoparticles are translocated through the pore and detected or characterized with the nanotubes. This sample design might be useful for DNA/nanopore sequencing.

7.4 Conclusion

In conclusion, we have demonstrated that a highly focused electron beam can be used to fabricate nanoholes and nanoconstrictions in MWNTs and niobium nanowires. We have discussed some potential applications of this fabrication method, such as articulating a nanopore with nanotube electrodes for DNA/nanopore sequencing experiments. We have also suggested that this fabrication method might in the future be extended down to the atomic scale, i.e., EBESA.

References

[1] H. Kamerlingh Onnes. *Leiden Comm.*, 120b, 122b, 124c, 1911.

[2] W. A. Little. *Phys. Rev.*, 156(398), 1967.

[3] M. Tinkham. *Introduction to Superconductivity*. Dover Publications, 1996.

[4] J. E. Lukens, R. J. Warburton, and W. W. Webb. Onset of quantized thermal fluctuations in "one-dimensional" superconductors. *Phys. Rev. Lett.*, 25(17):1180–1184, Oct 1970.

[5] R. S. Newbower, M. R. Beasley, and M. Tinkham. Fluctuation effects on the superconducting transition of tin whisker crystals. *Phys. Rev. B*, 5(3):864–868, Feb 1972.

[6] A. Rogachev, A. T. Bollinger, and A. Bezryadin. Influence of high magnetic fields on the superconducting transition of one-dimensional nb and moge nanowires. *Physical Review Letters*, 94:017004, 2005.

[7] A. J. Leggett. *Prog. Theor. Phys. (Suppl.)*, 69:80, 1980.

[8] A. T. Bollinger, A. Rogachev, M. Remeika, and A. Bezryadin. Effect of morphology on the superconductor-insulator transition in one-dimensional nanowires. *Phys. Rev. B (Rapid Comm.)*, 69:180503, 2004.

[9] A. Rogachev and A. Bezryadin. Superconducting properties of polycrystalline Nb nanowires templated by carbon nanotubes. *Applied Physics Letters*, 83:512, 2003.

[10] A. T. Bollinger, A. Rogachev, and A. Bezryadin. Dichotomy in short superconducting nanowires: Thermal phase slippage vs. Coulomb blockade. *Europhysics Letters*, 76:505, 2006.

[11] A. T. Bollinger, R. C. Dinsmore III, A. Rogachev, and A. Bezryadin. *Physical Review Letters*, 101:227003, 2008.

[12] Alexey Bezryadin. *Journal of Physics: Condensed Matter*, 20:043202, 2008.

[13] C. N. Lau, N. Markovic, M. Bockrath, A. Bezryadin, and M. Tinkham. *Phys. Rev. Lett.*, 87:217003, 2001.

[14] N. Giordano. Evidence for macroscopic quantum tunneling in one-dimensional superconductors. *Phys. Rev. Lett.*, 61(18):2137–2140, Oct 1988.

[15] N. Giordano. Superconductivity and dissipation in small-diameter pb-in wires. *Phys. Rev. B*, 43(1):160–174, Jan 1991.

[16] Maciek Zgirski, Karri-Pekka Riikonen, Vladimir Touboltsev, and Konstantin Arutyunov. *Nano Letters*, 5(6):1029, 2005.

[17] M. Zgirski, K.-P. Riikonen, V. Touboltsev, and K. Yu. Arutyunov. Quantum fluctuations in ultranarrow superconducting aluminum nanowires. *Phys. Rev. B*, 77(5):054508, Feb 2008.

[18] Fabio Altomare, A. M. Chang, Michael R. Melloch, Yuguang Hong, and Charles W. Tu. Evidence for macroscopic quantum tunneling of phase slips in long one-dimensional superconducting al wires. *Phys. Rev. Lett.*, 97(1):017001, Jul 2006.

[19] Dmitri S. Golubev and Andrei D. Zaikin. Quantum tunneling of the order parameter in superconducting nanowires. *Phys. Rev. B*, 64(1):014504, Jun 2001.

[20] A. Bezryadin, C. N. Lau, and M. Tinkham. Quantum suppression of superconductivity in ultrathin nanowires. *Nature*, 404:971, 2000.

[21] Robert Chesley Dinsmore. *Microwave Response in Superconducting Nanowires*. PhD thesis, University of Illinois at Urbana-Champaign, 2009.

[22] John M. Martinis, Michel H. Devoret, and John Clarke. Experimental tests for the quantum behavior of a macroscopic degree of freedom: The phase difference across a josephson junction. *Physical Review B*, 35:4682, 1987.

[23] M. Sahu, M.H. Bae, A. Rogachev, D. Pekker, T.C. Wei, N. Shah, P.M. Goldbart, and A. Bezryadin. Individual topological tunnelling events of a quantum field probed through their macroscopic consequences. *Nature Physics*, 5(7):503–508, 2009.

[24] A. Wallraff, A. Lukashenko, J. Lisenfeld, A. Kemp, MV Fistul, Y. Koval, and AV Ustinov. Quantum dynamics of a single vortex. *Nature*, 425(6954):155–158, 2003.

[25] J. E. Mooij and C. J. P. M. Harmans. *New Journal of Physics*, 7:219, 2005.

[26] J. E. Mooij and Y. V. Nazaron. *Nature Physics*, 2:169, 2006.

[27] J. Ku, V. Manachurian, and A. Bezryadin. Superconducting Nanowires as Nonlinear Inductive Elements for Qubits. *Arxiv preprint arXiv:1007.3951*, 2010.

[28] Thomas Aref, Matthew Brenner, and Alexey Bezryadin. Nanoslits in silicon chips. *Nanotechnology*, 20(4):045303, 2009.

[29] C. Scheibe and E. Obermeier. *J. Micromech. Microeng.*, 5:109, 1995.

[30] M. A. Meitl, Z-T. Zhu, V. Kumar, K. J. Lee, X. Feng, Y. Y. Huang, I. Adesida, R. G. Nuzzo, and J. A. Rogers. Transfer printing by kinetic control of adhesion to an elastomeric stamp. *Nature Materials*, 5:33, 2006.

[31] T. Aref, M. Remeika, and A. Bezryadin. High-resolution nanofabrication using a highly-focused electron beam. *Journal of Applied Physics*, 104:024312, 2008.

[32] M. Zhang, E. A. Olson, R. D. Twesten, J. G. Wen, L. H. Allen, I. M. Robertson, and I. Petrov. *Journal of Materials Research*, 20:1802, 2005.

[33] J. S. Langer and V. Ambegaokar. Intrinsic resistive transition in narrow superconducting channels. *Physical Review*, 164(2):498, 1967.

[34] D. E. McCumber and B. I. Halperin. Time scale of intrinsic resistive fluctuations in thin superconducting wires. *Phys. Rev. B*, 1(3):1054–1070, Feb 1970.

[35] Sang L. Chu, A. T. Bollinger, and A. Bezryadin. Phase slips in superconducting films with constrictions. *Physical Review B (Condensed Matter and Materials Physics)*, 70(21):214506, 2004.

[36] Dganit Meidan, Yuval Oreg, and Gil Refael. Sharp superconductor-insulator transition in short wires. *Phys. Rev. Lett.*, 98(18):187001, May 2007.

[37] K. K. Likharev. Superconducting weak links. *Reviews of Modern Physics*, 51(1):101, 1979.

[38] B. Muhlschlegel. Die thermodynamischen funktionen des supraleiters. *Z. Phys.*, 155:313, 1959.

[39] John Bardeen. Critical fields and currents in superconductors. *Reviews of Modern Physics*, 34(4):667, Oct 1962.

[40] M. Tinkham and C. N. Lau. Quantum limit to phase coherence in thin superconducting wires. *Applied Physics Letters*, 80:2946, 2002.

[41] M. Tinkham, J. U. Free, C. N. Lau, and N. Markovic. Hysteretic i-v curves of superconducting nanowires. *Physical Review B*, 68:134515, 2003.

[42] B. D. Josephson. Possible new effects in superconductive tunnelling. *Physics Letters*, 1(7):251 – 253, 1962.

[43] B. D. Josephson. Supercurrents through barriers. *Advances in Physics*, 14(56):419–451, 1965.

[44] D. E. McCumber. Effect of ac impedance on dc voltage-current characteristics of superconductor weak-link junctions. *Journal of Applied Physics*, 39(7):3113–3118, 1968.

[45] W. C. Stewart. Current-voltage characteristics of josephson junctions. *Applied Physics Letters*, 12(8):277–280, 1968.

[46] Anupam Garg. Escape-field distribution for escape from a metastable potential well subject to a steadily increasing bias field. *Phys. Rev. B*, 51(21):15592–15595, 1995.

[47] T. A. Fulton and L. N. Dunkleberger. Lifetime of the zero-voltage state in josephson tunnel junctions. *Phys. Rev. B*, 9(11):4760–4768, Jun 1974.

[48] Peter Hänggi, Peter Talkner, and Michal Borkovec. Reaction-rate theory: fifty years after kramers. *Rev. Mod. Phys.*, 62(2):251–341, Apr 1990.

[49] N. Shah, D. Pekker, and P. M. Goldbart. Inherent stochasticity of superconductor-resistor switching behavior in nanowires. *Physical Review Letters*, 101:207001, 2007.

[50] M. Remeika and A. Bezryadin. Sub-10 nanometre fabrication: molecular templating, electron-beam sculpting and crystallization of metallic nanowires. *Nanotechnology*, 16:1172–1176, 2005.

[51] A. K. Ghosh and D. H. Douglass. *Journal of Low Temperature Physics*, 27:487, 1977.

[52] H. Park, A.K.L. Lim, A.P. Alivisatos, J. Park, and P.L. McEuen. Fabrication of metallic electrodes with nanometer separation by electromigration. *Applied Physics Letters*, 75:301, 1999.

[53] Douglas R. Strachan, Danvers E. Johnston, Beth S. Guiton, Sujit S. Datta, Peter K. Davies, Dawn A. Bonnell, and A. T. Charlie Johnson. Real-time tem imaging of the formation of crystalline nanoscale gaps. *Physical Review Letters*, 100:056805, 2008.

[54] Hubert B. Heersche, G. Lientschnig, K. O Neill, H.S.J. van der Zant, and H.W. Zandbergen. In situ imaging of electromigration-induced nanogap formation by transmission electron microscopy. *Applied Physics Letters*, 91:072107, 2007.

[55] R. Holm. *Electrical Contacts*. Springer-Verlag, 1967.

[56] Alan W. Searcy, Robert J. Peavler, and H. J. Yearian. Preparation of mo3ge and determination of its structure. *Journal of the American Chemical Society*, 74:566, 1952.

[57] T. Aref and A. Bezryadin. Precise in-situ tuning of a superconducting nanowire's critical current using high bias voltage pulses. *Arxiv preprint arXiv:1006.5760*, 2010.

[58] A. O. Caldeira and A. J. Leggett. Influence of dissipation on quantum tunneling in macroscopic systems. *Phys. Rev. Lett.*, 46(4):211–214, Jan 1981.

[59] J. M. Kivioja, T. E. Nieminen, J. Claudon, O. Buisson, F. W. J. Hekking, and J. P. Pekola. Observation of transition from escape dynamics to underdamped phase diffusion in a josephson junction. *Phys. Rev. Lett.*, 94(24):247002, Jun 2005.

[60] V. M. Krasnov, T. Golod, T. Bauch, and P. Delsing. Anticorrelation between temperature and fluctuations of the switching current in moderately damped josephson junctions. *Phys. Rev. B*, 76(22):224517, Dec 2007.

[61] L. Huang, B. White, M. Y. Sfeir, M. Huang, H. X. Huang, S. Wind, J. Hone, and S. O'Brien. *J. Phys. Chem. B.*, 110:11103, 2006.

[62] K. Totsuka, H. Ito, T. Kawamura, and M. Ohtsu. *Jpn. J. Appl. Phys.*, 41:1566, 2002.

[63] K. Totsuka, H. Ito, K. Suzuki, K. Yamamoto, M. Ohtsu, and T. Yatsui. *Applied Physics Letters*, 82:1616, 2003.

[64] S-Y. Yim, E. Jeang, J-H. Lee, S-H. Park, and K. Cho. *Journal of the Korean Physical Society*, 45:1060, 2004.

[65] S. R. Park, H. Peng, and X. S. Ling. Fabrication of nanopores in silicon chips using feedback chemical etching. *Small*, 3:116, 2007.

[66] W. J. Venstra and P. M. Sarro. *Microelectronic Engineering*, 67:502, 2003.

[67] J. Brugger, J. W. Berenschot, S. Kuiper, W. Nijdam, B. Otter, and M. Elwenspoek. *Microelectronic Engineering*, 53:403, 2000.

[68] P. Zahl, M. Bammerlin, G. Meyer, and R. R. Schlittler. *Review of Scientific Instruments*, 76:023707, 2005.

[69] C. W. Park, O. V. Mena, and J. Brugger. *Nanotechnology*, 18:044002, 2007.

[70] S. Egger, A. Ilie, Y. Fu, J. Chongsathien, D-J. Kang, and M. E. Welland. *Nano Letters*, 5:15, 2005.

[71] M. M. Deshmukh, D. C. Ralph, M. Thomas, and J. Silcox. *Applied Physics Letters*, 75:1631, 1999.

[72] D. Hopkins, D. Pekker, P. Goldbart, and A. Bezryadin. Quantum interference device made by dna templating of superconducting nanowires. *Science*, 308:1762, 2005.

[73] J. A. Rogers, K. E. Paul, R. J. Jackman, and G. M. Whitesides. *Applied Physics Letters*, 70:2658, 1997.

[74] J. Maria, S. Jeon, and J. A. Rogers. *J. Photochemistry and Photobiology A: Chemistry*, 166:149, 2004.

[75] D. E. Prober, M. D. Feuer, and N. Giordano. *Applied Physics Letters*, 37:94, 1980.

[76] N. R. Tas, J. W. Berenschot, P. Mela, H. V. Jansen, M. Elwenspoek, and den. Berg. A. van. *Nano Letters*, 2:1031, 2002.

[77] M. Kociak, K. Suenaga, K. Hirahara, Y. Saito, T. Nakahira, and S. Iijima. *Physical Review Letters*, 89:155501, 2002.

[78] J. C. Meyer, D. Obergfell, S. Roth, S. Yang, and S. Yang. *Applied Physics. Letters*, 85:2911, 2004.

[79] J. Y. Huang, S. Chen, S. H. Jo, Z. Wang, D. X. Han, G. Chen, M. W. Dresselhaus, and Z. F. Ren. *Physical Review Letters*, 94:236802, 2005.

[80] T. Kim, J-M. Zuo, E. A. Olson, and I. Petrov. *Applied Physics Letters*, 87:173108, 2005.

[81] A. Yu, R. Deblock, M. Kociak, B. Reulet, H. Bouchiat, I. I. Khodos, Y. B. Gorbatov, V. T. Volkov, C. Journet, and M. Burghard. *Science*, 284:1508, 1999.

[82] S. B. Chikkannanavar, D. E. Luzzi, S. Paulson, and A. T. Johnson Jr. *Nano Letters*, 5:151, 2005.

[83] Y. Choi, J. Johnson, R. Moreau, E. Perozziello, and A. Ural. *Nanotechnology*, 17:4635, 2006.

[84] M. A. F. van den Boogaart, M. Lishchynska, L. M. Doeswijk, J. C. Greer, and J. Brugger. *Sensors and Actuators A*, 130:568, 2006.

[85] D. M. Eigler and E. K. Schweizer. Positioning single atoms with a scanning tunnelling microscope. *Nature*, 344(6266):524, 1990.

[86] M. F. Crommie, C. P. Lutz, and D. M. Eigler. Confinement of electrons to quantum corrals on a metal surface. *Science*, 262(5131):218, 1993.

[87] K. S. Novoselov, A. K. Geim, S. V. Morozov, D. Jiang, Y. Zhang, S. V. Dubonos, I. V. Grigorieva, and A. A. Firsov. Electric field effect in atomically thin carbon films. *Science*, 306:666, 2004.

[88] J. W. Mintmire, B. I. Dunlap, and C. T. White. Are fullerene tubules metallic? *Physical Review Letters*, 68(5):631–634, 1992.

[89] Kyoko Nakada, Mitsutaka Fujita, Gene Dresselhaus, and Mildred S. Dresselhaus. Edge state in graphene ribbons: Nanometer size effect and edge shape dependence. *Physical Review B*, 54(24):17954–17961, 1996.

[90] Q. Yan, B. Huang, J. Yu, F. Zheng, J. Zang, J. Wu, B. L. Gu, F. Liu, and W. Duan. Intrinsic current-voltage characteristics of graphene nanoribbon transistors and effect of edge doping. *Nano Letters*, 7(6):1469, 2007.

[91] D. S. Novikov. *Physical Review Letters*, 99:056802, 2007.

[92] Y. W. Son, M. L. Cohen, and S. G. Louie. Half-metallic graphene nanoribbons. *Nature*, 444:347, 2006.

[93] A. Rycerz, J. Tworzydlo, and C. W. J. Beenakker. *Nature Physics*, 3:172, 2007.

[94] B. Trauzettel, D. V. Bulaev, D. Loss, and G. Burkard. Spin qubits in graphene quantum dots. *Nature Physics*, 3(3):192, 2007.

[95] S. Y. Zhou, G. H. Gweon, A. V. Fedorov, P. N. First, W. A. de Heer, D. H. Lee, F. Guinea, A. H. Castro Neto, and A. Lanzara. Substrate-induced bandgap opening in epitaxial graphene. *Nature Materials*, 6(10):770, 2007.

[96] F. Peres, N. M. R. Guinea and A. H. Castro Neto. *Physical Review B*, 73:125411, 2006.

[97] J. C. Meyer, A. K. Geim, M. I. Katsnelson, K. S. Novoselov, T. J. Booth, and S. Roth. The structure of suspended graphene sheets. *Nature*, 446:60, 2007.

[98] M. S. M. Saifullah, K. Kurihara, and C. J. Humphreys. *J. Vac. Sci. Technol. B*, 18:2737, 2000.

[99] I. G. Salisbury, R. S. Timsit, S. D. Berger, and C. J. Humphreys. Nanometer scale electron beam lithography in inorganic materials. *Applied Physics Letters*, 45:1289, 1984.

[100] J. B. Heng, V. Dimitrov, Y. V. Grinkova, C. Ho, T. Kim, D. Muller, S. Sligar, T. Sorsch, R. Twesten, R. Timp, and G. Timp. The detection of DNA using a silicon nanopore. In *IEEE International Electron Devices Meeting, 2003. IEDM'03 Technical Digest*, page 767, 2003.

[101] A. J. Storm, J. H. Chen, X. S. Ling, H. W. Zandbergen, and C. Dekker. Fabrication of solid-state nanopores with single-nanometre precision. *Nature Materials*, 2(8):537, 2003.

[102] H. W. Zandbergen, R. van Duuren, P. F. A. Alkemade, G. Lientschnig, O. Vasquez, C. Dekker, and F. D. Tichelaar. Sculpting nanoelectrodes with a transmission electron beam for electrical and geometrical characterization of nanoparticles. *Nano Letters*, 5(3):549–554, 2005.

[103] S. Xu, M. Tian, J. Wang, J. Xu, J. M. Redwing, and M. H. W. Chan. Nanometer-scale modification and welding of silicon and metallic nanowires with a high-intensity electron beam. *Small*, 1(12):1221, 2005.

[104] M. D. Fischbein and M. Drndic. Sub-10 nm device fabrication in a transmission electron microscope. *Nano Letters*, 7(5):1329, 2007.

[105] J. Zhang, L. You, H. Ye, and D. Yu. Fabrication of ultrafine nanostructures with single-nanometre precision in a high-resolution transmission electron microscope. *Nanotechnology*, 18(15):155303, 2007.

[106] M. Terrones, F. Banhart, N. Grobert, J. C. Charlier, H. Terrones, and P. M. Ajayan. Molecular junctions by joining single-walled carbon nanotubes. *Physical Review Letters*, 89(7):75505, 2002.

[107] A. Hashimoto, K. Suenaga, A. Gloter, K. Urita, and S. Iijima. Direct evidence for atomic defects in graphene layers. *Nature*, 430:870, 2004.

[108] P. M. Ajayan, V. Ravikumar, and J. C. Charlier. Surface reconstructions and dimensional changes in single-walled carbon nanotubes. *Physical Review Letters*, 81(7):1437, 1998.

[109] V. H. Crespi, N. G. Chopra, M. L. Cohen, A. Zettl, and S. G. Louie. Anisotropic electron-beam damage and the collapse of carbon nanotubes. *Physical Review B*, 54(8):5927, 1996.

[110] B. W. Smith and D. E. Luzzi. Electron irradiation effects in single wall carbon nanotubes. *Journal of Applied Physics*, 90:3509, 2001.

[111] F. Banhart, J. Li, and M. Terrones. Cutting single-walled carbon nanotubes with an electron beam: evidence for atom migration inside nanotubes. *Small*, 1(10):953, 2005.

[112] J. Li and F. Banhart. The engineering of hot carbon nanotubes with a focused electron beam. *Nano Letters*, 4(6):1143, 2004.

[113] A. Zobelli, A. Gloter, C. P. Ewels, and C. Colliex. Shaping single walled nanotubes with an electron beam. *Physical Review B*, 77:045410, 2008.

[114] J. F. Celik-Aktas, J. Stubbins, and J.-M. Zuo. Electron beam machining of nanometer-sized tips from multiwalled boron nitride nanotubes. *Journal of Applied Physics*, 102(2):024310, 2007.

[115] D. Williams and C. Carter. *Transmission Electron Microscopy*. Plenum Press, New York, 1996.

[116] F. Banhart. Irradiation effects in carbon nanostructures. *Reports on Progress in Physics*, 62(8):1181, 1999.

[117] J.J. Kasianowicz, E. Brandin, D. Branton, and D.W. Deamer. Characterization of individual polynucleotide molecules using a membrane channel. *Proceedings of the National Academy of Sciences*, 93:13770–13773, 1996.

[118] A. J. Storm, C. Storm, J. Chen, H. Zandbergen, J.-F. Joanny, and C. Dekker. *Nano Letters*, 5:1193, 2005.

[119] H. Chang, F. Kosari, G. Andreadakis, M. A. Alam, G. Vasmatzis, and R. Bashir. Dna-mediated fluctuations in ionic current through silicon oxide nanopore channels. *Nano Letters*, 4(8):1551, 2004.

[120] J. B. Heng, C. Ho, T. Kim, R. Timp, A. Aksimentiev, Y. V. Grinkova, S. Sligar, K. Schulten, and G. Timp. Sizing DNA using a nanometer-diameter pore. *Biophysical journal*, 87(4):2905, 2004.

[121] J. Li, M. Gershow, D. Stein, E. Brandin, and J. A. Golovchenko. *Nature Materials*, 2:611, 2003.

[122] H. W. C. Postma, T. Teepen, Z. Yao, M. Grifoni, and C. Dekker. Carbon nanotube single-electron transistors at room temperature. *Science*, 293(5527):76–79, 2001.

[123] L. Guo, E. Leobandung, and S. Y. Chou. A silicon single-electron transistor memory operating at room temperature. *Science*, 275(5300):649, 1997.

[124] M. Zwolak and M. D. Ventra. *Nano Letters*, 5:421, 2005.

[125] J. S. Bunch, A. M. van der Zande, S. S. Verbridge, I. W. Frank, D. M. Tanenbaum, J. M. Parpia, H. G. Craighead, and P. L. McEuen. Electromechanical resonators from graphene sheets. *Science*, 315(5811):490, 2007.

[126] P. E. Batson, N. Dellby, and O. L. Krivanek. Sub-angstrom resolution using aberration corrected electron optics. *Nature*, 418:617, 2002.

Vita

Thomas Aref was born May 30, 1980 in Ithaca, New York (his parents were graduate students at Cornell at the time). He graduated from University of Illinois at Urbana-Champaign with a B.S. in Engineering Physics in 2002. He decided to pursue his graduate studies there as well and joined Professor Alexey Bezryadin's group in 2003. He also earned his masters degree in Physics in 2003. He started off on a project focused on detecting biomolecules such as DNA and protein. He gradually adapted the methods for making nanopores into modifying nanotubes and nanowires with the focused electron beam of a transmission electron microscope which led to his first paper published in Journal of Applied Physics. While attempting to devise a more robust platform for performing TEM imaging combined with electrical transport measurements, he developed a unique form of nanoslit. The fabrication method and applications of these nanoslits were published in nanotechnology. More recently, Thomas has focused on modifying nanowires in-situ with high bias voltage pulses. He explained a unique phenomenon that occurs when MoGe nanowires are exposed to high bias voltage pulses and was able to use the effect to precisely set the switching current of the nanowire. He used this pulsing method to extend work on probing quantum phase slips in superconducting nanowire. After completing his Ph.D., Thomas will be starting a post-doc in Professor Jukka Pekola's lab in Finland where he will be continuing his work on nanoelectronics with a focus on quantum metrology.